Quantitative Intravoxel Analysis of microCT-Scanned Resorbing Ceramic Biomaterials

Agnes Czenek

Thesis of 60 ECTS credits
Master of Science in Biomedical Engineering

June 2014

Quantitative Intravoxel Analysis of microCT-Scanned Resorbing Ceramic Biomaterials

Agnes Czenek

Thesis of 60 ECTS credits submitted to the School of Science and Engineering at Reykjavik University in partial fulfillment of the requirements for the degree of
Master of Science in Biomedical Engineering

June 2014

Supervisors:

Dr. Paolo Gargiulo
Assistant Professor, Reykjavik University
Dr. Ólafur E. Sigurjónsson
Associate Professor, Reykjavik University
Dr. Gissur Örlygsson
Project manager, Innovation Center Iceland
Dr. Christian Hellmich
Professor, Vienna University of Technology

Examiner:
Dr. Kristján Leósson
Senior Research Scientist, Science Institute, University of Iceland

Megindleg greining á innihaldi rúmmálseininga smásneiðmynda af niðurbrjótanlegum keramískum lífaðhæfdum efnum

Agnes Czenek

60 ECTS eininga ritgerð til
Meistaraprófs (MSc) i heilbrigðisverkfræði

Júní 2014

Megindleg greining á innihaldi rúmmálseininga smásneiðmynda af niðurbrjótanlegum keramískum lífaðhæfdum efnum

Agnes Czenek

60 eininga ritgerð lögð fram við tækni- og verkfræðideild
Háskólans í Reykjavík til
Meistaraprófs (MSc) í heilbrigðisverkfræði

Júní 2014

Leiðbeinendur:

Dr. Paolo Gargiulo
Lektor, Háskólinn í Reykjavík
Dr. Ólafur E. Sigurjónsson
Dósent, Háskólinn í Reykjavík
Dr. Gissur Örlygsson
Verkefnisstjóri, Nýsköpunarmiðstöð Íslands
Dr. Christian Hellmich
Prófessor, Vienna University of Technology

Prófdómari:
Dr. Kristján Leósson
Vísindamaður, Eðlisfræðistofa Raunvísindastofnun Háskóli Íslands

Quantitative Intravoxel Analysis of microCT-scanned Resorbing Ceramic Biomaterials

Agnes Czenek

Thesis of 60 ECTS credits submitted to the School of Science and Engineering at Reykjavik University in partial fulfilment of the requirements for the degree of

Master of Science in Biomedical Engineering

June 2014

Student:

Agnes Czenek

Supervisors:

Paolo Gargiulo

Ólafur E. Sigurjónsson

Gissur Örlygsson

Christian Hellmich

Examiner:

Kristján Leósson

Contents

Abstract

The synergy between 3D scaffold and cell differentiation is crucial for new bone tissue formation in tissue engineering. The structure and bioactivity and compatibility of the scaffolds material play a critical role of stimulating the cell functionality. Researches on this field aim to bring a robust knowledge of 3D scaffold fabrication and cell culture *in vitro/vivo*. The aim of this thesis was to develop a novel method of 3D imaging technique for new bone tissue analysis on a 3D resorbing ceramic scaffold, cultured *in vitro*. The 3D imaging technique is based on microCT assessment combined with 3D modeling procedure. This standard microCT assessment has been used in researches in different kind of analyses, however this perspective is based on one kind of statistical evaluation of grey values illustrating the microCT images. The grey values are in linear relation to the X-ray attenuation coefficient of the material being scanned. Thus the relation between grey values and attenuation coefficients depending on the X-ray energy is identified by proportionality constants. In this thesis a novel method is presented which retrieves the proportionality constants and the used X-ray energy for the CT image acquisition. This method will be wield to identify the elastic properties of the tissue engineered configuration of the 3D ceramic scaffold along with extracellular bone matrix. Ten 3D tricalcium phosphate (TCP) scaffolds were microCT scanned, then cultured with pre-osteoblastic cells for 3, 6, and 8 weeks. The scaffolds were re-scanned subsequently after cultivation. The outcome of this analysation showed that the corresponding voxel-specific nanoporosities turn out to increase during the culturing period following in reduced elastic properties, as determined from micromechanical considerations, while the overall macroporosity remains constant.

Keywords–
Tissue engineering scaffold, continuum micromechanics, Computed Tomography, X-ray physics, tri-calcium phosphate

Ágrip

Samræmi milli þrívíðar stoðgrindur og ræktun frumna er mjög mikilvægt til beinmyndunar í vefjaverkfræði. Lögun og eiginleikar efnisins í stoðgrindinni getur haft áhrif á hegðun frumna og vöxt þeirra. Rannsóknir á þessu sviði einblína á að öðlast djúpa þekkingu varðandi samspil milli þrívíðar stoðgrindur úr mismunandi efnum og frumu tegundir í frumuræktunum *in vivo/vitro*. Markmið þessa verkefnis var að þróa stafræna úrvinnslu er byggir á smásneiðmyndun af þrívíðum bíókeramiskum stoðgrindum sáð með stofnfrumum sem leyfir þrívíddar endurbyggingu, módelgerð, mælingar, og tölfræðilegar útreikningar sem stutt geta greiningu á frumuvexti eftir ákveðinn tíma í frumu ræktun.
Skannaðar voru sex þrívíð þríkalsíum fósfat stoðgrindur með smásneiðmyndunar tæki í Nýsköpunarmiðstöð Íslands. Eftir skönnun voru þau ræktuð með frumum í 3, 6, og 8 vikur og aftur skönnuð eftir ræktun. Rúmmálsbreytingar verða greindar með þrívíðum líkanagerðum af byggingu stoðgrindanna og verða studdar með myndum fengnar úr rafeindasmásjá. Smásneiðmyndirnar voru einnig greindar með tölfræðilegum útreikningum sem byggir á línuleg tengsl milli dreifni stuðul skannaða efnisins og gráskálagildisins sem fæst úr sneiðmyndunar tækinu. Þessi aðferð er studd með X-ray eðlisfræði þekkingu með notkun á þekkt gildi á ljóseindar orku í smásneiðmyndunar tækinu. Samanburður á gráskalagildum er gerður á milli stoðgrinda fyrir og eftir ræktun á mismunandi tímabilum. Niðurstöður sýndu að rúmmálsbreytingar á míkró skala voru lítillegar milli ræktunar tímabila en aftur á móti urðu marktækar breytingar á nanó skala í bíókeramiska efninu. Með ör-aflfræði útreikningum var sýnt fram á að porurnar á nanó skala hafa aukist í efninu með tilliti til tíma sem leiddi til minnkun á eðliseiginleika efnisins. Aðferðir sem byggja á sneiðmyndunar tækni er ákjósanlegar í ljósi þess að þurfa ekki að fórna sýnunum til rannsóknar og því eru frekari rannsóknir á sama sýni mögulegar.

-Lykilorð

Vefjaverkfræðilegar stoðgrindur, öraflfræði, smásneiðmyndun, X-ray eðlisfræði, trí kalsíum fósfat

1 Introduction

1.1 Tissue Engineering

In general the main goal of tissue engineering (TE) is to generate new tissue for implantation to replace a greatly damaged organ in the human body. The major reason for this kind of a damaged tissue might be due to serious diseases or injuries that the human body is not able to recover by itself. With this method, investigators on this field are trying to circumvent difficulties in surgery such as organ transplantation from a donor, cadaver or different species. These difficulties are mostly immune reaction due to resistance to the new implanted organ. These kind of transplantations are also highly limited in sake of a lack in identical donor. Numerous implantations using non-biological materials with lack of biocompatibility might lead to infections including toxicity and allergic responses shortly after the surgery. These synthetic products can effect the surrounding tissue in a negative manner. Moreover they have limited material durability and do not grow with time, in case of an implantation to children. There are endless variations of objects that might inhibit implantations so list of obstacle might continue further on. For the procedure of engineer a vital organ with abilities of function, three major fields are fused together. These are cell cultivation procedure of different kind of stem-cells, three dimensional (3D) biomaterial scaffold design, and control of bioactive molecules during cell differentiation, and cultivation. The combination of these three objects are vital in order to guide cellular behaviour for new tissue formation and also to analyse the behaviour of biomaterials of 3D scaffolds during cell cultivation *in vitro/vivo*, see Figure 1. The most comprehensive

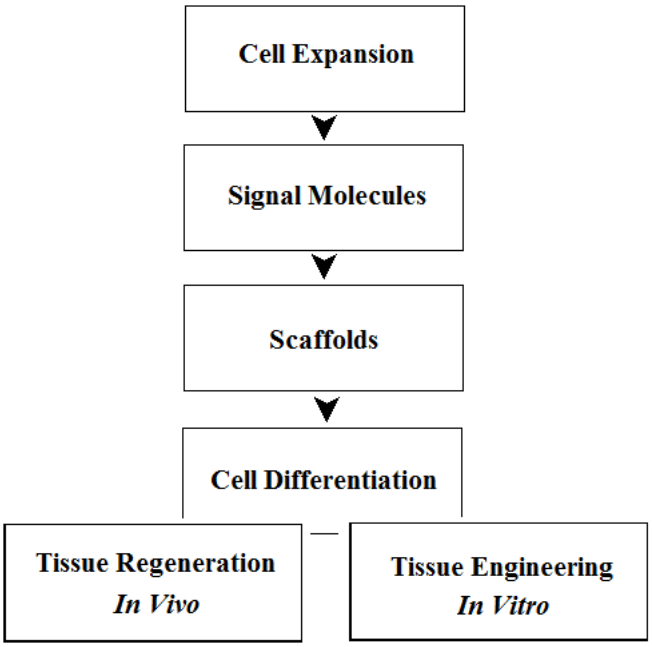

Figure 1: Tissue Engineering is based on several approaches including cell expansion, usage of 3D scaffolds, using growth factors and Cell differentiation in culture

procedure is to generate an object out of biodegradable material which is formed similar as the desired new tissue and combine it with a suitable expanded cell type to be further cultivated. During the cultivation the cells are differentiated and new tissue is formed on the biodegradable scaffold by time and implanted into the patient in need. The degradable, biomaterial dissolves by time leaving the new tissue behind for proper function. In tissue engineering a complex synergy is studied and applied between varying cells and different 3D scaffold materials for enhanced improvements in researches of new tissue formation.[1] Nevertheless the most complex challenge is to create a convenient environment for cells during cultivation. It has been

concluded that stem cells need a special environment in order to be able to differentiate into a desired type of cell. The environment is varying regarding to the desired cell type, which builds up the wanted organ. The human body needs to be mimicked *in vitro* for cell differentiation and extracellular matrix (ECM) formation. Furthermore the mechanical stimulation can inspire cell growth and induce ECM formation and in a more homogeneous manner. For these chemical and mechanical stimulations a complex controlled system is needed and it is performed with bioreactor systems, described in more detail later.[2] Researches on the field of TE are expanding and numerous techniques are developed with the goal of designing a functional tissue for implantation. However only few complex subjects have entered clinical trials, i.e. replacement of joint defects. The most challenging task is to create a cultivation system *in vitro* with an effective transmission of nutritions and oxygen supply, temperature regulation, moreover an ability for waste removal.[3] Particularly Azami et al. has concluded good cellular migration and osteoconductivity on the scaffolds macroporosities with cytoplasmic extension within four days of cell culture. The scaffolds architecture including mechanical properties similar to spongy bone is indeed suitable for cell penetration and new tissue formation. The cell migration and ECM production on the 3D scaffold along with surface and cavities were captured with SEM with low and high magnification. The cultivation is carried out *in vitro* and the time span of the

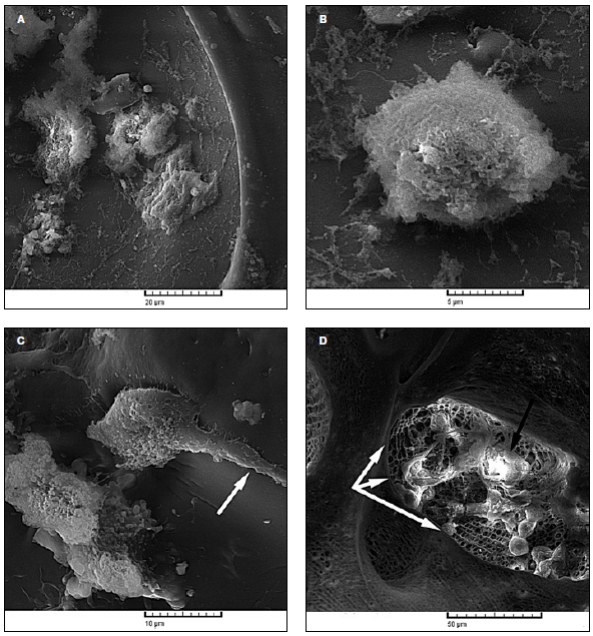

Figure 2: Scanning electron microscope images of SaOS-2 cell type seeded on nanocomposite scaffold, resulting cell attachment and migration over the surface of the scaffold.

cell differentiation is partially four days which is quite short in this field of researches. Although they alone analyse the cell proliferation/extension and migration but do not discuss the scaffolds biodegradability during the cultivation period including macro- and nanoporosity. Nevertheless their results strongly indicates the 3D porous scaffolds positive ability for cell attachment furthermore new tissue formation and the ability of cell proliferation and migration. This research presents cultivation of advanced human osteoblst-like cells and the scaffolds material is made out of hydroxyapatite/gelatine which might be more osteogenic than other scaffold materials, inducing earlier osteogenic differentiation which supports further more cell proliferation within shorter time period. Primary human cell sources are frequently used since they have clinical applicability and have no differences in interspecies. [4, 5, 6] However human derived cell types represent heterogeneous cell population and have limited accessibility of human osteoblast cells. For this reason bone cells derived from animals are used in researches. Moreover they are frequently used regarding their advantages, i.e. existence of unlimited number of cells, homogeneous character, and phenotypic differentiation from pre-osteoblasts

to osteablastic cells. MC3T3-E1 characterizes a pre-osteoblastic mouse calvariae cell line which has five sub-clones, 4, 8, 11, 14, and 26, however only two of them, 4 and 14 are capable for extracellular matrix production. The latter have been shown to undergo proliferation and mineralisation during researches. The *in vitro* experimental design is very complex, the cell cultivation environment is needed to be mimicked as in a living tissue. Several factors influence the ability of cells for differentiation and proliferation which can lead to varying outcomes. Here might mention the variety of medium types, cell seeding technique, different stimulations used during differentiation and the whole culture procedure itself. Under satisfactory conditions during incubation period the cell line starts a physiological response including migration and it undergoes a passage of differentiation into mature osteoblasts whith proliferation, matrix maturation, and matrix mineralization. This is the intention of most cell-based experimentations in order to study and analyse the behaviour and connectivity of cell and scaffolds material. [7, 8, 9, 10, 11] This complex cell functionality during cell-based experimentations results with time new tissue in 3D network on the surface of the scaffold and moreover throughout its center in case of satisfactory environment. As earlier was described, there are several limitations regarding 3D scaffolds, such as incomplete pore interconnection, degradation characteristics plus in case of a static culture there is poor mass transport through the scaffolds core due to no flow in culturing media. Thus in static culture the cells in the growing state show fibroblastic morphology during differentiation resulting mono layer of viable cells surrounding the scaffolds body. This cell-layer hinders the mass transfer even more into the core of the scaffold and cells are entrapped below it causing necrotic central region. [10] In order to prevent this phenomenon a constant or periodical effective flow is needed of the culturing media surround the scaffold or for a greater effect an application of perfusion throughout the porous 3D scaffold. Like in living tissue the environment of cells are not mechanically passive so in order to get the most out of cell differentiation and mineralisation the environment is needed to be engineered, mimicking a living tissue environment. Compact cultivation systems has been engineered for this specific purpose resulting many varying types of systems called bioreactors. These bioreactor systems for cell cultivation are specially designed to achieve this goal with important factors that enhance cell migration and mineralisation, resulting new 3D network tissue formation. [12] The most known types of cell cultivation systems in the field of tissue engineering are including spinner flask, rotating wall, perfusion, and compression bioreactors. The latter differs from the other systems, thus mechanical effect is applied on the scaffolds with compression in spite the others aiming on having an effect on the cell culture medium. For the compression bioreactor the scaffold's material is needed to be elastic and non-breakable to achieve durability throughout the entire experiment. The bioreactors aiming on the movement of the culture medium have different strategies which have advantages and also disadvantages.[13, 14] With this techniques the cell function increases resulting a homogeneous distribution of cell migration on the scaffold's nearly entire 3D body and indeed the ECM production is generated likewise.[15, 16] Nevertheless the major key for an effective new tissue formation is a collaboration of three important entities, which are the cells-osteogenic ability, ECM function, and an ideal 3D scaffold with suitable architecture, made out of a biomaterial which enhances cell functionality. For bone tissue engineering, pre-osteoblastic cells need a specifically suitable, stimulative environment for creation of biological construct of cells resulting ECM matrix for new bone formation. The length scale of the complex cell and tissue hierarchy is around few up to hundreds of nanometers. The ECM of bone cells includes poorly carbonated apatitic mineral similar to bone tissue which is produced by mature osteoblasts which are differentiated from pre-osteoblastic cells after migration into the cultivation surface.[17] As a result the new tissue, more specifically the cell environment is rather complex having a 3D shaped ECM organisation. The ECM function is rather important for cells, it ensures structural and physical support in the cell environment allowing migration and signal transportation between cells. This means that this complex matrix gives them ability for regulation of their activities. It may act as a source for growth factor and helps their bioactivities. The interpretation of the mineralization in ECM is essential for understanding the initiation and morphology of new bone tissue produced by viable cells. However this goal is still slight far away thus researchers have varying results and implementation of ECM function, mineralization, and likewise the effect on the scaffolds biomaterial. Since the whole tissue engineering process starts with cell attachment to a 3D scaffold for differentiation in order to reach a proper functionality for ECM production, the most efficient biological 3D scaffold would be a copy of the ECM of the target tissue. However the ECM is a very

complex phenomena with multiple functions and complicated composition which is very difficult to resemble. The ECM functional characteristics are on a very small length scale, below hundreds of nanometer, which makes its analysation rather challenging for researchers. Additionally the interaction between the scaffold's biomaterial and the ECM in early stage is not clear. Moreover apatite derived from synthetic samples differ from bioapatites in chemical and physical properties. Thus initial deposition of hydroxyapatite (HA) is unknown within the ECM which is a mixture of minerals similar to bone matrix and organic tissue.[18] For now researchers had aimed to mimic the ECM partially with characteristics as supportive architecture for cells, cyto- and tissue compatibility, and last but not least bioactivity and degradability in order to let new tissue replace the scaffold by time.

1.2 Biological Scaffold

As earlier was clarified the synergy between cells and 3D scaffold structures are needed to be achieved in beneficial therapeutic strategies, resulting in promotion of structural and functional living tissue. Researches in field of TE require apparatus which alter on many characteristics with great respect to the tissue type being requested for invention. One of the key characteristics is the material and morphology of the 3D scaffold. The cells function and grow in a sufficient environment, that can be achieved *in vitro* by mimicking the ECM of the chosen cell type. For that reason most of the 3D scaffolds are contrived with aim to have similar characteristics as the ECM of the desired cell type. In resent researches many aspects are considered for a proper design of a 3D scaffold for tissue engineering. The first vital thing that might mention is the materials biocompatibility. The host tissue might start a reaction due to the foreign implanted material causing symptoms that might lead to serious disorders or even causing death of patients. Furthermore it is important that the chosen cells for tissue formation can attach to the scaffolds material, migrate and be capable to function properly. A proper material for TE is also bioactive which means that it promotes cell interactions and has an ability to provide growth factors and other bioactive entities for cell function and differentiation. During investigation of biomaterials the regulation of cellular function is studied carefully in order to understand the interrelation between cell lines, ECM function, and varying type of biomaterials.[18, 19] For a purpose of tissue formation biomaterials need to induce bone-related gene expression, nonetheless effect of factors as biomaterials are still unknown regarding to intracellular growth and biosynthesis at molecular level. [19] Moreover it is important that the material is bioinert, thus it does not initiate a response after implantation. The scaffolds morphology and topology needs to be suitable for the researches performed *in vitro/vivo*. There have been countless developments of materials and architectures of scaffolds which improve cell migration and differentiation. Thus 3D biological scaffolds structures provide a skeleton for cells for migration and differentiation. It is a guideline for them to build up a new initial tissue for implantation. Accordingly it is an advantage if the material is biodegradable, with this ability the material dissolves in the body slowly by time allowing a replacement of the new tissue. While the scaffolds material dissolves slowly, it provides a shelter and temporary mechanical support against forces initiating in the human body. Additionally the scaffold offer free space for new tissue formation with its unique architecture.[20] Regarding 3D porous-scaffold fabrication the critical characteristics are the size, percentage of porosity, anisotropy, material properties and mechanical properties. For new bone tissue formation the 3D scaffold maintains similar mechanical properties as trabecular bone, the macroporosity is approximately 50-90 % within a characteristic range of 100-500 μm. The internal architecture needs to be suitable thus the size of the macroporosity is important for cell differentiation in order to be able to migrate and proliferate inside the pores.[21] If the proportionality of internal macroporosity is low-grade, it results poor flow through the scaffold causing insufficient nutrition and gas transfer to cells, causing cell-death within the scaffold by time.[22] Not only the scaffolds architecture is important, the right choice of the biomaterial is with respect to the host tissue and also with privilege to the cells attachment, penetration for new tissue formation and the ability to create a suitable structure of the 3D scaffold for the replacement of the damaged tissue. Numerous materials have been investigated, with respect to a predominant material, polymer. Different kind of polymers have been used in this field. Besides polymers, calcium phosphate (CaP) materials have been used in researches more specifically for bone tissue engineering. In view of the fact that it is biocompatible, bioactive, biodegradable, and moreover it is present in human body. The most common CaP ceramics is

hydroxyapatite (HA). For more specific manufacture of 3D structures synthetic CaP ceramics have been used. By means of different fabrication methods, varying types of CaP ceramic scaffolds have been involved in researches during *in vitro/vivo* experimentations, see Figure 3.

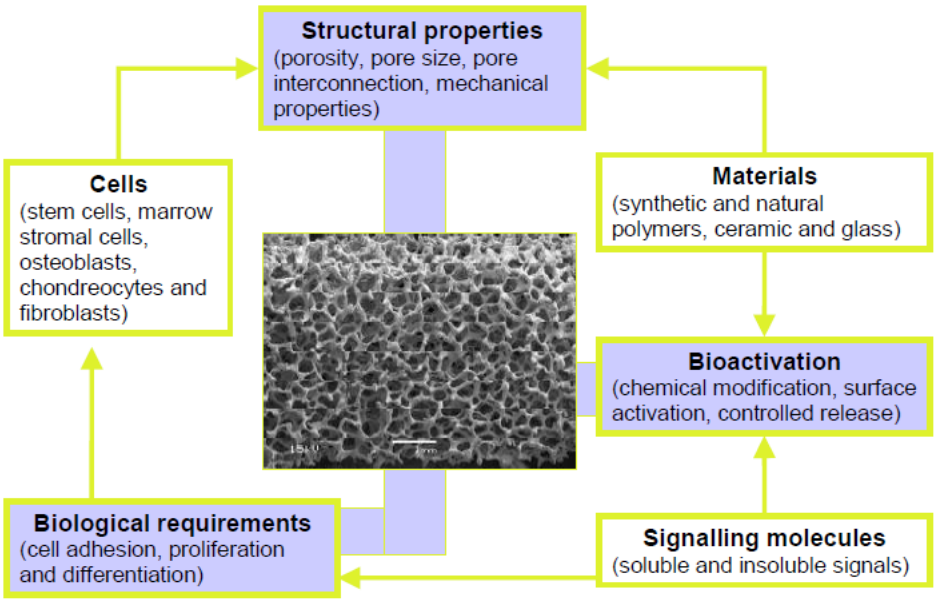

Figure 3: Properties of 3D biological scaffolds for tissue engineering

However despite all the positive results on this territory with biodegradable ceramic scaffolds, the behaviour of the nanoporosity has not been studied sufficiently during the time span of cell culture. What if the behaviour of intrinsic scaffold materials shows some changes during the culturation period? Could it be that it affects the surrounding tissue and the extracellular matrix production?[23]

1.3 MicroCT evaluation for Tissue Engineering

Since 3D ECM networks are produced in new bone tissue on a scaffold's body with a complex structure, a 3D imaging technique is exemplary for analysis. Researches in tissue engineering use microCT evaluation of the tissue engineered configuration with an aim of visualizing the increase of cultured extracellular matrix production in a non-destructive manner. With the microCT technique is possible to visualize the scaffolds entire structure including pore size, proportionality of porosity, and interconnected surfaces in its core.[5, 24] In this case the microCT images are implemented with selected voltage, current, sampling distance in order to get a suitable spatial resolution with computed back projection. The equipment uses an X-ray beam, which goes through a slowly rotating object of interest inside the scanner. The attenuation intensity of the X-ray is detected by a detector. The intensity is obtained and recoded by a computer. The 2D shadow images were converted to digital images, 2D image slices through the object with back projection, see Figure 4. These 2D slices consists out of voxels represented by grey value. One voxel is illustrated with one specific grey value. The data sets from the CT scanner were 8 bits in depth, following a grey scale existing out of 256 grey values. The attenuation coefficient is in linear relation ship with the grey values.[25, 26, 27, 28] Present studies use mostly microCT examinations in terms of investigation of porosities in macro- and microscale with characteristic length from few mm to several μm. With the aim of new tissue engineering 3D imaging evaluation technique is often used in order to map the ECM network formation and calcification.[29] Also

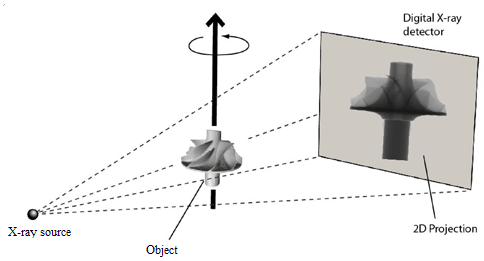

Figure 4: Function of Computed Tomography

with this technique, investigation on varying types of 3D structural scaffolds have been carried out for overall behaviour of the scaffolds material *in vitro/vivo*, such as ability of bioactivity and degradability.[6] Likewise it is very sufficient for morphology and topology evaluation of various 3D scaffolds, since SEM only guarantees 2D image observation in a specific diameter and the samples must be sacrificed during preparation for the SEM investigation. Although histological processes might be time-consuming and deliver 2D sections which can be misinterpreted during analysis of the 3D tissue within the cavities of a complex 3D scaffold. This process is not suitable for quantification of a network tissue surrounded by a biomaterial further more a professional, statistical comparison within experimental groups is not guaranteed[15]. Various software applications are combined with microCT imaging techniques in order to obtain 3D quantitative parameters with reconstruction of 2D images. These images are presented in grey level with respect to the X-ray attenuation of the samples material being scanned. The 3D image evaluation appear to be more reliable concerning changes in the 3D structure than the 2D analysis with other techniques[24, 30]. Komlev et al. concludes a 3D visualization method where the data is rendered directly without decomposing it into geometric primitives. A software, VGStudio MAX is used for 3D image generation and further analysation of the porous scaffold seeded with cells. With this procedure they are able to measure the macroporosity and cell proliferation by thresholding with respect to the grey level gathered from the microCT device. Privilege of use of microCT quantification is a sufficient resolution for detection of complex 3D samples with various material in a non-destructive manner. Moreover microCT scanners with a software application delivers morphometric analysis of 3D images build up of voxel specific attenuation in terms of grey level. With these voxel specific grey levels is possible to evaluate the voxel specific elastic properties of the 3D structure for further investigation in biomechanics. It is also favourable to mention the fact of cost reduction during sample analysation in researches[15].

2 Thesis Work

In this cell-based research on the field of tissue engineering several multidisciplinary fields were combined in order to carry out the experiment including cell cultivation and differentiation, microCT imaging, SEM observation, 3D modeling, and statistical analysis of the microCT images carried out with MATLAB computations. The thesis work flow is illustrated in details in Figure 5.

2.1 MicroCT Acquisition

The starting point was determined with microCT acquisition of ten 3D scaffolds (Becton, Dickinson and Company, La Jolla, CA, USA), as produced in a plastic flacon carried out with phoenix nanotom s, General Electric Measurement and Control (Department of Materials, Biotechnology, and Energy, Innovation Center, Reykjavik, Iceland). The microCT scanning procedure was carried out with 160 μm, 90 kV, with a copper filter, and a sampling distance with 7,33 microns.

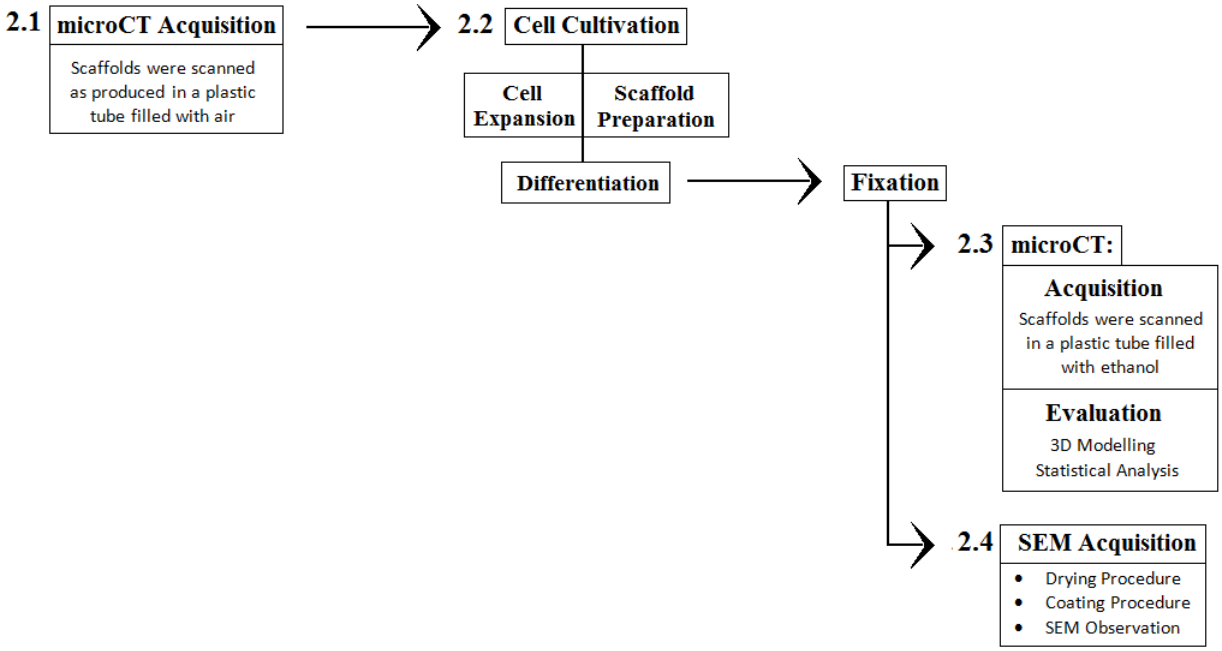

Figure 5: Thesis workflow

2.2 Cell Cultivation

Subsequently the 3D scaffolds were prepared for cell seeding and cultivation at REModeL Laboratory, The Blood Bank, Landspitali University Hospital, Iceland. The chosen cell line was MC3T3-E1, sub-clone 4 of mouse pre-osteoblasts, for the *in vitro* cultivation. This cell line whas chosen with an intention of high level of differentiation and its ability to form a well mineralised ECM [16]. The cells prior for scaffold seeding were expanded for seven days. Following the expansion cells were ready for the attachment on the prepared 3D β-TCP scaffolds. Seven out of ten scaffolds were seeded with cells the other three left empty for control. These ten scaffolds were divided into three groups, each group was cultured separately for 3, 6, and 8 weeks. Three scaffolds (two with cells and one empty) were cultured for 3 and 6 weeks, four scaffolds (three with cells and one empty) were cultured for 8 weeks. The reason for one extra scaffold is the risk of infection during differentiation which increases by time.

2.3 MicroCT Acquisition and Evaluation

Following the cultivation period, the scaffolds were fixed and re-scanned with the microCT. At the end of evaluation, informations were gathered and a decision was made that six samples out of ten will be examined in this experiment. Two scaffolds from each group with different cultivation period. The reason for this decision is that, during the experiment some cells spread out to the control samples in every group. Also the additional sample in the last group cultured for 8 weeks was not needed, since no infection occurred. Moreover the controls are not comparable to the other once since the scaffold's material is not completely identical. Thus the behaviour of the scaffold's material is only compared in two time sequences, i.e. before and after cultivation. The data sets gathered from microCT were saved as 8 bit "TIFF" files which were analysed with statistical evaluation of the grey values. On the CT image slices the grey values are representing the material of the object being scanned. The most frequent grey value representing each material on the CT image is used in this computation, see Figure 6. The analysis was carried out with a software for numerical computation and visualization, MATLAB ("MATrix LABoratory"). A new evaluation method was developed, which uses

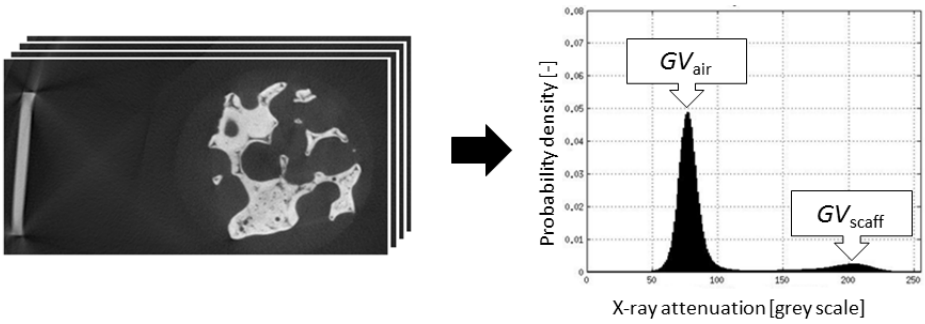

Figure 6: The most frequent grey value representing the materials in the CT image scans are chosen

the unique linear relationship between grey values and X-ray attenuation coefficients with the energy used for the microCT image under consideration. For the 3D modeling of the scaffolds, the 8 bit "TIFF" files were imported to a medical imaging software MIMICS for the 3D scaffolds structure and cell morphology analysation. The data processing started with a procedure of distinguishing the scaffold's material from the background. This technique of finding the object of interest is referred to as segmentation techniques. Any segmentation result is a set of pixels that are related to each other e.g. an object in an image. This set of pixels are usually called segmentation mask or simply mask. The segmentation involves a process of dividing a digital image into several regions (set of pixels). The main goal of segmentation is to produce a binary mask image which fulfils the segmentation criteria. MIMICS is able to create models with any geometry from images delivered as voxel-specific information in terms of 8-bit grey scale. Thus by grouping together similar grey values, the image data can be segmented and the image created. The segmentation procedure is carried out in three steps for a 3D model: thresholding, region growing, and 3D model construction. The first step of the image processing is the "thresholding", it identifies and links together certain regions and materials from the scan data with selection of specific interval of grey values, see Figure 7. The interval of grey values are linked together by the software which results in a highlighted section (mask) of chosen pixels which lie in the selected interval. The grey values interval for the scaffold's visualization is obtained from statistical computation performed in MATLAB for each scaffold separately. The second step is to separate the segmented area from floating pixels, carried out with "region growing". When the mask of the whole 3D scaffold's structure is carried out, a 3D model is created in the software. The 3D model represents the entire scaffold and also the conceivable calcification of the ECM produced by the osteoblastic cells. The volume of the 3D model is extracted of every scaffold in each time sequence and compared together. Specific 3D structure of all the six scaffolds are implemented with 3D modelling in order to investigate the changes/differences in both time sequences of every scaffold. The 3D model represents a lifelike enlarged replica of the scaffolds complex structure.

2.4 SEM Acquisition

Preparation and Observation

In continuation of microCT evaluation, all scaffolds were investigated with LEO Supra 25, Zeiss, scanning electron microscope (SEM), (Department of Materials, Biotechnology, and Energy, Innovation Center, Reykjavik, Iceland) for morphological changes in the cultivation period, 3, 6, and 8 weeks. Images were taken of the upper surface of the 3D scaffolds at an accelerating voltage of 10 kV with different magnification depending on the investigated morphology. With this equipment it was feasible to zoom inside the scaffold's cavities to investigate in more details the ECM production in the time sequences. For the SEM analysation the scaffolds were handled properly, they were dried with a critical point drying device and gold coated with a Sputter Coater equipment and then investigated with the SEM device.

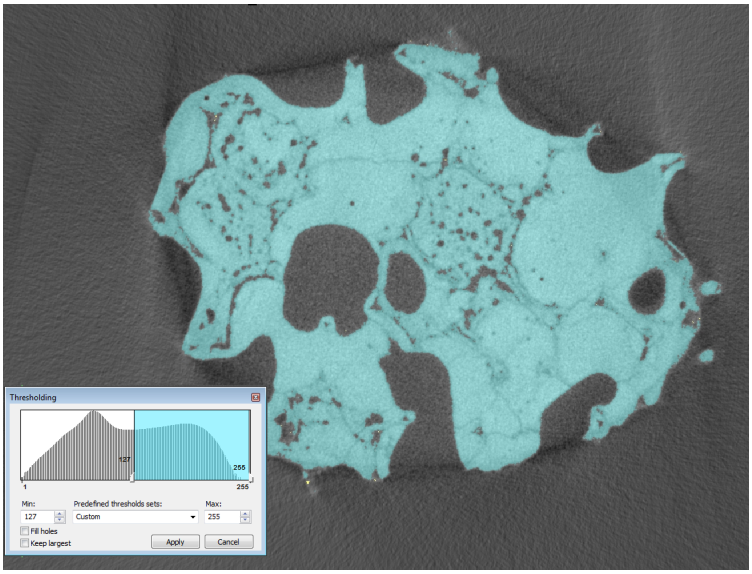

Figure 7: Medical software MIMICS is used in order to visualize the scaffolds structure and create a 3D model in order to identify the entire volume of the scaffold's body in different time of cell culture. In thresholding, grey value interval is selected which represents the scaffold on the 2D CT image slices appearing in blue color

Critical point drying method

All the samples underwent a drying procedure to remove all liquid in a precise and controlled way. A Critical Point Dryer, Bio-Rad, (Department of Materials, Biotechnology, and Energy, Innovation Center, Reykjavik, Iceland), see Figure 8 was used for this task, with a physical principle which is based on a specific temperature and corresponding pressure at a critical point where liquid and vapour coexist with same density. This is necessary in order to keep the biological tissue and the scaffold's fragile structure undamaged during dehydration. During normal air drying, large tension forces are created in small cavities which damages the fragile structure of the scaffold and the weak tissue in it. The main purpose of the critical point is that the transition from liquid to vapour is at that specific point and it happens without density changes. This liquid CO_2/CO_2 gas system is crucial with its stable density of preventing the sample from large tension forces.

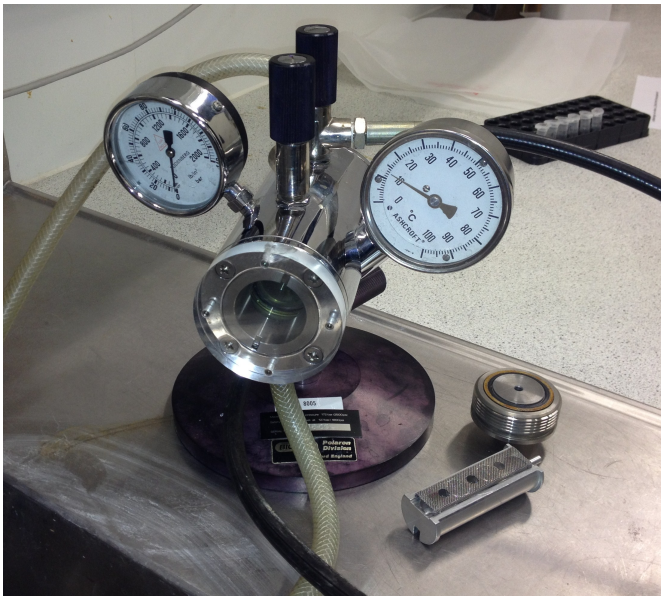

Figure 8: Critical Point Drying system, with a pressure and temperature measuring system on the left and right side, and a small chamber in the middle where the small wire cage is kept during the drying procedure.

Gold coating
After the drying process, the samples were attached to an aluminium small plates put inside a chamber with vacuum within a coating device. This device, named Sputter Coater S150b, Edwards applies Argon gas and small electric field in order to coat the samples with a thin gold layer. Electrons are removed from the atoms of Argon, resulting the Ar atoms ions positively charged. A thin gold foil attracted the Ar ions, thus it had a negatively charged. The Ar ions hit on the thin foil pushing the gold atoms from it which fell onto the surface of the samples creating a thin layer of gold on it, see Figure 9. After coating the samples were put into an SEM device for investigation of the structure of the scaffold and to examine cell morphology on the surface and within superior cavities.

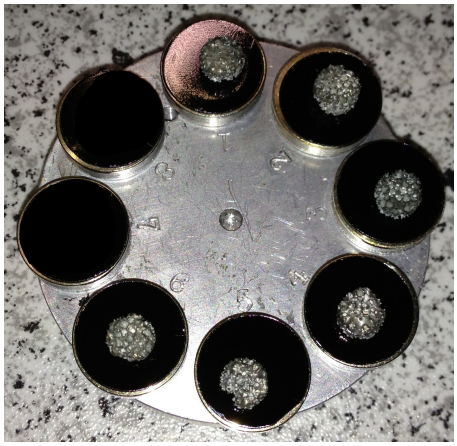

Figure 9: The scaffolds with thin layer of gold coating attached to small aluminium plates ready for the SEM investigation

When both evaluation methods were carried out successfully, the divergent resulting data of the samples

could be compared, see Figure 10.

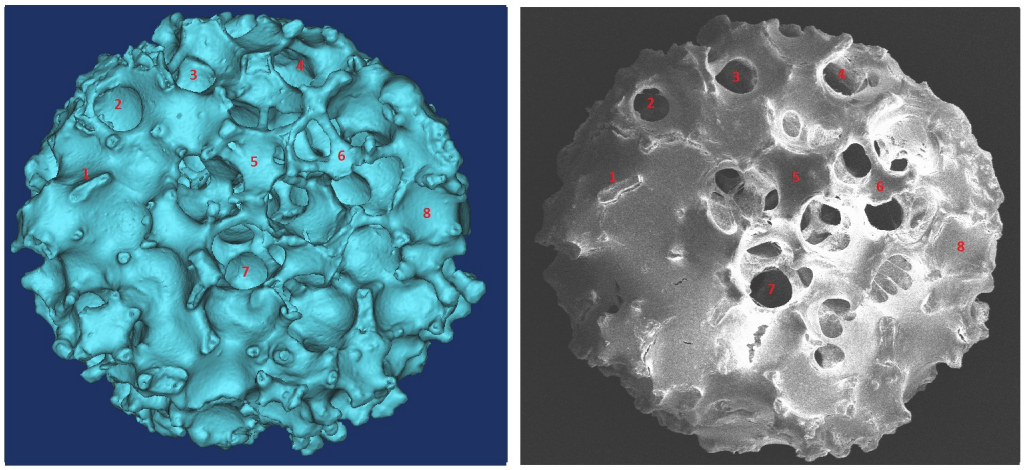

Figure 10: The 3D scaffold's structure is visualized with the medical software MIMICS, shown on left. For comparison of the entire 3D structure, an SEM image is represented on the right. The sample is after 6 weeks of static cultivation. The numbers on the image are representing the identical areas of the 3D scaffold's structure on both images

References

[1] M.S. Stevens M.M. Mwenifumbo, S. Shaffer. Exploring cellular behaviour with multi-walled carbon nanotube constructs. *Journal of Materials Chemistry*, 17:1894 – 1902, 2007.

[2] J.P. Shieh, S.J. Vacanti. State-of-the-art tissue engineering: From tissue engineering to organ building. *Surgery Research Review*, 137:1 – 7, 2005.

[3] U. A. Stock and J. P. Vacanti. Tissue Engineering: current state and prospects. *Annu. Rev. Med.*, 52:443–51, 2001.

[4] A. Poursamar S.A. Azami, M. Samadikuchakasaraei. Synthesis and characterization of a laminated hydroxyapatite/gelatin nanocomposite scaffold with controlled pore structure for bone tissue engineering. *Int J Artif Organs*, 33:86 – 95, 2010.

[5] I.R. Azami M. Khoshzaban A. Tavakol B. Kharrazi S. Ebrahimi S. Sorkhabadi S.M.R. Tavakol, S. Kashani. In vitro and in vivo investigations of bone regeneration potential of laminated hydroxyapatite/gelatin nanocomposite scaffold along with dbm. *J Nanopart Res*, 2012.

[6] Y. Zhao K. Tang Y. Cheng Z Chen J. Zang Y. Wu J. Kong L. Liu S. Lei W. Wu Z. Yu, L. Li. A novel injectible calcium phosphate cement-bioactive glass composite for bone regeneration. *Plos One*, 8, 2013.

[7] M.J. Richards R.G. Hayes J.S. JCzekanska, E.M. Stoddart. In search of an osteoblast cell model for in vitro research. *European Cells and Materials*, 24:1 – 17, 2012.

[8] K. Chawla K. Xiao G. Krebsbach P.H. Franceschi R.T. Wang, D. Christensen. Isolation and characterization of mc3t3-e1 preosteoblasts subclones with distinct in vitro and in vivo differentiation/mineralization potential. *Journal of Bone and Mineral Research*, 14:893 – 903, 1999.

[9] S.S. Purali N. G Korkusuz, P. Hakki.

[10] D. Franceschi R.T. Mooney D.J. Shea, L. Wang. Engineered bone development from a pre-osteoblast cell line on three-dimensional scaffolds. *Tissue Engineering*, 6:605 – 617, 2000.

[11] N. Kifor O. Butters R.R. JR. Sugimoto T. Brown E.M. Yamaguchi, T. Chattopadhyay. Mouse osteoblastic cell line (mc3t3-e1) expresses extracellular calcium (cachemotaxis and proliferation of mc3t3-e1 cells. *Journal of Bone and Mineral Research*, 13, 1998.

[12] R. Vogler E.A. Mastro A.M. Krishnan, V. Dhurjati. Osteogenesis in vitro: from pre-osteoblasts to osteocytes. *The Society for In Vitro Biology*, 46:28 – 35, 2009.

[13] S.A. Cioffi M. Martin I. Wendt, D. Riboldi. Bioreactors in tissue engineering: Scientific challenges and clinical perspectives. *Adv Biochem Engin/Biotechnol*, 112:1 – 27, 2009.

[14] F. Gatenholm P. Concaro, S. Gustavson. Bioreactors for tissue engineering of cartilage. *Adv Biochem Engin/Biotechnol*, 112:125 – 143, 2009.

[15] C.L. Peister A. Oest M.E. Lin A.S.P. Palmer A.W. Levenston M.E. Guldberg, R.E. Duvall. 3d imaging of tissue integration with porous biomaterials. *Biomaterials*, 29:3757 – 3761, 2008.

[16] H.A. Amagai Y. Yamamoto S. Kasai S. Sudo, H. Kodama. In vitro differentiation and calcification in a new clonal osteogenic cell line derived from newborn mouse calvaria. *Journal of Cell Biology*, 96:191 – 198, 1983.

[17] K.W. Chan, B.P. Leong. Scaffolding in tissue engineering: general approaches and tissue-specific considerations. *CEur Spine J*, 17:467–479, 2008.

[18] Y. DiMasi E. Ba X. Rafailovich M. Pernodet N. Meng, Y. Quin. Biomineralization of a self-assembled extracellular matrix for bone tissue engineering. *Tissue Engineering*, 15:355 – 366, 2009.

[19] Y. Markovic B. Barbara J. Howlett R.C. Zhang X. Zreiqat H. Wang, C. Duan. Phenotypic expression of bone-related genes in osteoblasts grown on calcium phosphate ceramics with different phase compositions. *Biomaterials*, 25:2507 – 2514, 2004.

[20] F. Mastrogiacomo M. Cedola A. Papadimitropoulos A. Rustichelli F. Cancedda R. Komlev, V.S. Peyrin. Kinetics of in vivo bone deposition by bone marrow stromal cells into porous calcium phosphate scaffolds: An x-ray computed microtomography study. *Tissue Engineering*, 12:3449 – 3458, 2006.

[21] B. Darling A. Gomez C. Sun, W. Starly. Computer-aided tissue engineering: application to biomimetic modelling and design of tissue scaffolds. *Biotechnol. Appl. Biochem.*, 39:49 – 58, 2004.

[22] C.E. Atala A. Kim, B.S Baez. Biomaterials for tissue engineering. *World J Urol*, 18:2–9, 2000.

[23] N. Appleford M. Ong J.L. Oh, S. Oh. Bioceramics for Tissue Engineering Applications - A Review. *American Journal of Biochemistry and Biotechnoloty*, 2:49–56, 2006.

[24] F. Peyrin. Evaluation of bone scaffolds by micro-CT. *Osteoporos Int*, 22:2043 – 2048, 2011.

[25] DICOM PS3.3 2013 - Information Object Definitions. 2013.

[26] J.H. Hubbell. Photon mass attenuation and energy-absorption coefficients. *The international Journal of Applied Radiation and Isotopes*, 33(11):1269–1290, 1982.

[27] S.M. Seltzer. Calculation of photon mass energy-transfer and mass energy-absorption coefficients. *Radiation Research*, 136(2):147–170, 1993.

[28] North Star Imaging, Computed Tomography.

[29] J.S. Correia C. Caridade S.G. Fernandes E.M. Sousa R.A. Mano J.F. Oliveira A.L. Reis R.L. Yan, L.P. Correia. Bioactive macro/micro porous silk fibron/nano-sized calcium phosphate scaffolds with potential for bone-tissue-engineering applications. *Nanomedicine*, 8:359 – 378, 2013.

[30] S. T. Ho and D. W. Hutmacher. A comparison of micro CT with other techniques used in the characterization of scaffolds. *Biomaterials*, 27(8):1362–1376, 2006.

3 Appendix

3.1 Paper: Quantitative Intravoxel Analysis of microCT-Scanned Resorbing Ceramic Biomaterials - Perspectives for Computer-Aided Biomaterial

This thesis has a core of a paper which has been submitted 1st. June, 2014 to the *Journal of Materials Research* in a materials area on the micro- and nanomechanics analysis.

Quantitative intravoxel analysis of microCT-scanned resorbing ceramic biomaterials - Perspectives for computer-aided biomaterial design

Journal:	*Journal of Materials Research*
Manuscript ID:	Draft
Manuscript Type:	Invited Feature Paper
Date Submitted by the Author:	n/a
Complete List of Authors:	Czenek, Agnes; Vienna University of Technology , Department of Civil Engineering; Reykjavik University, Institute of Biomedical and Neural Engineering; Landspitali University Hospital, Department of Science Blanchard, Romane; Vienna University of Technology, Department of Civil Engineering Dejaco, Alexander; Vienna University of Technology , Department of Civil Engineering Sigurjónsson, Ólafur; Reykjavik University, Institute of Biomedical and Neural Engineering Örlygsson, Gissur; Innovation Center Iceland, Department of Materials, Biotechnology and Energy Gargiulo, Paolo; Reykjavik University, Institute of Biomedical and Neural Engineering; Landspitali University Hospital, Department of Science Hellmich, Christian; Vienna University of Technology, Department of Civil Engineering
Key Words:	biomaterial, x-ray tomography, elastic properties

Quantitative Intravoxel Analysis of microCT-Scanned Resorbing Ceramic Biomaterials - Perspectives for Computer-Aided Biomaterial Design

Agnes Czenek[a,b,c], Romane Blanchard[a], Alexander Dejaco[a], Ólafur E. Sigurjónsson[b,d], Gissur Örlygsson[e], Paolo Gargiulo[b,c], Christian Hellmich[a*]

[a]Institute for Mechanics of Materials and Structures, Vienna University of Technology (TU Wien), Austria
[b]Institute of Biomedical and Neural Engineering, Reykjavik University, Iceland
[c]Department of Science, Landspitali University Hospital, Iceland
[d]REModel Lab, The Blood bank, Landspitali University Hospital, Iceland
[e]Department of Materials, Biotechnology and Energy, Innovation Center Iceland, Iceland

Abstract

Driving the field of micro Computed Tomography towards more quantitative, rather than qualitative, approaches, we here present a new evaluation method, which uses the unique linear relationship between grey values and X-ray attenuation coefficients, together with the energy-dependence of the latter, in order to identify (i) the average X-ray energy employed in the CT device, (ii) the X-ray attenuation coefficients, and (iii), via the X-ray attenuation average rule, the intravoxel composition, i.e. the nanoporosity, which, amongst others, governs the voxel-specific mechanical properties, such stiffness and strength. The method is realized for six 3D tricalcium phosphate scaffolds, seeded with pre-osteoblastic cells and differentiated for 3, 6, and 8 weeks, respectively. The corresponding voxel-specific nanoporosities turn out to increase during the culturing period (resulting in reduced elastic properties, as determined from micromechanical considerations), while the overall macroporosity remains constant. The new methods is expected to further foster the development of a rationally based and computer-aided design of biomaterials and tissue engineering scaffolds.

Keywords

Tissue engineering scaffold, continuum micromechanics, Computed Tomography, X-ray physics, bone biomaterials, tri-calcium phosphate

*Corresponding author. Tel.: +43 1 58801 20220; fax: +43 1 58801 20299
Email address: christian.hellmich@tuwien.ac.at (Christian Hellmich)

I. INTRODUCTION

Micro-Computed Tomography (microCT) has become a standard tool in biomaterial characterization. It allows for assessment of pore morphology[1,2], for quantifying the newly formed bone tissue in tissue engineering scaffolds[3,4,5], and the identified topology has been used to feed various types of numerical analyses, being related to elastic properties[6,7], to permeability[8,9], or to mechanobiology[10,11].

All these approaches are based on some kind of statistical evaluation of the grey values standardly defining the three-dimensional CT "images", while the deeper physical meaning of these grey values remains somewhat unconsidered. Actually, these voxel-specific grey values, being defined on 8-bit or 16-bit scales, are proportional to the X-ray attenuation coefficient of the material found within the respective voxel. The X-ray attenuation coefficient, in turn, measures the relative decrease of X-ray beam intensity per length of pervaded matter, and it is a function of the chemical composition of that matter - the latter being of obvious interest for the materials scientist, biomedical engineer, or clinician; and it is the key issue to be tackled in the present paper.

However, the proportionality constants defining the aforementioned relation between grey values and attenuation coefficients are standardly neither documented nor disclosed with the available commercial equipment, and in addition, the X-ray attenuation coefficients are no material properties in a strict sense, but depend on the used X-ray energy. In the sequel, we will present a novel method for retrieving both the proportionality constants and the used X-ray energy, from statistical analyses performed on the grey values imaging ceramic biomaterials, in combination with fundamental X-ray physics, comprising chemistry-attenuation relations published by NIST[12,13,14] on the one hand, and the volume average rule for X-ray attenuation coefficients[15,16] on the other hand. Thereby, the key ingredient of the analysis will be the unique existence of one X-ray energy (or of the peak of one X-ray energy spectrum) used for the 3D CT image under consideration. From an applied perspective, the

method will provide an answer to the following question: Does cell culturing of ceramic biomaterials in physiological fluid not only affect the several-hundred-microns-to-a-few-millimeters-sized pores provided for tissue ingrowth, but also alter the nanostructure of the solid phase of the ceramic scaffold, i.e. does culturing also increase the nanoporosity found in each and every solid scaffold voxel? Finally, the paper will be concluded by a broader perspective concerning future application of the presented method, together with an overview on how it relates to former "landmark" contributions in the field – all paving the way to a more mature, computer-aided biomedicine in general, and biomaterial design in particular.

II. MATERIALS AND METHOD

A. Test protocol

As typical ceramic biomaterials for bone tissue engineering, we consider six 3D beta-tri-calcium phosphate (β-TCP) scaffolds (Becton, Dickinson and Company, La Jolla, CA, USA), with an average pore size of 200-400 microns. The samples, installed in plastic flacon tubes together with a phantom of aluminum, were scanned by means of a Phoenix Nanotom S (General Electric Measurement and Control, X-ray microCT system) at Innovation Center Iceland, Reykjavík, Iceland, at a source current of 160 μA, a source voltage of 90 kV, and a sampling distance of 7.33 microns. The β-TCP scaffolds underwent the following protocol: First, they were scanned as produced, i.e. with empty pores. Then, they were seeded with the pre-osteoblastic cell line MC3T3-E1 (clone 4; ATCC, Wesel, Germany) and cultured in an alpha-minimum medium (α-MEM) containing 10 % fetal bovine serum (FBS; Lifetechnologies, Boston, MA, USA) mixed with Ascorbic Acid and β-Glycerophosphate (Glucerol 2-phospate disodium salt hydrate; Sigma-Aldrich Chemie GmbH, Taufkirchen, Germany) at 37°C, 5% CO_2 and 95% relative humidity (RH), for 3, 6, and 8 weeks, respectively. The cell-containing scaffolds were then washed in phosphate buffered saline (PBS), fixed with paraformaldehyde (4% v/v), subjected to a dehydration gradient with an

increasing concentration of ethanol, and finally kept in 96% ethanol until further use. The latter consisted of re-installing them into plastic flacons, this time filled with ethanol as well, in order to scan the scaffolds once again. Eventually, they were dried in a CO_2 Critical Point Dryer (Bio-Rad Polaron Division, Watford, England) before being coated by a conductive layer of sputtered gold for further investigation by means of scanning electron microscopy (SEM; LEO Supra 25, Zeiss, Oberkochen, Germany). Respective micrographs were taken at an accelerating voltage of 10 kV, at different magnifications. Anticipating, for the sake of more clearly developing the remaining methods sections, two such micrographs in Figure 1, we observe that the investigated scaffolds exhibit a double porous nature: ”large“, several-hundreds-micrometers-to-a-few-milimeter-sized ”macropores“ can be clearly distinguished from sub-micrometer-sized ”nanopores“. Micro Computed Tomography will allow for detailed resolution of the ”macropores“, while the nanopores will govern the ”density“ of the individual microCT voxels.

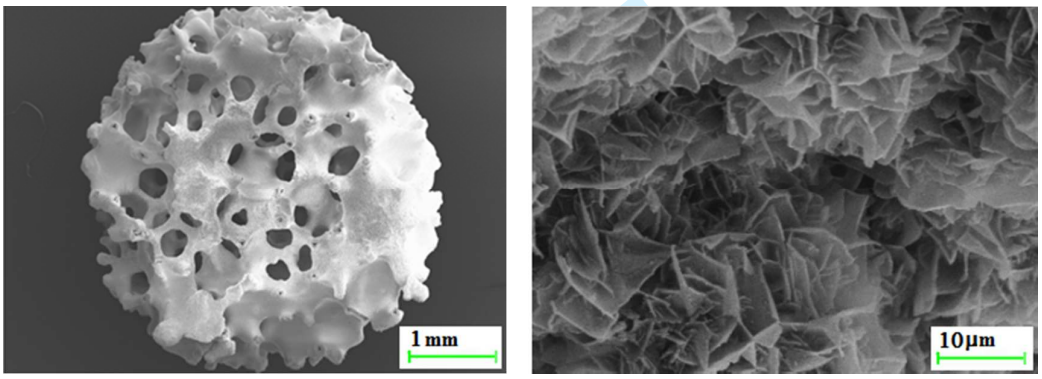

FIG. 1. Double porous structure of investigated ceramic biomaterial, as revealed by means of Scanning Electron Microscopy: (a) “macropores” of several hundreds of micrometers size, and (b) “nanopores” at the sub-micrometer scale

B. MicroCT evaluation procedure I: conversion of CT grey values to energy-dependent attenuation coefficients, based on air and aluminum characteristics

Radon transform-based reconstruction[17,18] of X-ray projection images recorded by the microCT scanner delivers a 3D image consisting of cubes called voxels, which are characterized by 8-bit grey values being related to the X-ray attenuation coefficients. The

latter relation is a linear one, with coefficients a and b depending on the photon energy $\mathcal{E}$ used in the scanner[19],

$$\mu(\mathcal{E})=a(\mathcal{E}) \times GV+b(\mathcal{E}), \quad (1)$$

Coefficients a and b are standardly not disclosed by a conventional CT equipment, and we will retrieve them from a statistical image analysis in combination with knowledge on the chemical nature of the scanned materials. Therefore, probability density plots of all the grey values found in each of the investigated 3D images are used, in order to identify several landmark values in each of these histograms:

- The leftmost peak of each histogram indicates the most frequent grey value in the image domain illustrating the air which surrounds the depicted scaffold; this grey value is denoted as GV_{air};
- The peak on the right side of each histogram indicates the most frequent grey value of all the voxels containing solid scaffold material, this grey value is denoted as GV_{scaff}^{peak}.
- As a third landmark, the grey value of the aluminum phantom scanned simultaneously with the ceramic scaffold is identified. Since it cannot be determined as a peak on any of the histograms concerning the overall images, the image domains illustrating the phantom material were cropped, and the most frequent grey values occurring in each of these subdomains, denoted as GV_{Al}, was identified.

The X-ray attenuation coefficients of the materials related to the landmark points can be retrieved from the NIST-database of mass attenuation coefficients μ/ρ [12], based on the mass densities of air, ρ_{air} = 0.0012 g/cm^3, of pure β-TCP, $\rho_{\beta\text{-}TCP}$ =3.07 g/cm^3, of ethanol, $\rho_{C_2H_6O}$ = 0.789 g/cm^3, and of aluminum, ρ_{Al} = 2.699 g/cm^3, see Figure 2 for their dependence on the X-ray energy $\mathcal{E}$.

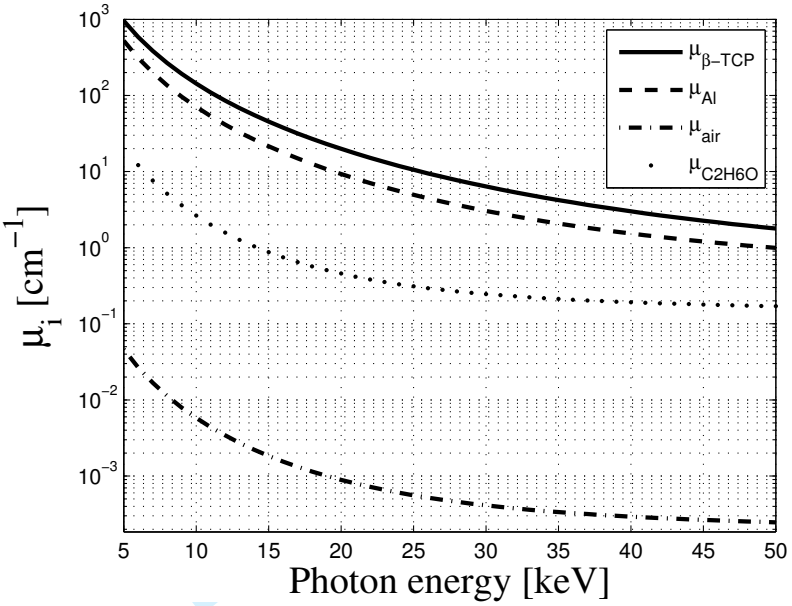

FIG. 2. X-ray attenuation coefficients of pure β-TCP, of aluminum, of ethanol, and of air, as functions of the photon energy $\mathcal{E}$

Specification of Eq. (1) for the attenuation coefficients and the grey values of air and of aluminum, μ_{air} and μ_{Al}, as well as GV_{air} and GV_{Al}, respectively, yields a linear system of equations for the energy-dependent coefficients *a* and *b,*

$$\begin{cases} \mu_{air}^{NIST}(\mathcal{E}) = a(\varepsilon) \times GV_{air} + b(\mathcal{E}) \\ \mu_{Al}^{NIST}(\mathcal{E}) = a(\varepsilon) \times GV_{Al} + b(\mathcal{E}) \end{cases} \quad (2)$$

with the solution,

$$\begin{cases} a(\mathcal{E}) = \left[\mu_{air}^{NIST}(\mathcal{E}) - \mu_{Al}^{NIST}(\mathcal{E})\right] / \left[GV_{air} - GV_{Al}\right] \\ b(\mathcal{E}) = \left[(\mu_{air}^{NIST}(\mathcal{E}) \times GV_{Al} - \mu_{Al}^{NIST}(\mathcal{E}) \times GV_{air}\right] / \left[GV_{Al} - GV_{air}\right] \end{cases} \quad (3)$$

Coefficients $a(\mathcal{E})$ and $b(\mathcal{E})$ allow for energy-dependent conversion of grey values to X-ray attenuation coefficients according to Eq.(1).

C. MicroCT evaluation procedure II: identification of used photon energy and of intravoxel nanoporosity, based on attenuation average rule applied to nanoporous ceramic

In order to identify the actual values for the coefficients *a* and *b*, we explicitly consider that relation (1) needs to be unique, i.e. per used photon energy $\mathcal{E}$ only one pair of coefficients *a* and *b* exists. Accordingly, value-specific, rather than function-specific, identification of *a* and *b* is based on deriving and then setting equal, of two independent expressions for the photon energy-dependent X-ray attenuation coefficient of the most frequently occurring grey value in the scaffold domain. The first expression relates to the average rule for X-ray attenuation coefficients[15,16], which when applied to the matter found within a scaffold voxel, reads as

$$\mu_{scaff}^{up}=\mu_{\beta\text{-}TCP}(1-\phi)+\mu_{air}\phi \qquad (4)$$

in the case of untreated (empty) scaffolds, and

$$\mu_{scaff}^{up}=\mu_{\beta\text{-}TCP}(1-\phi)+\mu_{C_2H_6O}\phi \qquad (5)$$

in the case of cultured scaffolds, with ϕ as the voxel-specific nanoporosity found within one voxel, and $\mu_{C_2H_6O}$ as the attenuation coefficient of ethanol. Superscript "up" indicates that Eqs.(4) and (5) allow for up-scaling of physical quantities (here attenuation coefficients) from the sub- or intra-voxel level, up to the level of the entire voxel.

The second expression for the most frequently encountered attenuation value found in the scaffold image domain results from respective specification of Eq.(1),

$$\mu_{scaff}^{up}=a(\mathcal{E})\times GV_{scaff}^{peak}+b(\mathcal{E}) \qquad (6)$$

Setting Eq.(6) equal to specifications of (4) and (5) for the most frequently encountered nanoporosity value, denoted as ϕ^{peak}, yields an equation in the format,

$$a(\mathcal{E})\times GV_{scaff}^{peak}+b(\mathcal{E})=\mu_{\beta\text{-}TCP}\times(1-\phi^{peak})+\mu_i\times\phi^{peak} \qquad (7)$$

with *i* = air for the untreated (empty) scaffolds, and *i* = C_2H_6O otherwise. Eq. (7) establishes a non-bijective function between ϕ^{peak} and $\mathcal{E}$: it assigns none, or one, or two values of $\mathcal{E}$ to a specifically chosen value for ϕ^{peak}.

However, only one photon energy was used in any of the considered images, so that only the one unique solution which is related to only one value for the photon energy, remains physically admissible. This gives access to both the photon energy $\mathcal{E}$ used for the considered image, and to the most frequently encountered nanoporosity value, ϕ^{peak}. Once knowing the unique value for the photon energy $\mathcal{E}$, all grey values encountered in the images can be converted into attenuation coefficients μ, by means of Eq.(1) with now *known* functions $a(\mathcal{E})$ and $b(\mathcal{E})$. Use of these attenuation coefficients in average rules (4) and (5) finally yields voxel-specific nanoporosities according to

$$\phi = \left(\mu - \mu_{\beta\text{-}TCP}\right) / \left(\mu_i - \mu_{\beta\text{-}TCP}\right) \quad (8)$$

with i = air for the untreated (empty) scaffolds, and $i = C_2H_6O$ otherwise.

D. MicroCT evaluation III: micromechanics-base nanoporosity-to-elastic conversion

Porosity is well-known to strongly govern the mechanical properties of a material[20]. Our present focus is on the nanoporous β-TCP polycrystal found in each and every voxel of the 3D micro Computer Tomographs of the investigated bioceramic scaffolds. As identified in Figure 1(b) the β-TCP crystals are of disc-type shape. A recent micromechanics study[21], based on self-consistent estimates for infinitely many, spatially oriented crystal phases[22,23,24,25] and validated on a variety of ceramic material systems[26,27,28,29,30,31,32,33,34,35] has revealed the Young's modulus E of such disc-composed porous polycrystals to closely follow a power law relation with the (nano)porosity as argument,

$$E/E_s = B_E(1-\phi)^{C_E} \quad (9)$$

with E_s as the Young's modulus of a pure beta-TCP crystal (which was quantified through molecular dynamics analysis as $E_s = 110$ GPa[36]), and the power function constants B_E and C_E amounting to 0.9867 and 2.053, respectively[21]. Full elastic characterization of the isotropic polycrystal found in each and every voxel also requires knowledge of Poisson's ratio v, which

can again be predicted from the aforementioned self-consistent micromechanics approaches (realized with empty pores), and closely approximated by a fourth-order polynomial,

$$v(v_s) \approx \overline{A}_v \times (1-\phi)^4 + \overline{B}_v \times (1-\phi)^3 + \overline{C}_v \times (1-\phi)^2 + \overline{D}_v \times (1-\phi) + \overline{E}_v \quad (10)$$

Coefficients $\overline{A}_v$, $\overline{B}_v$, $\overline{C}_v$, $\overline{D}_v$ and $\overline{E}_v$ of fourth-order polynomial approximation of v^{hom} depend linearly on v_s,

$$q = a^* \times v_s + b^* \quad (11)$$

Table I: Proportionality constants a^* and b^* defining, according Eq.(11), the polynomial coefficients $\overline{A}_\nu$, $\overline{B}_\nu$, $\overline{C}_\nu$, $\overline{D}_\nu$, and $\overline{E}_\nu$ for approximation, according to Eq.(10), of Poissons ratio of single crystal v_s

Disks		
	a^*	b^*
$\overline{A}_v$	-1.0521	0.2197
$\overline{B}_v$	2.2684	-0.4645
$\overline{C}_v$	-0.8121	0.1662
$\overline{D}_v$	0.3602	-0.0718
$\overline{E}_v$	0.2394	0.1496

see Table I for corresponding numbers, and the pure crystals Poisson‘s ratio, v_s=0.276, is again known from molecular dynamics[36]. Equations (9), (10), and (11) allow for conversion of the voxel-specific nanoporosities as derived from Eq. (8) into voxel-specific elastic properties.

F. MicroCT evaluation IV: macroporosity quantification

The voxels characterized by 8-bit grey scale are imported into the medical imaging segmentation software MIMICS (Materialise, Leuven, Belgium) for analysis of the macroporosity quantification, or more precisely, of the change of the volume of the (nanoporous) scaffold material due to treatment. Therefore, for each micro Computed Tomograph, a segmentation process based on the respective grey value histogram is performed: The minimum probability value left of the scaffold peak value GV_{scaff}^{peak} is identified as threshold value GV_{thr}, and all voxels with grey values larger than this threshold are considered as "scaffold material voxels". Then, a 3D model is created of the segmented area, for each scaffold, both before and after cultivation. Finally, the volumes of all the 3D models were computed, and values referring to time points before and after cultivation were compared.

III. RESULTS

Low magnification scanning electron micrographs (see Figure 3) clearly show covering of the scaffolds' surfaces with pre-osteoblastic cells, once the latter were seeded on the former. During ongoing cultivation, the cellular cover tends to grow denser, as is seen in the higher magnification SEMs of Figure 4: initially loose fibrous networks of cell processes [as seen after 3 weeks of cultivation, see Figure 4(a,b)], finally turn into more compact extracellular matrix after 8 weeks [as seen in Figure 4(c,d)], which finally even tends to cover the originally protruding cell nodules [see Figure 4(e,f)]. Further insight into the effects of the cultivation process results from studying the micro Computed Tomographs:

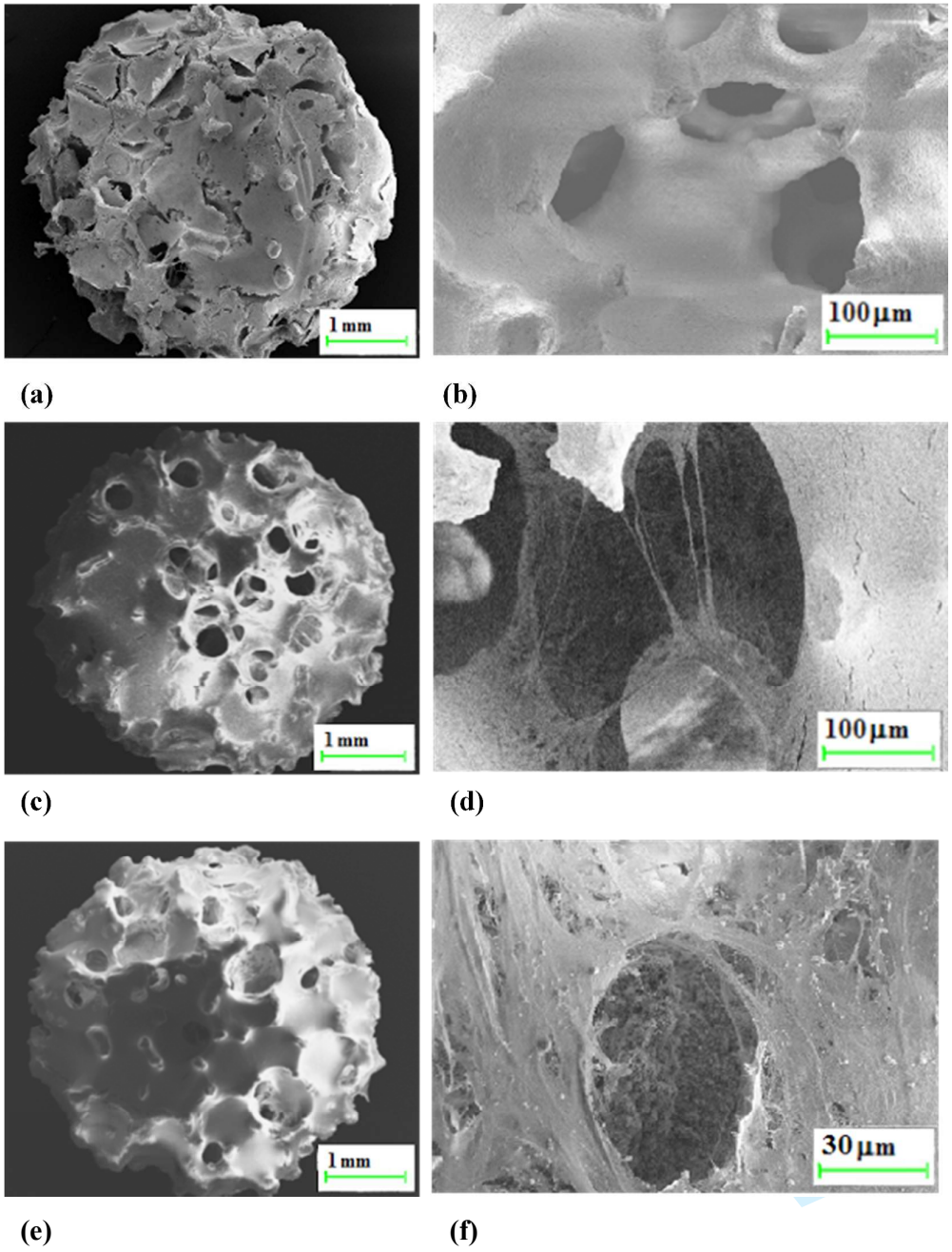

FIG. 3. Cell proliferation on ceramic scaffolds as revealed by SEM, at low magnification showing entire scaffolds with approximately 5 mm diameter (a,c,e), and at high magnification zooming into one of the "macropore" cavities (b,d,f): comparison of cell covers after 3 weeks of cultivation (a,b), with the situations after 6 weeks (c,d), and after 8 weeks (e,f)

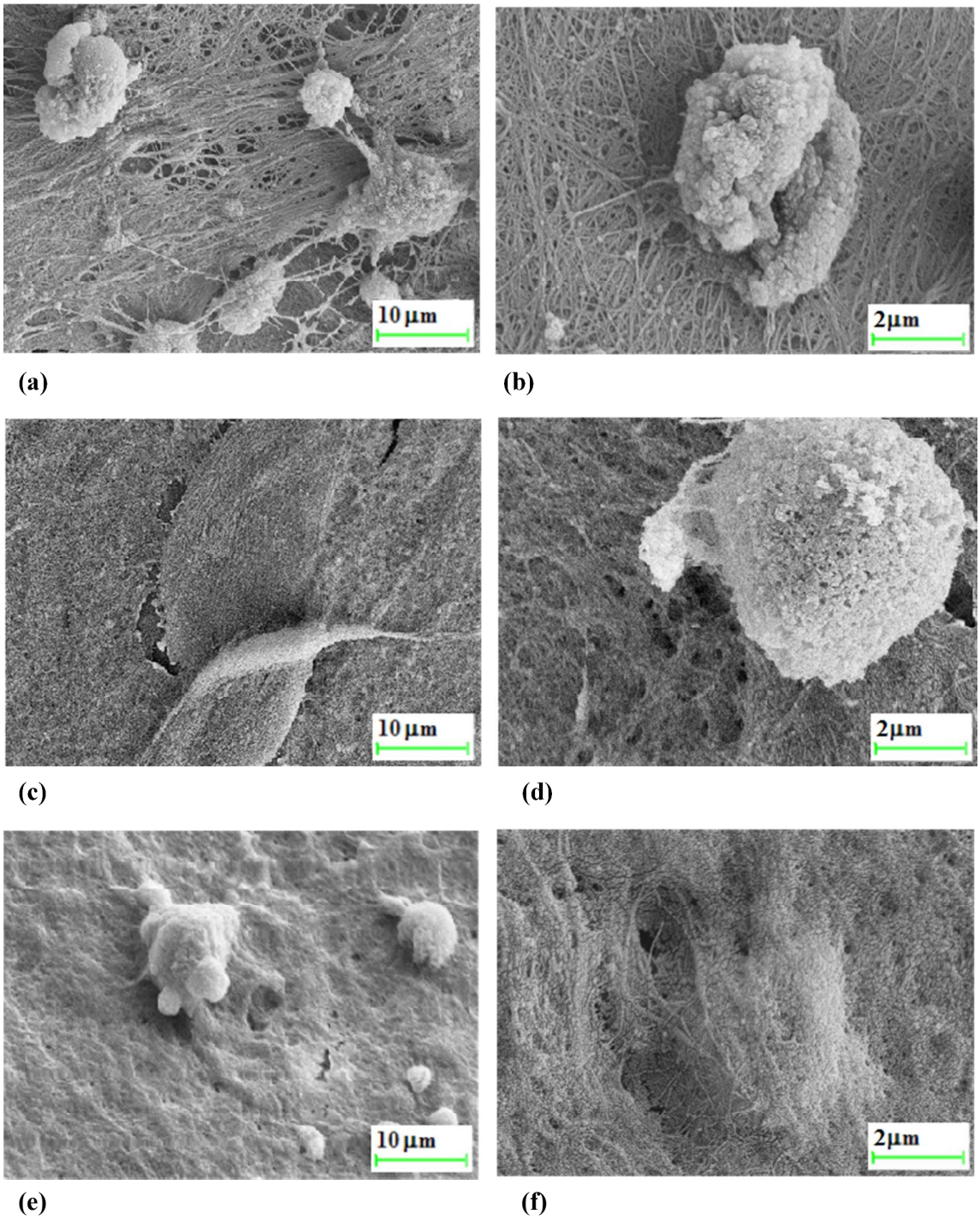

FIG. 4. SEM-based close up of immediate vicinity of a cell nodule: after 3 weeks (a,b), after 6 weeks (c,d), and after 8 weeks (e,f)

Histograms of all CT images of the six investigated scaffolds, in untreated and cultured conditions, respectively, show a large number of grey values referring to low-density voxels

(typically with GV<100), and a smaller number of denser voxels referring to the ceramic scaffold material, see Figures 5.

Before treatment in pseudo-physiological conditions, the low density voxels show one (or one dominant) peak, which is related to the attenuation of air alone, GV_{air}, while sometimes the plastic flacon-induced attenuation effects are explicitly visible as well, as seen in Figure 6(c,d,e). After cultivation and scanning in ethanol, the situation changes insofar, as a large number of ethanol-filled voxels emerge, which always leads to two clearly distinguishable peaks in the low density grey value range of the respective histograms, see Figure 5(g-l). Thereby, the left of these peaks refers to air, and the respective right one represents ethanol-filled voxels inside the plastic flacon tube.

The most frequent grey values found, respectively, in the image domains showing air, GV_{air}, scaffold material, GV_{scaff}^{peak}, and aluminum, GV_{Al}, are varying between all investigated scaffolds, be they treated or untreated, see Table II.

Interestingly, there does not emerge any additional peak which would be related to a material with densities somewhere between those of ethanol (or soft tissue) and of ceramic: this clearly shows that the cellular cover on the macropore and the outer surfaces of the scaffolds did not mineralize.

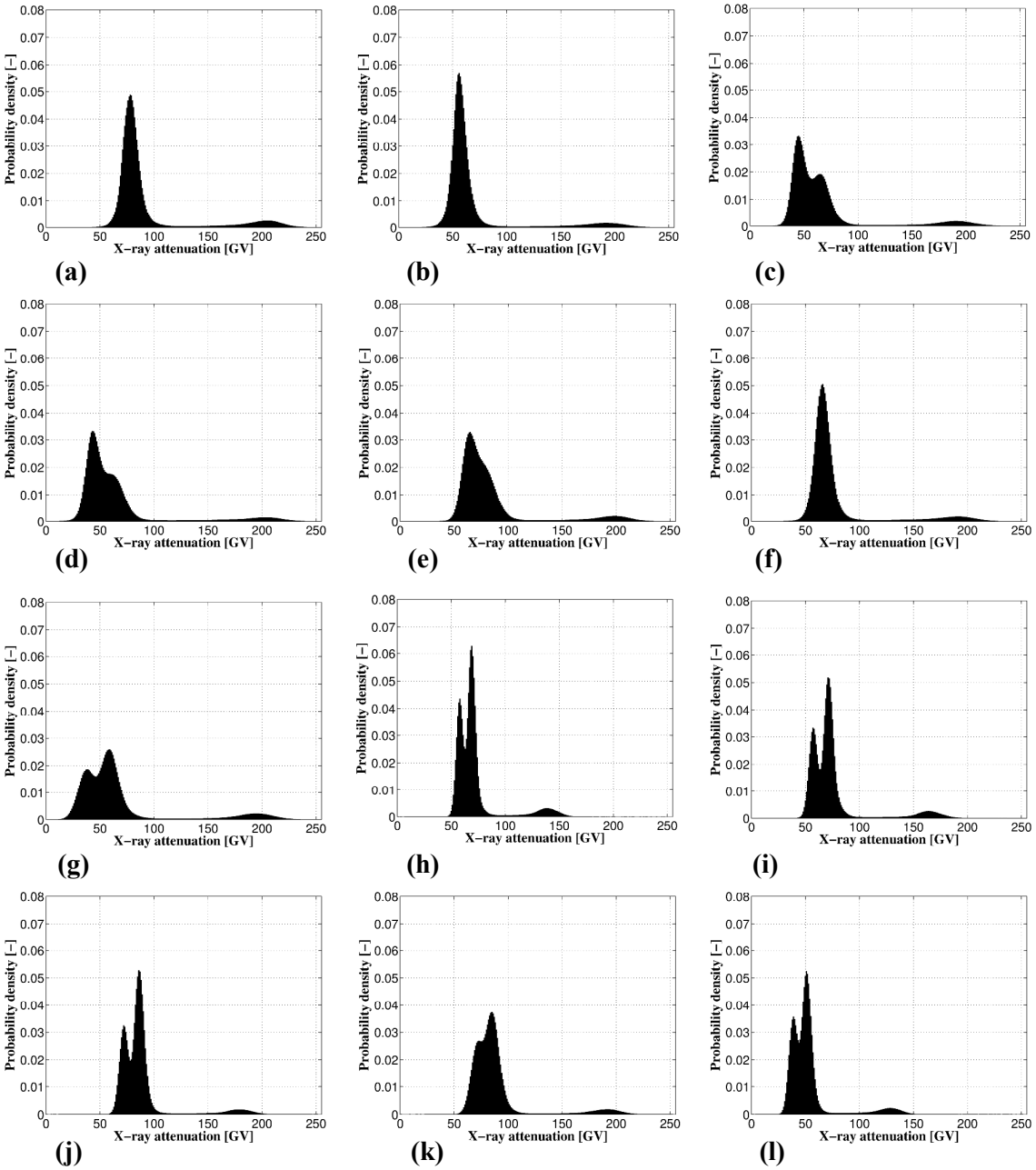

FIG. 5. Probability density function of attenuation-related grey values of six CT-imaged β-TCP scaffolds, before cell culturing (a-f): (a) sample I, (b) sample II, (c) sample III, (d) sample IV, (e) sample V, (f) sample VI; and after cell culturing (g-l): (g) sample I after 3 weeks of culturing, (h) sample II after 3 weeks of culturing (i) sample III after 6 weeks of culturing, (j) sample IV after 6 weeks of culturing, (k) sample V after 8 weeks of culturing, (l) sample VI after 8 weeks of culturing

Table II: Landmark grey values of scaffolds before and after cultivation

	Before Cultivation						After Cultivation					
Samples	I	II	III	IV	V	VI	I	II	III	IV	V	VI
GV_{air}	77	55	44	42	64	65	37	57	56	71	71	39
GV_{Al}	165	157	168	165	163	144	184	133	155	171	177	122
GV_{scaff}^{peak}	204	193	190	203	196	191	194	138	163	178	191	128
GV_{thr}	127	209	111	113	125	115	115	97	111	122	127	81

When continuing with the image evaluation steps as described in Section II.B, we find that the proportionality constants a and b relating grey values to attenuation coefficients as given in Eq.(1) emerge as decreasing functions of the photon energy, as depicted in Figure 6(a,b), plotted based on Eq.(3) fed by the data shown in Table II.

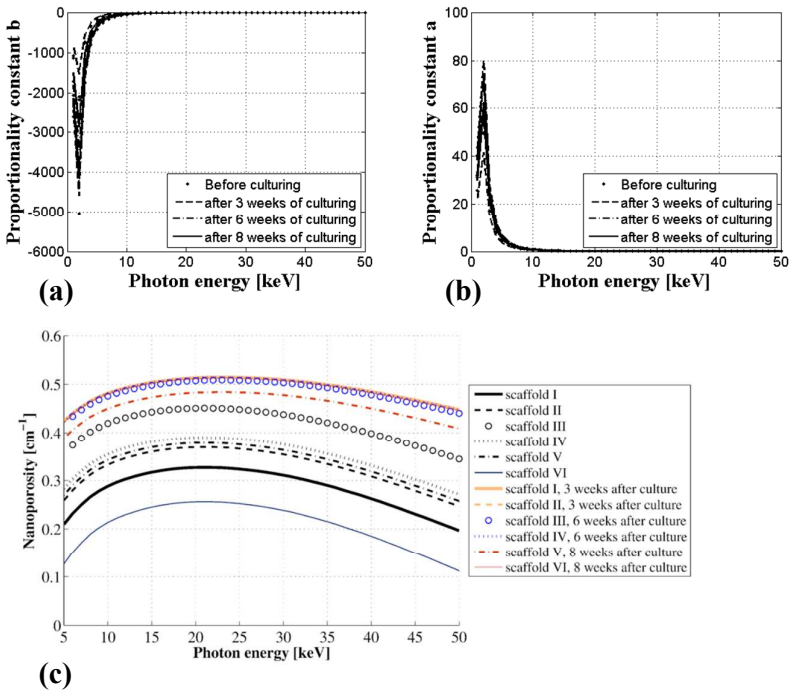

FIG. 6. (a,b) Proportionality constants relating grey values to attenuation coefficients, as functions of the photon energy $\mathcal{E}$; (c) scaffold-specific ϕ^{peak} - $\mathcal{E}$ - relations, used for identification

of scanner-specific employed photon energy and actual value of most frequently occurring nanoporosity

Use of these functions in the identity of upscaled and grey value-determined attenuation coefficients, as given through Eq.(7), yields $\mathcal{E}$ - ϕ^{peak} - relations as depicted in Figure 6(c). They are used to identify, for each microCT image, the only value of $\mathcal{E}$ which is uniquely related to just one value of ϕ^{peak} : $\mathcal{E}$ = 21 keV – this is the (average) photon energy used for all the images. The corresponding ”peak“ nanoporosities per investigated scaffold are again scaffold-specific, and increase through treatment, see Table III.

Table III: Most frequently occurring, i.e. “peak” nanoporosities in each scaffold, before and after cultivation

scaffold number	I	II	III	IV	V	VI
before cultivation	0.327	0.369	0.451	0.390	0.379	0.257
after cultivation	0.515	0.516	0.508	0.514	0.484	0.513

This increase can be studied for all the voxels of all the investigated scaffolds, as depicted in the nanoporosity maps of Figures 7 to 9:

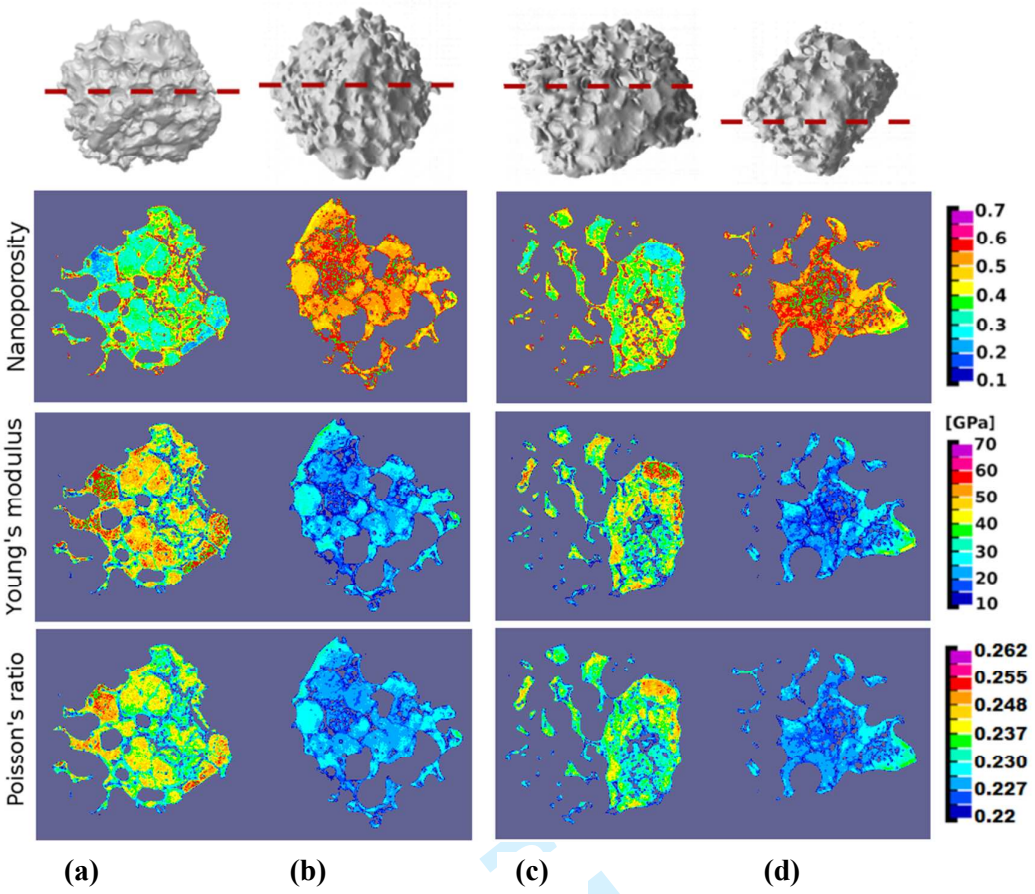

FIG. 7. Spatial distributions of voxel-specific nanoporosity and elastic properties, i.e. Young's modulus and Poisson's ratio, over chosen cross sections through: sample I before culturing (a), sample I after 3 weeks of culturing (b), sample II before culturing (c), sample II after 3 weeks of culturing (d)

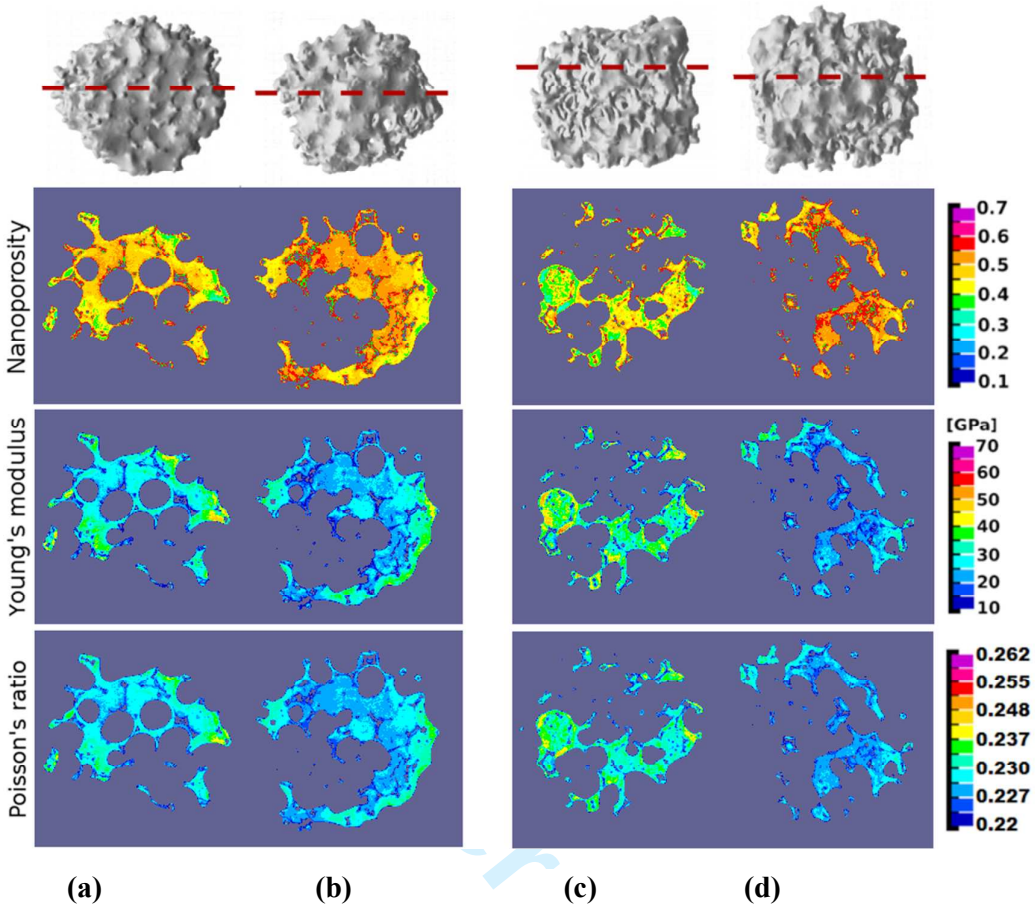

FIG. 8. Spatial distributions of voxel-specific nanoporosity and elastic properties, i.e. Young's modulus and Poisson's ratio, over chosen cross sections through: sample III before culturing (a), sample III after 6 weeks of culturing (b), sample VI before culturing (c), sample VI after 6 weeks of culturing (d)

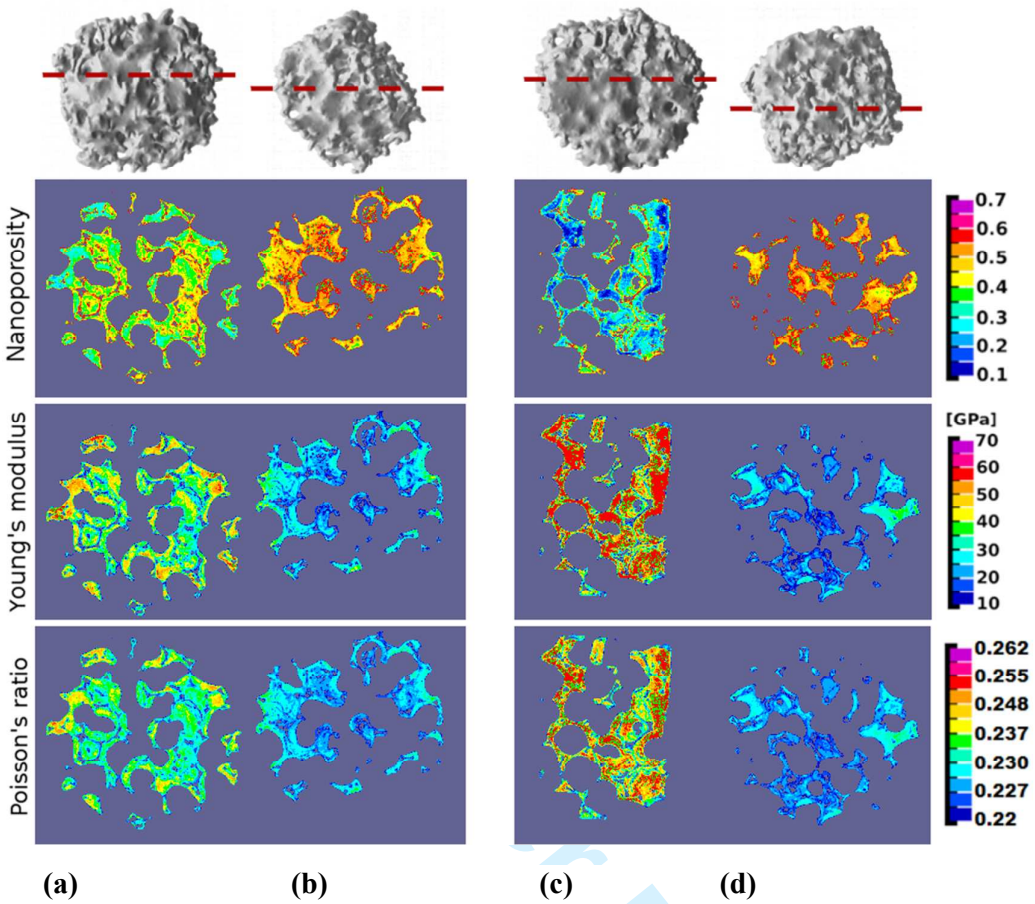

FIG. 9. Spatial distributions of voxel-specific nanoporosity and elastic properties, i.e. Young's modulus and Poisson's ratio, over chosen cross sections through: sample V before culturing (a), sample V after 8 weeks of culturing (b), sample VI before culturing (c), sample VI after 8 weeks of culturing (d)

Due to the highly overlinear effect of the nanoporosity on the Young's modulus as quantified through Eq.(9), the nanoporostiy increase turns out as quite detrimental for the scaffolds' local stiffnesses (see Figures 7 to 9), while the voxel-specific Poisson's ratio is also decreasing, i.e. tending towards 0.2 (see Figure 7 to 9). At the same time, the macroporosities remain fairly constant, as the results of the volume analysis in Table IV show (for corresponding theshold values GV_{thr} used for segmentation, we refer to Table II).

Table IV: Change in volume (mm^3) of the 3D scaffold's body, due to cultivation

Scaffolds volume (mm^3)	I	II	III	IV	V	VI
Before Cultivation	33.02	39.54	30.09	22.36	29.02	25.55
After Cultivation	34.90	40.04	28.85	21.39	28.34	26.05
Change in Volume	6%	1%	-4%	-4%	-2%	2%

IV. DISCUSSION, REVIEW, AND PERSPECTIVES

Due to its non-destructive character and its ability to "look deeply" into actually "non-transparent solid microstructures", micro Computed Tomography has become a key tool for the morphological study of biomaterials and tissue engineering scaffolds during the last decade. In the context of calcium phosphate or hydroxyapatite biomaterials, microCT studies allowed for quantification, in time and space, of newly formed bone tissue within in vivo implanted ceramic biomaterials[37,38,39,40,41,42,43,44,45]. Such analyses are based on segmentation of the grey value-characterized voxels of the micro Computer Tomographs into different subdomains which are defined to lie between certain reasonably chosen threshold values. In the context of bone tissue engineering, the aforementioned subdomains then related to bone tissue, ceramic material, or pore fluid, respectively. In this sense, the voxels within any of these subdomains are not further distinguished, or in other words, the subdomains are considered as "homogeneous". However, quite naturally, there has been the wish to retrieve, from Computed Tomographs, some more detailed, i.e. inhomogeneous, voxel-specific material properties. This aim has been followed perhaps the most pronouncedly, in the domain of bone imaging: By means of extended regression analyses, relations between X-ray attenuation and mass density of the matter found in respective voxels, on the one hand, and between mass density and Young's modulus, on the other, attenuation-density-elasticity relations have been frequently proposed and reported[46,47,48,49]. However, most of the relationships proposed are not very much in line with each other – and the debate on the "proper choice" of regression parameters seems somewhat indeterminable, as a direct

consequence of the rather vague physical foundation for the choice of attenuation-density-elasticity relations to be sought for.

This situation has provoked the emergence of an alternative view on the issue of proper evaluation of grey values stemming from CT images, with the present contribution marking an important "landmark". In more detail, the steps towards this present landmark have been the following: Instead of directly assuming unique attenuation-to-density relations, the first important step was to remember how, from the basic X-ray physics perspective, attenuation coefficient would be related to mass densities. In fact, it is well known that the attenuation coefficient related to a piece of material is equal to the sum of the material constituents' mass attenuation coefficients times their apparent mass densities (i.e. the constituents' masses over the overall volume of the considered piece of material)[15]. This relation could be directly transformed into a volume average rule for attenuation coeffients[16], which opened the way to a physics-based intervoxel analysis: Given a milimeter-sized voxel of a piece of cortical or trabecular bone and provided the attenuation coefficients of bone matrix and of vascular are known, voxel-specific attenuation coefficients can be converted in voxel-specific vascular porosities[16]. In the latter reference, attenuation coefficients were given in terms of Hounsfield numbers (which are attenuation coefficients related to that of water), so that the success of the method depended solely on a reasonably good estimate for the organ-specific, but space- and time-invariant Hounsfield number for the solid bone matrix (in the particularly considered case of a human mandible). Once the spatial porosity distribution throughout the organ was known, it could be further converted, by means of continuum micromechanics models validated for a large number of cortical and trabecular bone samples[50], to voxel-specific transversely isotropic fourth-order stiffness tensors. The situation becomes slightly more tricky if, rather than Houndfield numbers, only grey values which are linearly proportionally related to the X-ray attenuation coefficients are given (with two per se unknown proportionality constants not

disclosed by standard microCT equipment). One interesting feature of such attenuation-related grey values is that they still fulfill a volume average rule[7]. In cases where each micro-voxel just comprises a two-phase material, such as a glassy phase and some nanoporosity, the known grey values for voxels filled up by nanopores or by dense glass only, give again access to voxel-specific nanoporosities, which when combined with suitable micromechanics models for porous polycrystals[21], deliver voxel-specific elastic properties throughout porous bone tissue engineering scaffolds made out of bioglasses[7]. While the identification of the grey value of a pore-filled voxel follows quite unambigously from a histogram made from all voxels found within the considered 3D image, idenfication of the largest grey value as being actually of dense glass requires that such a completely glass- or ceramic-filled voxel would indeed occur in the investigated construct. In cases where this is not necessarily true the intravoxel analysis method has to be again refined: One way to do that consists of considering additional experiments conducted on the biomaterial scaffold, as it has been the case with hydroxyapatite bioceramics used as maxillofacial restoration tools[51]: Again encountering a two-phase ”pore-crystal“ material in each voxel, mathematical integration of the nanoporous space over the entire scaffold domain gives access to the overall mass density of the scaffold. Alternative, independent retrieval of the latter from direct weighing and volume tests of the scanned granule provides an additional equation for computing the nanoporosity found in the densest voxel. However, in all these contributions, the question remained on whether the proportionality constants between grey values and X-ray attenuation coefficients might be even directly accessible (without the need of additional – e.g. mass density – experiments), and the corresponding breakthrough was developed in detail in the present contribution: considering both the photon energy dependence of actual X-ray attenuation coefficients as publicly available in the NIST database, and the necessarily *unique* relation between grey values and X-ray attenuation coefficients, allowed indeed for direct determination of (i) the

proportionality constants, (ii) the used photon energy, and (iii) the X-ray attenuation distribution throughout nano- and microporous bioceramic scaffolds. Again, the latter information could be transformed into other, micromorphologically governed physical properties, such as elastic properties. In combination with similar endeavors concerning bone tissue[51], this opens the way to realistic mechanical modeling of bone-tissue composites as encountered in tissue engineering, and when extending the morphology-to-mechanics conversion step towards material strength[23,53] and viscoelasticity[54], to reliable computer-aided biomaterial design, at a level approaching that of classical civil or mechanical engineering. We regard this as an important complement to various activities in mechanics-based biomaterial research emerging recently on the international engineering science scene[55,56,57,58]. While a more detailled presentation of corresponding mechanics-related results, as currently under intensive investigation, is reserved for future publications, we re-iterate from the results of this paper that also the newly developed intravoxel porosity analysis in itself has revealed remarkable bioresorption and cytocompatibility features, which, to the best knoweldge of the authors, have never been described up the present precision so far: Namely, resorption of beta-TCP scaffolds occurs at the sub-micron level much more than at the milimeter level, and pre-osteoblastic cells do profilerate on the scaffolds' internal and external surfaces, as has been reported in earlier studies[59] – however, the life conditions in static cultures do not trigger them as to produce real mineralized bone matrix. Therefore, dynamic conditions such as in a bioreactor[60,61] may be needed – they are at the center of the current and future practical clinical side of the described research endeavors.

V. ACKNOWLEDGMENTS

The authors are grateful for financial support through the ERASMUS network, and through COST Action MP1005 NAMABIO, making the cooperation between Reykjavik University and the Vienna University of Technology (TU Wien) possible. Moreover, the Viennese

researchers gratefully acknowledge support from the European Research Council (ERC), in the course of project #257023, MICROBONE.

REFERENCES

1. S. T. Ho and D. W. Hutmacher: A comparison of micro CT with other techniques used in the characterization of scaffolds. *Biomaterials* **27**, 8 (2006).

2. C. Renghini, V. Komlev, F. Fiori, E. Verné, F. Baino, and C. Vitale-Brovarone: Micro-CT studies on a 3D bioactive glass-ceramic scaffolds for bone regeneration. *Acta Biomater.* **5**, 4 (2009).

3. O. Gauthier, R. Müller, D. von Stechow, B. Lamy, P. Weiss, J.-M. Bouler, E. Aguado, and G. Daculsi: In vivo bone regeneration with injectable calcium phosphate biomaterial: A three-dimensional micro-computed tomographic, biomechanical and SEM study. *Biomaterials* **26**, 27 (2005).

4. R. Cedola, A. Giuliani, A. Komlev, V. Lagomarsino,S. Mastrogiacomo, M. Peyrin, F Rustichelli, F. Cancedda: Bulk and interface investigations of scaffolds and tissue-engineered bones by X-ray microtomography and X-ray microdiffraction. *Biomaterials* **28**, 15 (2007).

5. A. C. Jones, C. H. Arns, A. P. Sheppard, D. W. Hutmacher, B. K. Milthorpe, and M. A. Knackstedt: Assessment of bone ingrowth into porous biomaterials using micro-CT. *Biomaterials* **28**, 15 (2007).

6. S.V.N. Jaecques, H. Van Oosterwyck, L. Muraru, T. Van Cleynenbreugel, E. De Smet, M. Wevers, I. Naert, and J. Vander Sloten: Individualised, micro CT-based finite element modelling as a tool for biomechanical analysis related to tissue engineering of bone. *Biomaterials* **25**, 9 (2004).

7. S. Scheiner, R. Sinibaldi, B. Pichler, V. Komlev, C. Renghini, C. Vitale-Brovarone, F. Rustichelli, C. Hellmich: Micromechanics of bone tissue-engineering scaffolds, based on resolution error-cleared computer tomography. *Biomaterials* **30**, 12 (2009).

8. S. Truscello, G. Kerckhofs, S. Van Bael, G. Pyka, J. Schrooten, and H. Van Oosterwyck: Predicition of permeability of regular scaffolds for skeletal tissue engineering: A combined computational and experimental study, *Acta Biomater.* **8**, 4 (2012).

9. M. R. Dias, P. R. Fernandes, J. M. Guedes, and S. J. Hollister: Permeability analysis of scaffolds for bone tissue engineering. *J. Biomech.* **45**, 6 (2012).

10. C. Sandino, S. Checa, P. J. Prendergast, and D. Lacroix: Simulation of angiogenesis and

cell differentiation in a CaP scaffold subjacted to compressive streins using a lattice modeling approach. *Biomaterials* **31**, 8 (2010).

11. C. Sandino and D. Lacroix: A dynamical study of the mechanical stimuli and tissue differentiation within a CaP scaffold based on micro-CT finite element models, *Biomech. Model. Mechan.* **10**, 4 (2011).

12. J. H. Hubbel, and S. M. Seltzer: Tables of X-ray mass attenuation coefficients and mass energy-absorption coefficients from 1 keV to 20 MeV for elements Z = 1 to 92 and 48 additional substances of dosimetric interest. *National Institute of Standards and Technologies* (2011).

13. S. M. Seltzer: Calculation of photon mass energy-transfer and mass energy-absorption coefficients. *Radiat. Res.* **136**, 2 (1993).

14. J. H. Hubbel: Photon mass attenuation and energy-absorption coefficients, *Int. J. Appl. Radiat. Is.* **33**, 11 (1982).

15. E. O. Crawley, W. D. Evans, and G. M. Owen: A theoretical analysis of the accuracy of single-energy CT bone measurements. *Phys. Med. Biol.* **33**, 10 (1988).

16. C. Hellmich, C. Kober, and B. Erdmann: Micromechanics-based conversion of CT data, *Ann. Biomed. Eng.* **36**, 1 (2008).

17. J. Radon: Über die Bestimmung von Funktionen durch ihre Integralwere längs gewisser Mannigfaltigkeiten. [On the determination of functions from their integrals along certain manifolds], *SBLeipzig* **29**, 69 (1917).

18. G. Hounsfield: A method of an apparatus for examination of a body by radiation such as X-ray or gamma-radiation, *Patent specification 1283915, The Patent Office* (1972).

19. Medical Imaging and Technology Alliance (division of the National Electrical Manufacturers Association): DICOM PS3.3 2013 - Information Object Definitions (2013).

20. R. Cobel and W. Kingley: Effect of porosity on physical properties of alumina. *J. A. Ceram. Soc.* **39**, 11 (1956).

21. A. Fritsch, C. Hellmich, and P. Young: Micromechanics-derived scaling relations for poroelasticity and strength of brittle porous polycrystals. *J. Appl. Mech.* **80**, 2 (2013).

22. A. Fritsch, L. Dormieux, and C. Hellmich: Porous polycrystals built up by uniformly and axisymmetrically oriented needles: homogenization of elastic properties. *C. R. Mec.* **334**, 3 (2006).

23. A, Fritsch, L. Dormieux, C. Hellmich, and J. Sanahuja: Mechanical behaviour of hydroxyapatite biomaterials: an experimentally validated micromechanical model for

elasticity and strength. *J Biomed. Mater. Res Part A* **88**, 1 (2009).

24. J. Sanahuja, L. Dormieux, S. Meille, C. Hellmich, and A. Fritsch: Micromechanical explanation of elasticity and strength of gypsum: from elongated anisotropic crystals to isotropic porous polycrystals. *J. Eng. Mech.* **136**, 2 (2010).

25. A. Fritsch, C. Hellmich, and L. Dormieux: The role of disc-type crystal shape for micromechanical predictions of elasticity and strength of hydroxyapatite biomaterials. *Philos. Trans. R. Soc.* **368**, 1917 (2010).

26. M. Ali and B. Singh: The effect of porosity on the properties of glass fibre-reinforced gypsum plaster. *J. Mater. Sci.* **10**, 11 (1975).

27. K. Phani: Young's modulus-porosity relation in gypsum systems. *Am. Ceram. Soc. Bull.* **65**, 12 (1986).

28. E. Tazawa: Effect of self stress on flexural strength of gypsum-polymer composites. *Adv. Cem. Based Mater* **7**, 1 (1998).

29. S. Meille: Etude du comportement mécanique du plâtre pris en relation avec sa microstructure [Study of the mechanical behaviour of gypsum with regard to its microstructure]. *Ph.D. thesis, INSA Lyon, Lyon, France (in French)* (2001).

30. M. Colak: Physical and mechanical properties of polymer-plaster composites. *Mater. Lett.* **60**, 16 (2006).

31. F. Carcium, C. Galassi, E. Roncari, A. Filippi, and G. Guidarelli: Electro-elastic properties of porous piezoelectric ceramics obtained by tape casting. *Ferroelectrics* **205** (1998).

32. W. Pabst, E. Gregorová, G. Tichá, and E. Týnová: Effective elastic properties of alumina-zirconia composite ceramics-part 4. tensile modulus of porous alumina and zirconia. *Ceramics-Silikáty* **48**, 4 (2004).

33. C. Reynaud, F. Thévenot, T. Chartier, and J.-L. Besson: Mechanical properties and mechanical behaviour of sic dense-porous laminates. *J. Eur. Ceram. Soc.* **25** (2005).

34. A. Díaz and S. Hampshire: Characterisation of porous silicon nitride materials produced with starch. *J. Eur. Ceram. Soc.* **24** (2004).

35. W. Pabst, E. Gregorová, and G. Tichá: Elasticity of porous ceramics--a critical study of modulusporosity relations. *J. Eur. Ceram. Soc.* **26** (2006).

36. L. Liang, P. Rulis, and W.Y. Ching: Mechanical properties, electronic structure and bonding of α- and β-tricalcium phosphates with surface characterization. *Acta Biomater.* **6** (2010).

37. M. Mastrogiacomo, V. S. Komlev, M. Hausard, F. Peyrin, F. Turquier, S. Casari, A. Cedola, F. Rustichelli, and R. Cancedda: Synchrotron radiation microtomography of bone engineered from bone marrow stromal cells. *Tissue Eng.* **10**, 11-12 (2004).

38. V.S. Komlev, F. Peyrin, M. Mastrogiacomo, A. Cedola, A. Papadimitropoulos, F. Rustichelli, and R. Cancedda: Kinetics of *in vivo* bone deposition by bone marrow stromal cells into porous calcium phosphate scaffolds: an x-ray computed microtomography study. *Tissue Eng.* **12**, 12 (2006).

39. M.C. von Doernberg , B. von Rechenberg, M. Bohner, S. Grünenfelder, G. Harry van Lenthe, R. Müller, B. Gasser, R. Mathys, G. Baroud, J. Auer: *In vivo* behavior of calcium phosphate scaffolds with four different pore sizes, *Biomaterials* **27**, 30 (2006).

40. R. Cedola, A. Guiliani, A. Komlev, V. Lagomarsino, S. Mastrogiacomo, M. Peyrin, F. Rustichelli, F. Cancedda: Bulk and interface investigations of scaffolds and tissue-engineered bones by X-ray microtomography and X-ray microdiffraction. *Biomaterials* **28** (2007).

41. M. Mastrogiacomo, A. Papadimitropoulos, A. Cedola, F. Peyrin, P. Giannoni, S.G. Pearce, M. Alini, C. Giannini, A. Guagliardi, and R. Cancedda.: Engineering of bone using bone marrow stromal cells and a silicon-stabilized tricalcium phosphate bioceramic: Evidence for a coupling between bone formation and scaffold resorption. *Biomaterials* **28**, 7 (2007).

42. A.C. Jones, C. H. Arns, A. P. Sheppard, D. W. Hutmacher, B. K. Milthorpe, and M. A. Knackstedt: Assessment of bone ingrowth into porous biomaterials using MICRO-CT. *Biomaterials* **28**, 15 (2007).

43. V. S. Komlev, M. Mastrogiacomo, R. C. Pereira, F. Peyrin, F. Rustichelli, and R. Cancedda.: Biodegradation of porous calcium phosphate scaffolds in an ectopic bone formation model studied by X-ray computed microtomography. *Europ. Cells and Mat.* **19** (2010).

44. S.K. Lan Levengood, S. J. Polak, M. J. Poellmann, D. J. Hoelzle, A. J. Maki, S. G. Clark, M. B. Wheeler, and A. J. Wagoner Johnson: The effect of BMP-2 on micro-and macroscale osteointegration of biphasic calcium phosphate scaffolds with multiscale porosity. *Acta Biomater* **6**, 8 (2010).

45. A. Giuliani, A. Manescu, M. Langer, F. Rustichelli, V. Desiderio, F. Paino, A. De Rosa, L. Laino, R. d'Aquino, V. Tirino, and G Papaccio: Three years after transplants in human mandibles, histological and in-line holotomography revealed that stem cells regenerated a compact rather than a spongy bone: biological and clinical implications, *Stem Cells Transl. Med.* **2** (2013).

46. J.Y. Rho, M.C. Hobatho, and R.B. Ashman: Relations of mechanical properties to density and CT numbers in human bone. *Med Eng Phys* **17**, 5 (1995).

47. B. Couteau, M.C. Hobatho, R. Darmana, J.C. Brignola, and J.Y. Arlaud: Finite element modelling of the vibrational behaviour of the human femur using CT-based individualized geometrical and material properties. *J Biomech* **31**, 4 (1998).

48. J.H. Keyak and Y. Falkinstein: Comparison of in situ and in vitro CT scan-based finite element model predictions of proximal femoral fracture load. *Med Eng Phys* **25**, 9 (2003).

49. A. Cong, O.D. Buijs, and D. Dragomir-Daescu: In situ parameter identification of optimal density-elastic modulus relationships in subject-specific finite element models of the proximal femur. *Med Eng Phys* **33**, 2 (2011).

50. C. Hellmich, F.-J., Ulm, and L. Dormieux: Can the diverse elastic properties of trabecular and cortical bone be attributed to only a few tissue-independent phase properties and their interactions? Arguments from a multiscale approach, *Biomech Model Mechanobiol* **2**, 4 (2004).

51. A. Dejaco, V.S. Komlev, J. Jaroszewicz, W. Swieszkowski, and C. Hellmich: Micro CT-based multiscale elasticity of double-porous (pre-cracked) hydroxyapatite granules for regenerative medicine. *J Biomech* **45**, 6 (2012).

52. R. Blanchard, A. Dejaco, E. Bongaers, and C. Hellmich: Intravoxel bone micromechanics for microCT-based finite element simulations. *J Biomech* **46**, 15 (2013).

53. A. Fritsch, C. Hellmich, L. Dormieux: Ductile sliding between mineral crystals followed by rupture of collagen crosslinks: Experimentally supported micromechanical explanation of bone strength. *J. Theor. Biol.* **260**, 2 (2009).

54. L. Eberhardsteiner, C. Hellmich, and S. Scheiner: Layered water in crystal interfaces as source for bone viscoelasticity: Arguments from a multiscale approach. *Comput. Method. Biomec.* **17**, 1 (2014).

55. R. Khanna, D. Katti, and K.Katti: Nanomechanics of surface modified nanohydroxyapatite particulates used in biomaterials. *J. Eng. Mech.* **135**, 5 (2009).

56. R. Khanna, D. Katti and K. Katti: AFM and nanoindentation studies of bone nodules on chitosan-polygalacturonic acid-hydroxyapatite nanocomposites. *CMES* **87**, 6 (2012).

57. S. Huang, Z. Li, Z. Chen, Q. Chen and N. Pugno: Study on the elastic-plastic behaviour of a porous hierarchical bioscaffold used for bone regeneration. *Mater. Lett.* **112** (2013).

58. Q. Chen, F. Baino, S. Spriano, N.M. Pugno, C. Vitale-Brovarone: Modelling of the strength-porosity relationship in glass-ceramic foam scaffolds for bone repair

J. Europ. Cer. Soc. (2014), Article in Press.

59. M. Azami, A. Samadikuchaksaraei, and S.A. Poursamar: Synthesis and characterization of a laminated hydroxyapatite/gelatin nanocomposite scaffold with controlled pore structure for bone tissue engineering. *Int J Artif Organs* **33**, 2 (2010).

60. Q. Lv, M. Deng, B. Ulery, L. M.Phil and C. Laurencin: Nano-ceramic composite scaffolds for bioreactor-based bone engineering. *Clin. Orthop. Re. Res.* **471** (2013).

61. Q. Lv, L. Nair and C. Laurencin: Fabrication, characterization, and in vitro evaluation of poly(lactic acid glycolic acid)/nano-hydroxyapatite composite microsphere-based scaffolds for bone tissue engineering in rotating bioreactors. *J. Biomed. Mater. Res.* **91A**, 3 (2008).

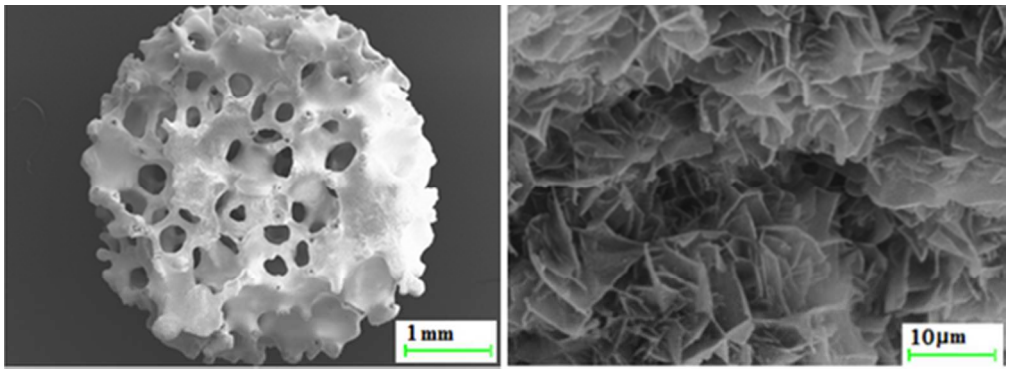

Double porous structure of investigated ceramic biomaterial, as revealed by means of Scanning Electron Microscopy: (a) "macropores" of several hundreds of micrometers size, and (b) "nanopores" at the sub-micrometer scale
47x17mm (300 x 300 DPI)

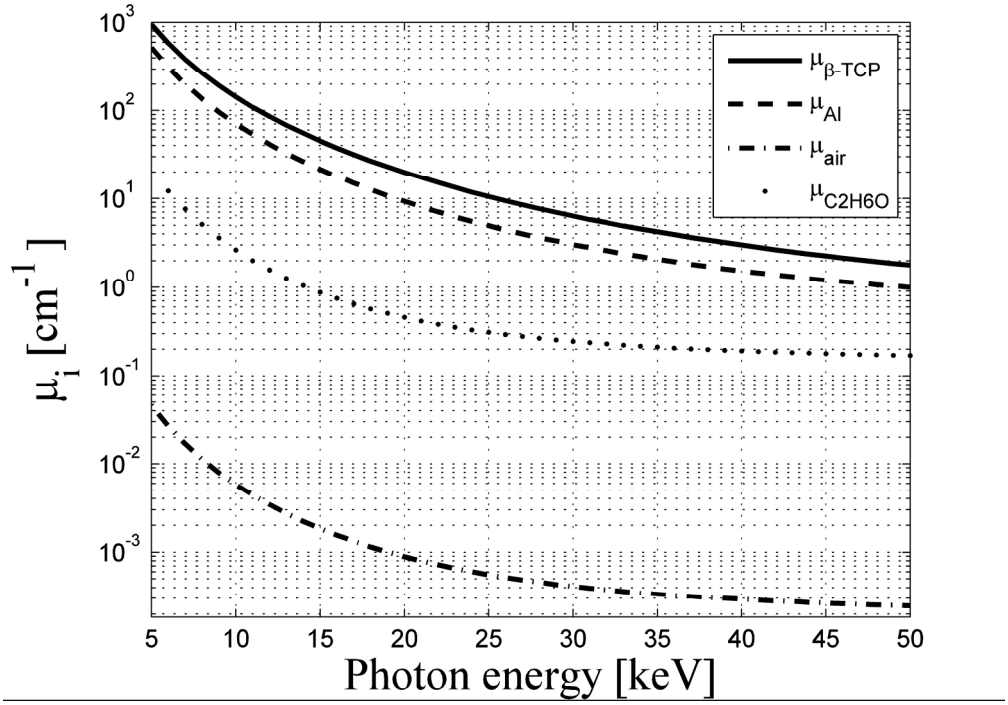

X-ray attenuation coefficients of pure β-TCP, of aluminum, of ethanol, and of air, as functions of the photon energy ε
102x74mm (600 x 600 DPI)

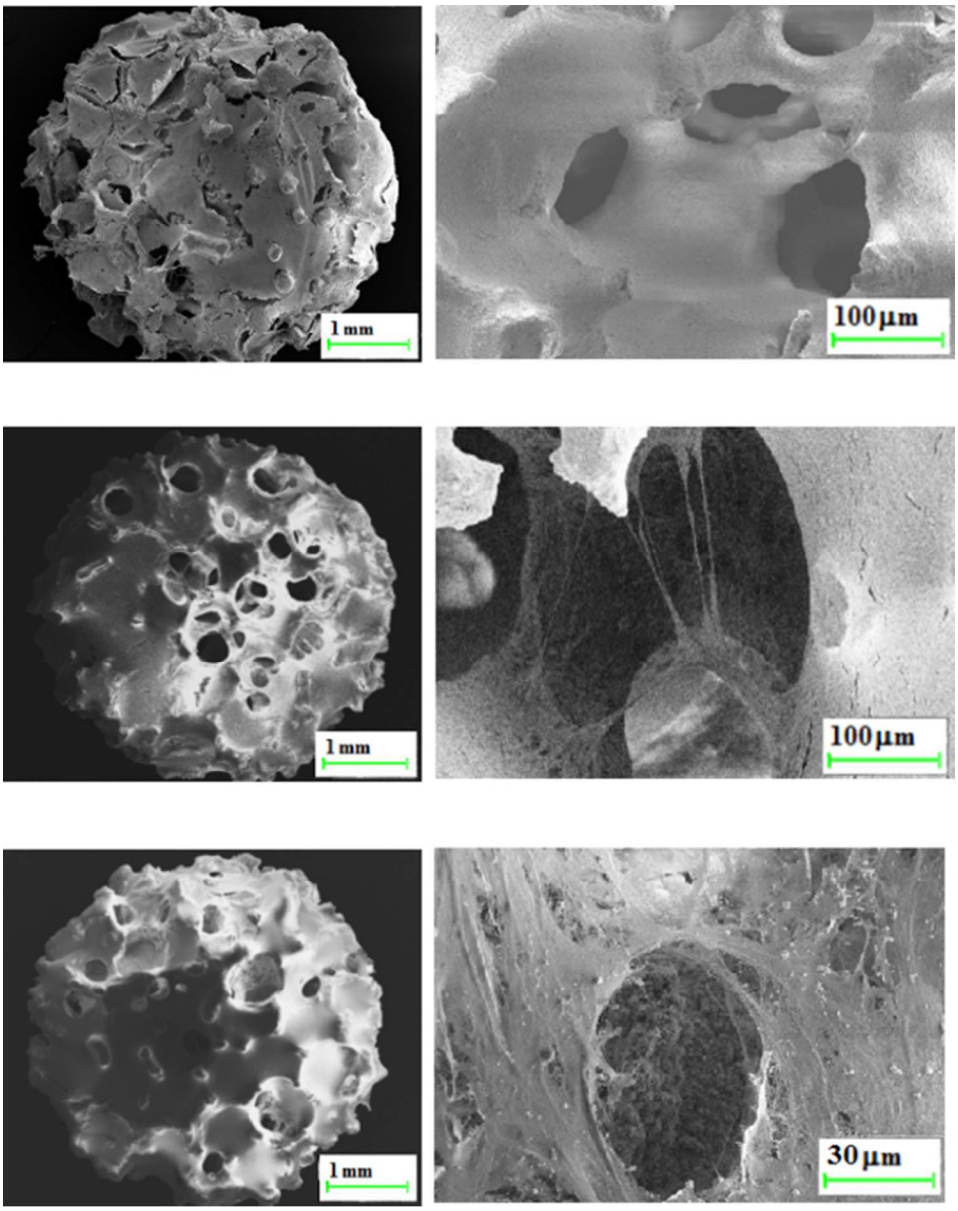

Cell proliferation on ceramic scaffolds as revealed by SEM, at low magnification showing entire scaffolds with approximately 5 mm diameter (a,c,d), and at high magnification zooming into one of the "macropore" cavities (b,d,f): comparison of cell covers after 3 weeks of cultivation (a,b), with the situations after 6 weeks (c,d), and after 8 weeks (e,f)
56x70mm (300 x 300 DPI)

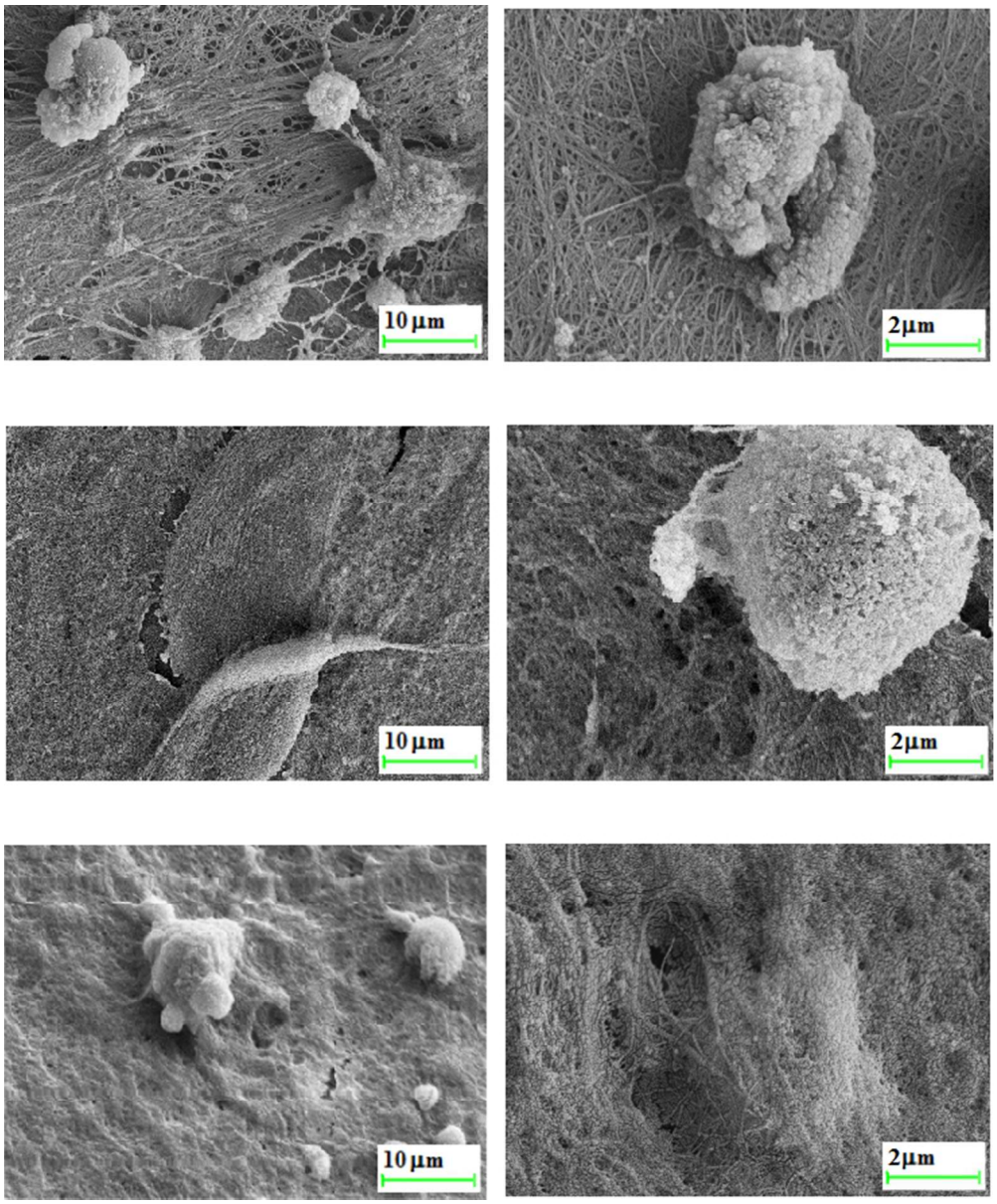

SEM-based close up of immediate vicinity of a cell nodule: after 3 weeks (a,b), after 6 weeks (c,d), and after 8 weeks (e,f)
194x234mm (96 x 96 DPI)

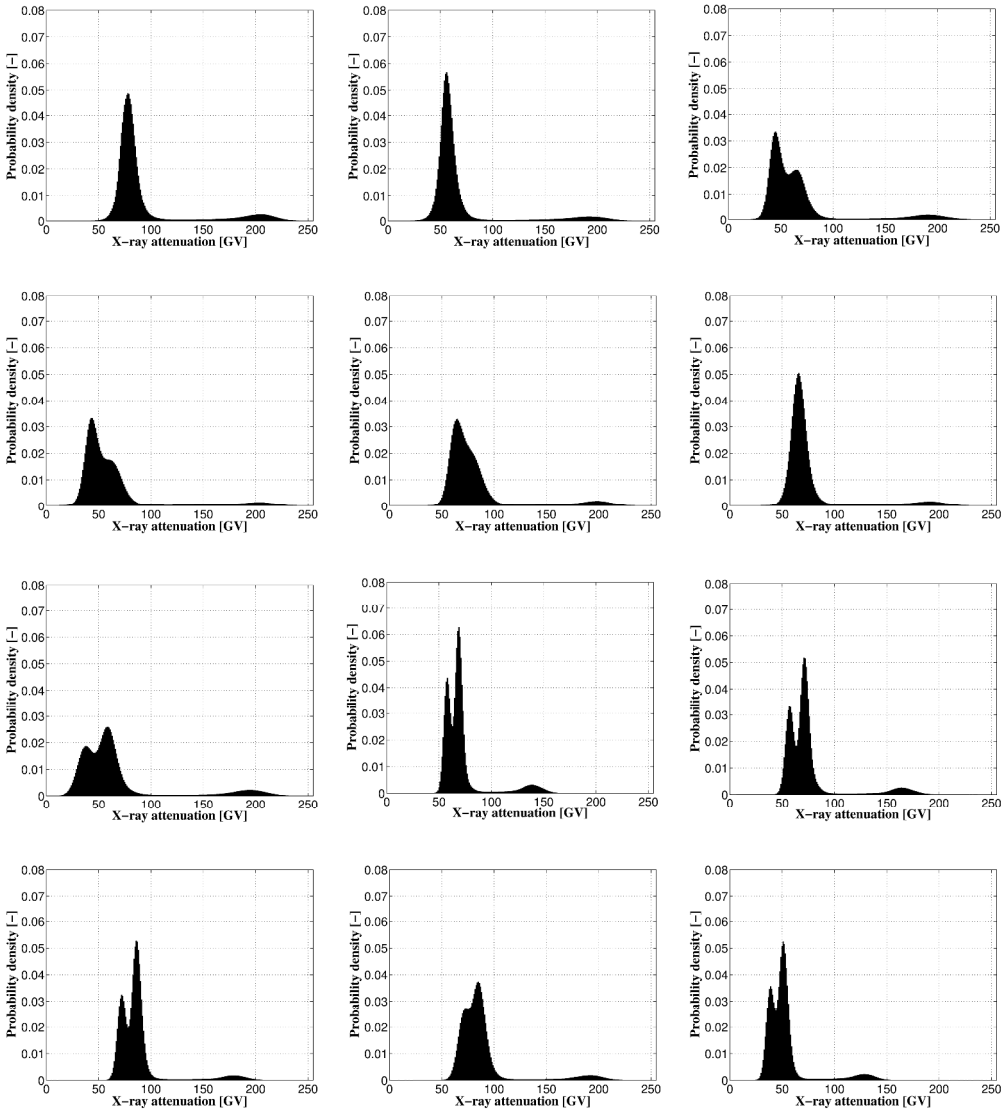

Probability density function of attenuation-related grey values of six CT-imaged β-TCP scaffolds, before cell culturing (a-f): (a) sample I, (b) sample II, (c) sample III, (d) sample IV, (e) sample V, (f) sample VI; and after cell culturing (g-l): (g) sample I after 3 weeks of culturing, (h) sample II after 3 weeks of culturing (i) sample III after 6 weeks of culturing, (j) sample IV after 6 weeks of culturing, (k) sample V after 8 weeks of culturing, (l) sample VI after 8 weeks of culturing
590x654mm (250 x 250 DPI)

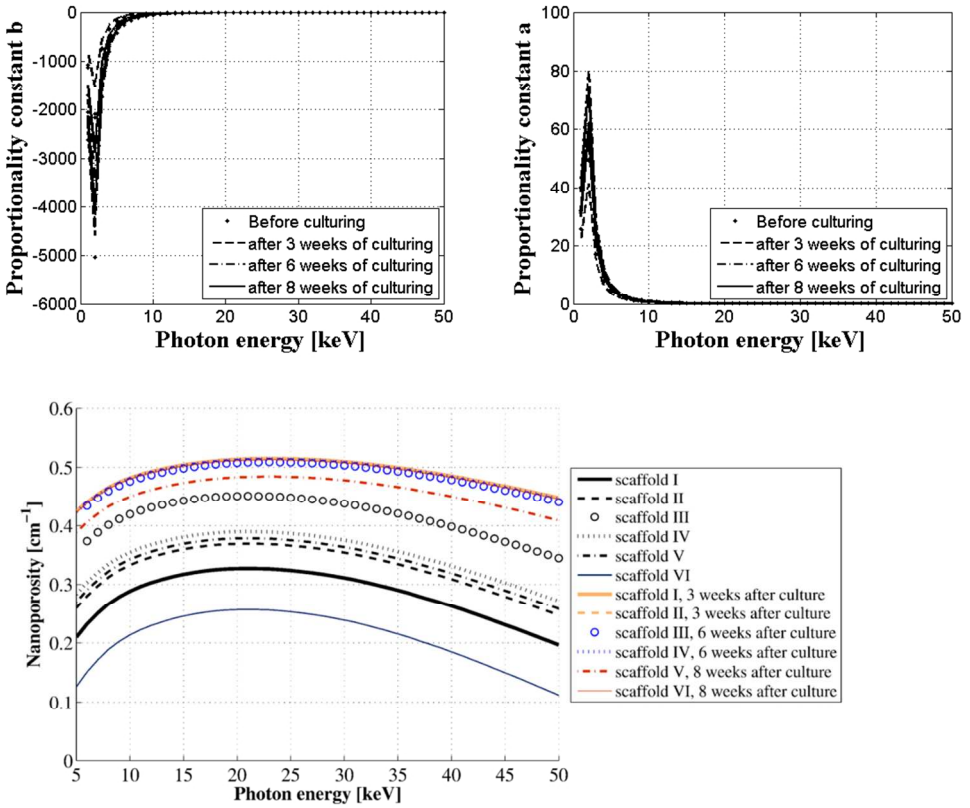

Proportionality constants relating grey values to attenuation coefficients, as functions of the photon energy Ɛ; (c) scaffold-specific ϕpeak - Ɛ - relations, used for identification of scanner-specific employed photon energy and actual value of most frequently occurring nanoporosity
115x94mm (250 x 250 DPI)

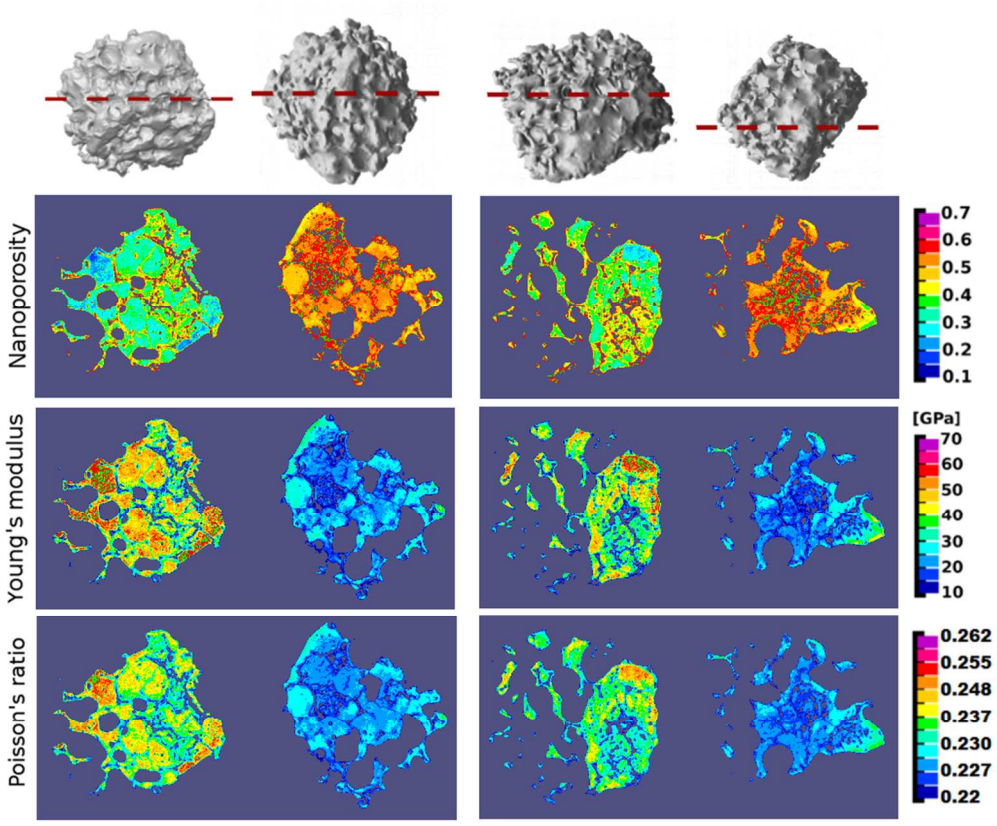

Spatial distributions of voxel-specific nanoporosity and elastic properties, i.e. Young's modulus and Poisson's ratio, over chosen cross sections through: sample I before culturing (a), sample I after 3 weeks of culturing (b), sample II before culturing (c), sample II after 3 weeks of culturing (d)
363x299mm (72 x 72 DPI)

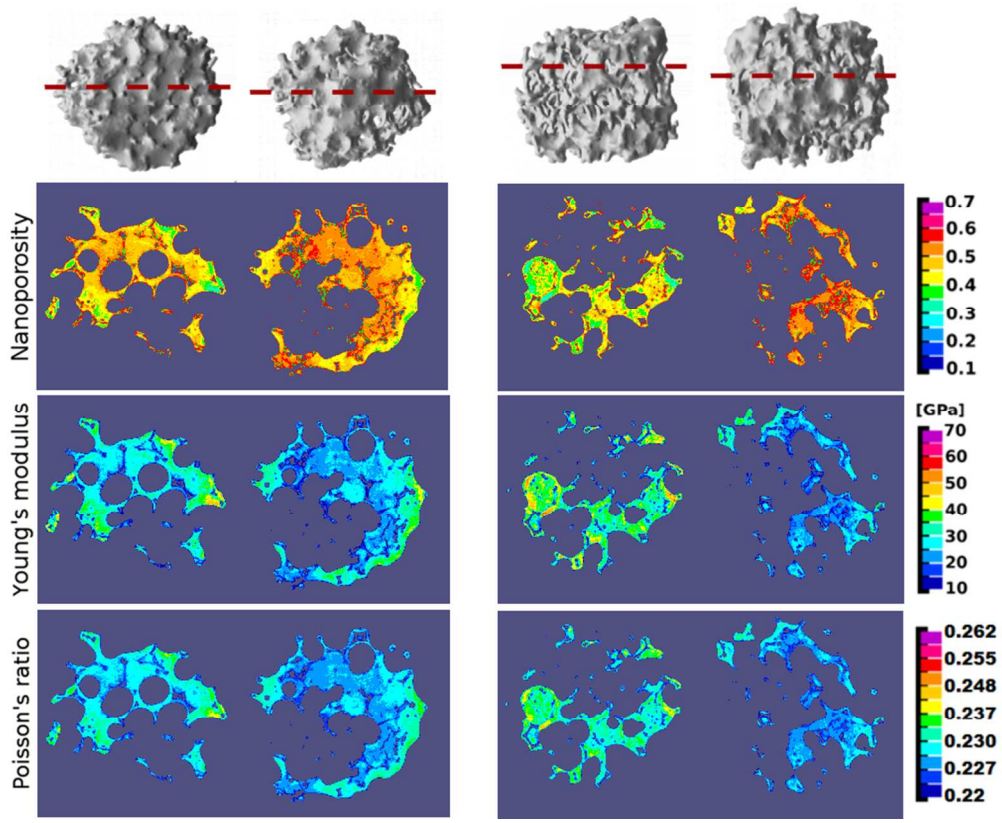

Spatial distributions of voxel-specific nanoporosity and elastic properties, i.e. Young's modulus and Poisson's ratio, over chosen cross sections through: sample III before culturing (a), sample III after 6 weeks of culturing (b), sample VI before culturing (c), sample VI after 6 weeks of culturing (d)
356x290mm (72 x 72 DPI)

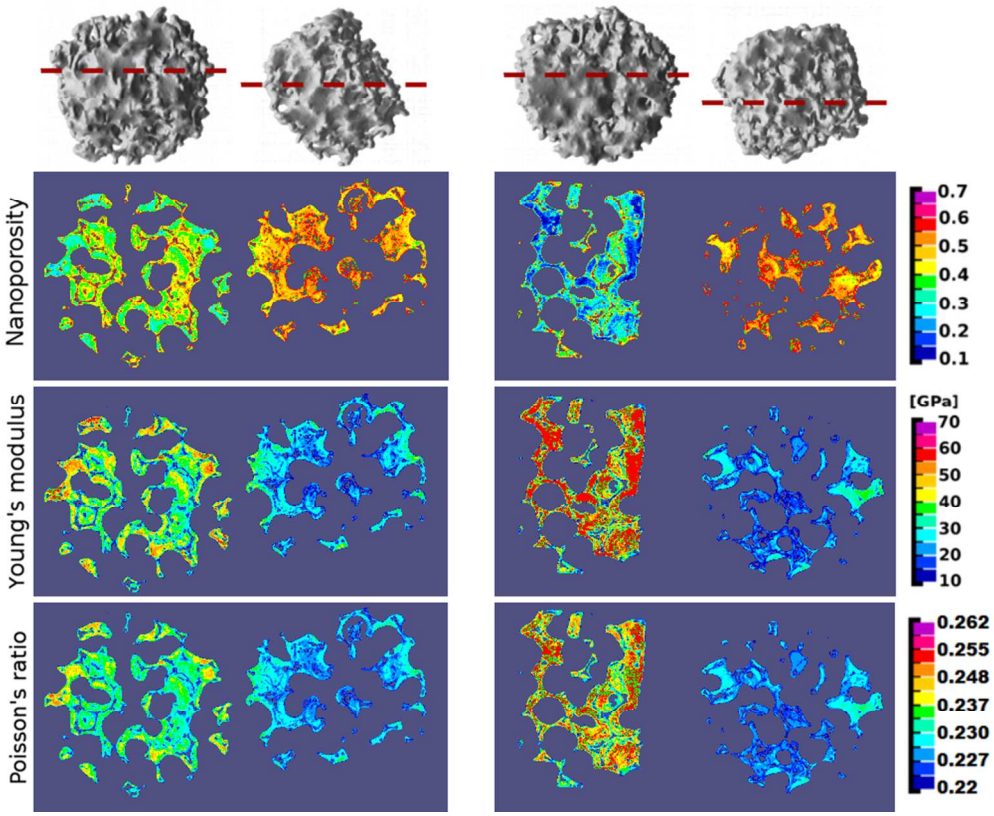

Spatial distributions of voxel-specific nanoporosity and elastic properties, i.e. Young's modulus and Poisson's ratio, over chosen cross sections through: sample V before culturing (a), sample V after 8 weeks of culturing (b), sample VI before culturing (c), sample VI after 8 weeks of culturing (d)
354x288mm (72 x 72 DPI)

3.2 Preparation and cell culture protocol

For this experiment mouse pre-osteoblastic MC3T3-E1 cells, derived from mouse calvariae were used. This experiment were carried out at REModeL Laboratory, The Blood Bank, Landspitali University Hospital, Iceland. All preparation and work were done in a tissue culture hood. The following equipments were used:

- Tissue culture hood
- Inverted Microscope
- Centrifuge
- Refrigerator
- Freezer
- Vortexer
- Wipes
- Water distiller
- Alcohol, 70 % ethanol
- Pipets
- Flasks
- Cell culture tubes
- waste container

3.2.1 Culturing Protocol

Overview of the major steps in cell handling are listed below:

- Cell expansion
- Splitting cells
- Scaffold Preparation
- Cell Differentiation and Cultivation
- Fixation

Cell Expansion
The MC3T3-E1 mouse cells were expanded in 75 cm^2 flask, 5000 cells/cm^2 with 22.5 ml of expansion medium α-MEM containing penicillin/streptomycin and 10 % FBS. The flask were incubated for 7 days with change of medium every second day. After the expansion, the cells has been multiplied and they cover the intire bottom of the flask. In the splitting procedure, the expansion medium is poured off the cells, the cell layer is washed once with PBS. Tripsin is added on the cell layer and it is incubated for 3 to 5 min. The removal of Trypsin after 5 min is crucial for cells proper functionality. An equal amount of culturing medium as Trypsin is added deactivating the Trypsin. The cell suspension is centrifuged for 5 min and 1750 rpm and the medium is poured off. The cells are re-suspended with cell culture medium, kept in a 75 cm^2 Flask, until the scaffolds preparation.

Scaffold Preparation
For the *in vitro* cell culturing, 10, 3D β-TCP scaffolds were used, see Table 4.

Scaffolds Characteristics	
Material	β tricalcium phosphate
Dimension	5 mm in diameter, 3 mm in height
Volume	0.058 cm^3
Average pore size	200-400 μm
Structure	similar to cancellous bone

Table 1: Characteristics of the resorbing, ceramic, biomaterial scaffold used in this experiment

The porous, 3D scaffolds are very fragile so it is crucial to handle them carefully. A solution containing PBS and Fibronectin is prepared to improve cell attachment on the scaffolds. The scaffolds are placed inside a 24-well plate separately see Figure 1. The PBS and Fibronection mixed solution is poured on the scaffolds and they are incubated for 1 hour.

Figure 11

In the mean while the culturing medium for differentiation is prepared. The medium is mixed with α-MEM, 10 % FBS and PBS. After 1 hour of incubation the solution containing Fibronectin is removed from the scaffolds and medium is added on them and the entire 24 well plate is shook carefully, left on for 20 min and removed. Only 7 scaffolds will be seeded with cells, the other once are left empty for control. The chosen scaffolds for cell seeding are covered with 1 ml albumin for improving cell attachment and incubated for 30 min. Cells with density of 200.000 cells/150μl/scaffold are seeded and incubated for 1 hour. Next 850 μl of expansion medium is added carefully and not directly to the scaffolds in order to not wash the freshly attached cells away. For sufficient attachment of cells, the expansion medium is incubated for 1 or 2 days. The expansion medium was replaced with specific differentiation medium. The medium consisting of α-MEM mixed with Ascorbic Acid (Ascorbic Acid γ-irradiated, Sigma), FBS, and β-glycerophosphate. The cell culturing experiment was carried out in an incubator at 37 centigrades in a humidified atmosphere containing 95 % air and 5 % CO_2.

Fixation
In the 24-well plate the first row was fixed and microCT scanned after 3 weeks of cell culture, the second row of scaffolds were fixed and scanned after 6 weeks of cell culture, and the last row containing 4 scaffolds were fixed in the end of 8 weeks cell culturing before scanning. The fixation protocol is listed below:

- Wash 3x with PBS
- Fix scaffolds in formaline for 15 min
- Prepare ethanol dehydration series:

  5 %

  12.5 %

  25 %

  50 %

  75 %

  96 %
- Each percentage of ethanol is kept on for 10 min

  100 μl/well
- Prepare a 15 ml falcon with sample name and 96 % ethanol

  Transfer scaffold gently into the falcon tube

  Close well

  Store until taken for microCT scanning and then crytical point drying

3.3 Matlab instructions

The data sets gained from the microCT equipment are analysed with MATLAB programming. A main script is assembled and the other additional scripts are controlled from there. There is only one separate script which back calculates the photon energy used by the microCT equipment which is described later. An overview of the main script is presented here below:

- Informations are given for folders, scaffold number, images counts, and the directory
- Mass density is given for β-TCP and ethanol (g/cm^3)
- The mean grey value (peak) of the data's are given for air, ethanol, aluminium and β-TCP for every sample from the histogram of the data
- GV_E21 are the GV_max when the photon energy is 21 keV calculated with a formula (based on the linear relation between grey values and attenuation coefficients), (see maiScript_Efunction_Agnes.m)
- The maximum grey values GV_max are gained from the Gaussian distribution which will be used for the data processing for GV_max
- The photon energy is given, 21 keV since the energy was back calculated in script mainScript_Efunction_Agnes.m.
- First the dicom data sets are imported with a script import_images
- Attenuation coefficients are gained from script fun_NIST_A
- The linearity constants are calculated for each data set (formula for a and b)
- The nanoporosities are converted from the attenuation coefficients in script Nanopores
- Images are cleaned from GV of air in script image_cleaning resulting only GV of the 3D scaffold visible
- Nanoporosity is taken only of the scaffolds material (Threshold to GV_max) called nanop_clean
- Homogenization is done in script hom_scaffold_clean
- Engineering table is created of mechanical properties of the 3D scaffold for each data set
- Reduction of image size and txt files written in script generate_grey_el
- Color maps are generated of the 3D scaffold presenting the mechanical properties in script generate_color_rhoec
- Color scale are stored in script generate_color_image_cryst_rhoec which is used by the script generate_color_rhoec

The main script and all the MATLAB scripts which are included within main script are listed here below:

```
%                                                                       %
% main.m                                                               %
%                                                                       %
% Created by:         Agnes Czenek                                     %
% E-Mail:             agnesc08@ru.is                                   %
% Based on code by:   Romane Blanchard and Alexander Dejaco            %
% Note:               The linear relation between grey values          %
%                     and attenuation coefficients are used to         %
%                     convert the voxel-specific grey values to        %
%                     voxel-specific attenuation coefficients          %
%                     in microCT data sets. The corresponding          %
%                     voxel-specific nanoporosities are gained         %
%                     for estimation of elastic properties             %
%                     determined from micromechanical consideration    %
%%%%%%%%%%%%%%%%%%%%%%%%%%%%%%%%%%%%%%%%%%%%%%%%%%%%%%%%%%%%%%%%%%%%%%%

clear all
close all
clc

% PARAMETERS

folder='8weeks_8bit'
scaffold_number=17 %used for calculation a and b; 1-20
scaffold='scaffold7_8w'
images_count=1015
dir=['/ct_images/',folder,'/',scaffold];

rho_bTCP = 3.07;    % g/cm3 mass density of CaP scaffold
rho_ETH = 0.789;    % g/cm3 mass density of ethanol

%   GV = [1.e;2e;3e;  4e; 5e; 6e; 7e; 8e; 9e; 10e;1.3w;2.3w;3.3w;4.6w;5.6w;6.6w;7.8w;8.8w;9.8w;
10.8w]
%         1   2   3   4   5   6   7   8   9   10  11   12   13   14   15   16
% [0:255] !!
GV_AIR_vec = [77; 55; 70; 44; 42; 59; 64; 65; 39; 36; 37;  57;  80;  56;  71;  44; 71; 39; 55; 62];
GV_ETH_vec = [77; 55; 70; 65; 60; 59; 76; 65; 62; 62; 58;  68;  95;  70;  85;  63; 84; 50; 68; 62];
GV_AL_vec =  [165;157;159;168;165;167;163;144;180;184;184;133; 185; 155; 171; 179; 177;122;169; 105];
GV_SC_vec =  [204;193;188;190;203;195;196;191;185;189;194;138; 194; 163; 178; 188; 191;128;180; 198];

%Maximum value of GV for Gaussian distrib.

%   GV = [1.e;2e;3e;  4e; 5e; 6e; 7e; 8e; 9e; 10e;1.3w;2.3w;3.3w;4.6w;5.6w;6.6w;7.8w;8.8w;9.8w;
10.8w]
%         1   2   3   4   5   6   7   8   9   10  11   12   13   14   15 16
GV_E21 = [266;274;0;310;306;  0; 276;234; 0;   0;352; 220;   0;  268;286;   0; 298;217;0;0]
GV_max = [245;240;0;239;246;  0; 240;235; 0;   0;240; 167;   0;  198;212;   0; 227;157;0;0]

GV_AIR= GV_AIR_vec(scaffold_number);
GV_ETH= GV_ETH_vec(scaffold_number);
GV_AL= GV_AL_vec(scaffold_number);
GV_SC= GV_SC_vec(scaffold_number);

photon_energy=21;

import_images
%save(['raw_volume/',folder,'_',scaffold,'_','raw_volume.mat'])

%%
%load(['raw_volume/',folder,'_',scaffold,'_','raw_volume.mat'])
```

```
fun_NIST_A

b=(mu_AIR_theoretical*GV_AL-mu_AL_theoretical*GV_AIR)/(GV_AL-GV_AIR)
a=(mu_AIR_theoretical-mu_AL_theoretical)/(GV_AIR-GV_AL)


[nanop,threshold]=nanopores(a, b, GV_ETH, GV_AL, GV_E21, GV_max, hist_all, mu_ETH_theoretical, mu_AIR_theoretical


%% Raw data, nanopores in GV_scaffold

image_cleaning


GV_vector=(threshold:GV_max(scaffold_number));
nanop_clean=nanop(GV_vector);



%% Homogenization of cleaned images from threshold to max values (of scaffold, [no air and ethanol])
%[E3,nu31,G12]=hom_scaffold_clean(nanop_clean);
hom_func
%make_histograms

%% Writes data tables
% datatable=[GV_vector' nanop_clean' E3' nu31' G12'];
% fid=fopen(['engineering_table/engineering_table_',folder,scaffold,'.txt'],'w');
% %fprintf(fid,' GV    porosity     E3       nu31        G12\r\n');
% fprintf(fid, '%3.0f  %2.4f  %3.4f  %3.4f  %3.4f  \r\n',datatable');
% fclose(fid);

%% Write data tables
datatable=[GV_vector' nanop_clean' E_hom' nu_hom'];
fid=fopen(['engineering_table_',folder,scaffold,'.txt'],'w');
%fprintf(fid,' GV    porosity     Ehom      nuhom   \r\n');
fprintf(fid, '%3.0f  %2.4f  %3.4f  %3.4f  \r\n',datatable');
fclose(fid);
%%

% Reduction of image size by grouping of voxels + Generation of txt files
% with element number and porosity/Young's modulus/Poisson's ratio
 generate_grey_el
%
%% Generation of color maps
 generate_color_rhoec
```

```
slice=imread([dir,'/raw/',scaffold,'_0000.tif']);
%slice=imread([dir,'/raw/',scaffold,'_0000.tif']);

build_dimx=size(slice,1);
build_dimy=size(slice,2);
build_dimz=images_count;
voxels=build_dimx*build_dimy;

volumes=zeros(build_dimx,build_dimy,images_count,'uint8');
hist_all=zeros(1,256); %empty variable for matlab to be quicker (otherwise it has to add every line in every loop

for i=1:images_count
    if i<11
        slice = imread([dir,'/raw/',scaffold,'_000',num2str(i-1),'.tif']);
    elseif i>10 && i<101
        slice = imread([dir,'/raw/',scaffold,'_00',num2str(i-1),'.tif']);
    elseif i>100 && i<1001
        slice = imread([dir,'/raw/',scaffold,'_0',num2str(i-1),'.tif']);
    else
        slice = imread([dir,'/raw/',scaffold,'_',num2str(i-1),'.tif']);
    end
    volumes(:,:,i)=uint8(slice);
    disp(['imported ',num2str(i),'/',num2str(images_count)]);

    slice2 = double(slice); % convert to double
    slice_vec = reshape(slice2,voxels,1);  % make vector
    n = hist(slice_vec, 0:255);  % n...frequency count
    hist_all = hist_all + n;
end
```

```
% photon energz in keV
% from NIST database
% column 1 = photon energy [MeV]
% column 2 = mass attenuation coefficient
% [cm2/g]
close all
%

%MeV
 NIST_AL = ...
    [
    1.000E-03 1.185E+03
2.000E-03 2.263E+03
3.000E-03 7.881E+02
4.000E-03 3.605E+02
5.000E-03 1.934E+02
6.000E-03 1.153E+02
7.000E-03 7.408E+01
8.000E-03 5.032E+01
9.000E-03 3.569E+01
1.000E-02 2.621E+01
1.100E-02 1.981E+01
1.200E-02 1.534E+01
1.300E-02 1.212E+01
1.400E-02 9.744E+00
1.500E-02 7.955E+00
1.600E-02 6.583E+00
1.700E-02 5.513E+00
1.800E-02 4.667E+00
1.900E-02 3.990E+00
2.000E-02 3.442E+00
2.100E-02 2.993E+00
2.200E-02 2.623E+00
2.300E-02 2.314E+00
2.400E-02 2.055E+00
2.500E-02 1.836E+00
2.600E-02 1.649E+00
2.700E-02 1.489E+00
2.800E-02 1.351E+00
2.900E-02 1.232E+00
3.000E-02 1.128E+00
3.100E-02 1.037E+00
3.200E-02 9.576E-01
3.300E-02 8.873E-01
3.400E-02 8.250E-01
3.500E-02 7.696E-01
3.600E-02 7.202E-01
3.700E-02 6.760E-01
3.800E-02 6.364E-01
3.900E-02 6.007E-01
4.000E-02 5.684E-01
4.100E-02 5.392E-01
4.200E-02 5.128E-01
4.300E-02 4.886E-01
4.400E-02 4.667E-01
4.500E-02 4.466E-01
4.600E-02 4.281E-01
4.700E-02 4.112E-01
4.800E-02 3.957E-01
4.900E-02 3.814E-01
5.000E-02 3.681E-01
5.100E-02 3.559E-01
5.200E-02 3.446E-01
5.300E-02 3.340E-01
5.400E-02 3.242E-01
```

```
5.500E-02 3.151E-01
5.600E-02 3.066E-01
5.700E-02 2.987E-01
5.800E-02 2.913E-01
5.900E-02 2.843E-01
6.000E-02 2.778E-01
6.100E-02 2.717E-01
6.200E-02 2.659E-01
6.300E-02 2.605E-01
6.400E-02 2.554E-01
6.500E-02 2.506E-01
6.600E-02 2.460E-01
6.700E-02 2.417E-01
6.800E-02 2.376E-01
6.900E-02 2.338E-01
7.000E-02 2.301E-01
7.100E-02 2.266E-01
7.200E-02 2.233E-01
7.300E-02 2.202E-01
7.400E-02 2.172E-01
7.500E-02 2.143E-01
7.600E-02 2.116E-01
7.700E-02 2.089E-01
7.800E-02 2.064E-01
7.900E-02 2.041E-01
8.000E-02 2.018E-01
8.100E-02 1.996E-01
8.200E-02 1.975E-01
8.300E-02 1.955E-01
8.400E-02 1.935E-01
8.500E-02 1.917E-01
8.600E-02 1.899E-01
8.700E-02 1.881E-01
8.800E-02 1.865E-01
8.900E-02 1.849E-01
9.000E-02 1.833E-01
9.100E-02 1.818E-01
9.200E-02 1.804E-01
9.300E-02 1.790E-01
9.400E-02 1.777E-01
9.500E-02 1.764E-01
9.600E-02 1.751E-01
9.700E-02 1.739E-01
9.800E-02 1.727E-01
9.900E-02 1.715E-01
1.000E-01 1.704E-01
];

% % Ethanol  C2H6O
NIST_ETH = ...
    [1.000E-03 2.748E+03
2.000E-03 3.993E+02
3.000E-03 1.226E+02
4.000E-03 5.211E+01
5.000E-03 2.666E+01
6.000E-03 1.538E+01
7.000E-03 9.664E+00
8.000E-03 6.477E+00
9.000E-03 4.566E+00
1.000E-02 3.355E+00
1.100E-02 2.552E+00
1.200E-02 2.000E+00
1.300E-02 1.607E+00
1.400E-02 1.321E+00
1.500E-02 1.108E+00
```

1.600E−02 9.458E−01
1.700E−02 8.203E−01
1.800E−02 7.216E−01
1.900E−02 6.430E−01
2.000E−02 5.795E−01
2.100E−02 5.276E−01
2.200E−02 4.849E−01
2.300E−02 4.493E−01
2.400E−02 4.194E−01
2.500E−02 3.940E−01
2.600E−02 3.724E−01
2.700E−02 3.539E−01
2.800E−02 3.378E−01
2.900E−02 3.239E−01
3.000E−02 3.117E−01
3.100E−02 3.009E−01
3.200E−02 2.914E−01
3.300E−02 2.830E−01
3.400E−02 2.755E−01
3.500E−02 2.687E−01
3.600E−02 2.626E−01
3.700E−02 2.571E−01
3.800E−02 2.522E−01
3.900E−02 2.476E−01
4.000E−02 2.434E−01
4.100E−02 2.396E−01
4.200E−02 2.361E−01
4.300E−02 2.329E−01
4.400E−02 2.299E−01
4.500E−02 2.271E−01
4.600E−02 2.245E−01
4.700E−02 2.221E−01
4.800E−02 2.198E−01
4.900E−02 2.177E−01
5.000E−02 2.157E−01
5.100E−02 2.138E−01
5.200E−02 2.120E−01
5.300E−02 2.103E−01
5.400E−02 2.087E−01
5.500E−02 2.071E−01
5.600E−02 2.057E−01
5.700E−02 2.043E−01
5.800E−02 2.030E−01
5.900E−02 2.017E−01
6.000E−02 2.005E−01
6.100E−02 1.993E−01
6.200E−02 1.982E−01
6.300E−02 1.971E−01
6.400E−02 1.960E−01
6.500E−02 1.950E−01
6.600E−02 1.940E−01
6.700E−02 1.931E−01
6.800E−02 1.921E−01
6.900E−02 1.913E−01
7.000E−02 1.904E−01
7.100E−02 1.895E−01
7.200E−02 1.887E−01
7.300E−02 1.879E−01
7.400E−02 1.871E−01
7.500E−02 1.864E−01
7.600E−02 1.856E−01
7.700E−02 1.849E−01
7.800E−02 1.842E−01
7.900E−02 1.835E−01
8.000E−02 1.828E−01

```
8.100E−02 1.822E−01
8.200E−02 1.815E−01
8.300E−02 1.809E−01
8.400E−02 1.802E−01
8.500E−02 1.796E−01
8.600E−02 1.790E−01
8.700E−02 1.784E−01
8.800E−02 1.778E−01
8.900E−02 1.772E−01
9.000E−02 1.767E−01
9.100E−02 1.761E−01
9.200E−02 1.756E−01
9.300E−02 1.750E−01
9.400E−02 1.745E−01
9.500E−02 1.740E−01
9.600E−02 1.735E−01
9.700E−02 1.729E−01
9.800E−02 1.724E−01
9.900E−02 1.719E−01
1.000E−01 1.714E−01];


% % Tricalcium Phosphate
NIST_TCP = ...
[1.000E−03 4.162E+03
2.000E−03 6.571E+02
3.000E−03 4.166E+02
4.000E−03 1.903E+02
5.000E−03 3.105E+02
6.000E−03 1.905E+02
7.000E−03 1.254E+02
8.000E−03 8.702E+01
9.000E−03 6.277E+01
1.000E−02 4.673E+01
1.100E−02 3.572E+01
1.200E−02 2.792E+01
1.300E−02 2.223E+01
1.400E−02 1.800E+01
1.500E−02 1.478E+01
1.600E−02 1.229E+01
1.700E−02 1.033E+01
1.800E−02 8.771E+00
1.900E−02 7.514E+00
2.000E−02 6.489E+00
2.100E−02 5.645E+00
2.200E−02 4.945E+00
2.300E−02 4.359E+00
2.400E−02 3.864E+00
2.500E−02 3.444E+00
2.600E−02 3.085E+00
2.700E−02 2.777E+00
2.800E−02 2.510E+00
2.900E−02 2.279E+00
3.000E−02 2.077E+00
3.100E−02 1.900E+00
3.200E−02 1.744E+00
3.300E−02 1.606E+00
3.400E−02 1.484E+00
3.500E−02 1.375E+00
3.600E−02 1.278E+00
3.700E−02 1.190E+00
3.800E−02 1.112E+00
3.900E−02 1.042E+00
4.000E−02 9.779E−01
4.100E−02 9.202E−01
```

```
4.200E-02 8.677E-01
4.300E-02 8.200E-01
4.400E-02 7.764E-01
4.500E-02 7.366E-01
4.600E-02 7.002E-01
4.700E-02 6.667E-01
4.800E-02 6.359E-01
4.900E-02 6.076E-01
5.000E-02 5.814E-01
5.100E-02 5.572E-01
5.200E-02 5.348E-01
5.300E-02 5.140E-01
5.400E-02 4.947E-01
5.500E-02 4.768E-01
5.600E-02 4.601E-01
5.700E-02 4.445E-01
5.800E-02 4.299E-01
5.900E-02 4.163E-01
6.000E-02 4.035E-01
6.100E-02 3.915E-01
6.200E-02 3.803E-01
6.300E-02 3.697E-01
6.400E-02 3.598E-01
6.500E-02 3.505E-01
6.600E-02 3.416E-01
6.700E-02 3.333E-01
6.800E-02 3.254E-01
6.900E-02 3.180E-01
7.000E-02 3.110E-01
7.100E-02 3.043E-01
7.200E-02 2.980E-01
7.300E-02 2.920E-01
7.400E-02 2.863E-01
7.500E-02 2.808E-01
7.600E-02 2.757E-01
7.700E-02 2.708E-01
7.800E-02 2.661E-01
7.900E-02 2.616E-01
8.000E-02 2.574E-01
8.100E-02 2.533E-01
8.200E-02 2.494E-01
8.300E-02 2.457E-01
8.400E-02 2.421E-01
8.500E-02 2.387E-01
8.600E-02 2.355E-01
8.700E-02 2.323E-01
8.800E-02 2.293E-01
8.900E-02 2.264E-01
9.000E-02 2.236E-01
9.100E-02 2.210E-01
9.200E-02 2.184E-01
9.300E-02 2.159E-01
9.400E-02 2.136E-01
9.500E-02 2.113E-01
9.600E-02 2.090E-01
9.700E-02 2.069E-01
9.800E-02 2.048E-01
9.900E-02 2.029E-01
1.000E-01 2.009E-01 ];

% HA
% NIST_HA = ...
%    [0.0010
%     0.0050  313.0000
%     0.0060  192.0000
```

```
%     0.0080   87.9000
%     0.0100   47.2000
%     0.0150   14.9000
%     0.0200    6.5600
%     0.0300    2.1000
%     0.0400    0.9880
%     0.0500    0.5870
%     0.0600    0.4070
%     0.0800    0.2590
%     0.1000    ];


% %Air
% NIST_AIR = ...
%     [0.0010  3606
%      0.0015  1191
%      0.002   527.9
%      0.003   162.5
%      0.0032  134
%      0.004   77.88
%      0.0050  40.27
%      0.0060  23.41
%      0.0080  9.921
%      0.0100  5.120
%      0.0150    1.614
%      0.0200    0.7779
%      0.0300  0.3538
%      0.0400  0.2485
%      0.0500    0.2080
%      0.0600  0.1875
%      0.0800    0.1662
%      0.1000  0.1541 ];

% Air
NIST_AIR = ...
[1.000E-03 3.578E+03
2.000E-03 5.230E+02
3.000E-03 1.608E+02
4.000E-03 7.451E+01
5.000E-03 3.841E+01
6.000E-03 2.227E+01
7.000E-03 1.403E+01
8.000E-03 9.406E+00
9.000E-03 6.621E+00
1.000E-02 4.847E+00
1.100E-02 3.666E+00
1.200E-02 2.851E+00
1.300E-02 2.270E+00
1.400E-02 1.846E+00
1.500E-02 1.529E+00
1.600E-02 1.288E+00
1.700E-02 1.101E+00
1.800E-02 9.540E-01
1.900E-02 8.367E-01
2.000E-02 7.419E-01
2.100E-02 6.645E-01
2.200E-02 6.007E-01
2.300E-02 5.475E-01
2.400E-02 5.029E-01
2.500E-02 4.652E-01
2.600E-02 4.331E-01
2.700E-02 4.055E-01
2.800E-02 3.817E-01
2.900E-02 3.611E-01
3.000E-02 3.431E-01
```

3.100E−02 3.273E−01
3.200E−02 3.134E−01
3.300E−02 3.010E−01
3.400E−02 2.900E−01
3.500E−02 2.802E−01
3.600E−02 2.714E−01
3.700E−02 2.635E−01
3.800E−02 2.564E−01
3.900E−02 2.499E−01
4.000E−02 2.440E−01
4.100E−02 2.386E−01
4.200E−02 2.337E−01
4.300E−02 2.292E−01
4.400E−02 2.250E−01
4.500E−02 2.212E−01
4.600E−02 2.176E−01
4.700E−02 2.143E−01
4.800E−02 2.112E−01
4.900E−02 2.084E−01
5.000E−02 2.057E−01
5.100E−02 2.032E−01
5.200E−02 2.008E−01
5.300E−02 1.986E−01
5.400E−02 1.965E−01
5.500E−02 1.946E−01
5.600E−02 1.927E−01
5.700E−02 1.910E−01
5.800E−02 1.893E−01
5.900E−02 1.877E−01
6.000E−02 1.862E−01
6.100E−02 1.847E−01
6.200E−02 1.834E−01
6.300E−02 1.820E−01
6.400E−02 1.808E−01
6.500E−02 1.796E−01
6.600E−02 1.784E−01
6.700E−02 1.773E−01
6.800E−02 1.762E−01
6.900E−02 1.752E−01
7.000E−02 1.742E−01
7.100E−02 1.732E−01
7.200E−02 1.723E−01
7.300E−02 1.714E−01
7.400E−02 1.705E−01
7.500E−02 1.696E−01
7.600E−02 1.688E−01
7.700E−02 1.680E−01
7.800E−02 1.672E−01
7.900E−02 1.665E−01
8.000E−02 1.657E−01
8.100E−02 1.650E−01
8.200E−02 1.643E−01
8.300E−02 1.636E−01
8.400E−02 1.629E−01
8.500E−02 1.623E−01
8.600E−02 1.616E−01
8.700E−02 1.610E−01
8.800E−02 1.604E−01
8.900E−02 1.598E−01
9.000E−02 1.592E−01
9.100E−02 1.586E−01
9.200E−02 1.581E−01
9.300E−02 1.575E−01
9.400E−02 1.570E−01
9.500E−02 1.564E−01

```
9.600E-02 1.559E-01
9.700E-02 1.554E-01
9.800E-02 1.549E-01
9.900E-02 1.544E-01
1.000E-01 1.539E-01];

% Mass density of compounds
rho_bTCP = 3.07;     %[g/cm3] Beta Tricalcium phosphate
rho_AL = 2.699;      %[g/cm3] Aluminum
rho_ETH = 0.789;     %[g/ml]  Ethanol
rho_HA = 3.0;        % [g/cm^3]
rho_AIR = 0.0012;


% attenuation coefficients
mu_bTCP = NIST_TCP(:,2)*rho_bTCP;
mu_AL = NIST_AL(:,2)*rho_AL;
mu_ETH = NIST_ETH(:,2)*rho_ETH;
%mu_HA = NIST_HA_a*rho_HA;
mu_AIR = NIST_AIR(:,2)*rho_AIR;

energy = NIST_TCP(:,1)*1000;
% photon_energy=21;


%%plot of the NIST curves
% figure2 = figure('XVisual',...
%     '0x29 (TrueColor, depth 24, RGB mask 0xff0000 0xff00 0x00ff)');
% plot=semilogy(energy,mu_bTCP, energy,mu_AL, energy,mu_AIR, 'MarkerFaceColor','auto','LineWidth',3);
% grid on; hold on;
% xlabel('Photon energy [keV]','FontWeight','bold','FontSize',14);
% ylabel('$\mu_i$ $\mathbf{[cm^{1}]}$','Interpreter','latex',...
%     'FontWeight','bold',...
%     'FontSize',16);
% legend('bTCP','AL');
% set(plot1(1),'Marker','>','LineStyle','-.','Color', [0 0.498039215803146 0]);
% set(plot1(2),'Marker','square','LineStyle','--', 'Color', 'r');
% axis([0 100 0 525]);
% axes1 = axes('YScale','log','FontWeight',...
%        'bold','FontSize',14);

%
%    xaxis=1:100;
% % attenuation coefficient vs energy
% figure1=figure
% plot=semilogy(energy, mu_bTCP,'k -', energy, mu_AL,'k --', energy, mu_AIR,'k :', energy, mu_ETH,'k .-','LineWid
% legend({'$\mu_{\beta-TCP}$', '$\mu_{Al}$', '$\mu_{air}$', '$\mu_{C_2H_6O}$'}, 'interpreter', 'latex', 'FontSize
% xlabel('Photon energy [keV]','FontSize', 18, 'FontName', 'Times');
% ylabel({'$\mu_{i}$ [cm$^{-1}$]'},'interpreter', 'latex', 'FontSize', 20, 'FontName', 'Times','FontWeight', 'bol
% axis([5 50 0 1000]);%zoomed axis, xaxis:10-30kev yaxis for mus: air:0-4.3, eth:0-2200, al:0-6300, bTCP:0-13000
% %grid on;



% plot(energy,mu_AIR);
% xlabel('Energy [keV]','FontSize', 12, 'FontName', 'Times','FontWeight', 'bold');
% ylabel('attenuation coefficient [cm^{-1}]','FontSize', 13, 'FontName', 'Times','FontWeight', 'bold');
% axis([0 100 0 4.3]);


%% FIT FUNCTIONS FOR CALCULATING MASS ATTENUATION COEFFICIENTS for main script
%b_TCP
% cfun = fit(energy,NIST_TCP, 'cubicspline');
% mass_ac_scaffold = feval(cfun,photon_energy);
mass_ac_scaffold = NIST_TCP(photon_energy,2);
```

```
mu_bTCP_theoretical = mass_ac_scaffold*rho_bTCP;

% ETHANOL
% cfun = fit(energy,NIST_ETH, 'cubicspline');
% mass_ac_ETH = feval(cfun,photon_energy)
mass_ac_ETH = NIST_ETH(photon_energy,2);
mu_ETH_theoretical = mass_ac_ETH*rho_ETH;

% ALUMINIUM
% cfun = fit(energy,NIST_AL(:,2), 'cubicspline');
% mass_ac_AL = feval(cfun,photon_energy);

mass_ac_AL = NIST_AL(photon_energy,2);
mu_AL_theoretical = mass_ac_AL*rho_AL;

% AIR
cfun = fit(NIST_AIR(:,1)*1000,NIST_AIR(:,2), 'cubicspline');
mass_ac_AIR = feval(cfun,photon_energy);
mu_AIR_theoretical = mass_ac_AIR*rho_AIR;
```

```
function [nanop,threshold]=nanopores(a, b, GV_ETH, GV_AL, GV_E21, GV_max, hist_all, mu_ETH_theoretical, mu_AIR_th
bins=0:GV_max(scaffold_number);
mu = bins*a+b
if scaffold_number <= 10 %scaffolds before cell culture (scaffolds used are: 1,2,4,5,7, and 8)
    nanop = (mu-mu_bTCP_theoretical)/(mu_AIR_theoretical-mu_bTCP_theoretical);
else
    nanop = (mu-mu_bTCP_theoretical)/(mu_ETH_theoretical-mu_bTCP_theoretical); % scaffolds after cell culture (sc

end
% min value should always be between GV_ethanol and GV_aluminium !?
indx_lower=GV_ETH; % ethanol
indx_higher=GV_AL; % aluminium

[xx,indx]=min(hist_all(indx_lower:indx_higher));
threshold=(indx_lower+indx)-1
```

```
for z=1:(build_dimz)
    for y=1:build_dimy
        for x=1:build_dimx

            if (volumes(x,y,z) < threshold)
                volumes(x,y,z) = 0; % Below threshold is put to zero
            else
                if  (volumes(x,y,z) > GV_max(scaffold_number));
                    volumes(x,y,z) = GV_max(scaffold_number); % above GV_max is put to equal to GV_max to get [0:
                end
            end

        end
    end
    disp(['running ',num2str(z),'/',num2str(build_dimz)])
end

save(['cleaned_volume/',folder,'_',scaffold,'_','cleaned_volume.mat'])


for z=1:build_dimz
    disp(['running ',num2str(z),'/',num2str(build_dimz)])
    imwrite(volumes(:,:,z),[dir,'/cleaned/',scaffold,'_',num2str(z),'.tif']);
end
```

```
function [E3,nu31,G12]=hom_scaffold_clean(nanop_clean)

% ******************************************************
% TENSOR DEFINITION
% ******************************************************
% 4th-order identity tensor
I=[1 0 0 0 0 0; 0 1 0 0 0 0; 0 0 1 0 0 0; 0 0 0 1 0 0; 0 0 0 0 1 0; 0 0 0 0 0 1];
% volumetric part of the 4th-order identity tensor
J=[1/3 1/3 1/3 0 0 0; 1/3 1/3 1/3 0 0 0; 1/3 1/3 1/3 0 0 0; 0 0 0 0 0 0; 0 0 0 0 0 0; 0 0 0 0 0 0];
% deviatoric part of the 4th-order identity tensor
K=I-J;
% second-order unit tensor
one2=eye(3);


% ******************************************************
% NEEDLE FAMILIES HA
% ******************************************************
% total number of families between 0..pi/2 and for phi between O and pi
weight=1/15;
r=1/2;
s=(sqrt(5)+1)/4;
t=(sqrt(5)-1)/4;

vector_cos_theta=[t t t t s s s s r r r r 0 0 1];
vector_sin_theta_sin_phi=[+s -s +s -s +r -r +r -r +t -t +t -t 0 1 0];
vector_sin_theta_cos_phi=[+r +r -r -r +t +t -t -t +s +s -s -s 1 0 0];

max_fam = length(vector_cos_theta) ;

% bulk modulus fluid
k_pore  = 2.3;
% elastic parameters mineral
k_CaP=82; % bulk modulus
mu_CaP=43.2; % Shear modulus

c_pore  = 3*k_pore*J; % Stiffness tensor of pores
c_CaP=2*mu_CaP*K+3*k_CaP*J; % Calculation of stiffnesstensor with I;J;K tensors

E1=zeros(1,length(nanop_clean));
E3=zeros(1,length(nanop_clean));
nu31=zeros(1,length(nanop_clean));
nu12=zeros(1,length(nanop_clean));
G12=zeros(1,length(nanop_clean));

counter=1;
for i=1:length(nanop_clean) % phi is the porosity
    phi=nanop_clean(i);

    if mod(i, 50)==0
        disp([num2str(i),'/', num2str(length(nanop_clean))]);
    end

% start with cwetcol as the C0-matrix
C0=c_CaP;
C0_old=0;



% iteration for calculation of self-consistent stiffness
while abs((norm(C0)-norm(C0_old))/norm(C0))>0.00001

% CONTRIBUTION OF NEEDLES

% Local and global coordinates initiation
```

```
help_IPcCaP=zeros(6,6);
help_pore=zeros(6,6);

% Stroud's integration formulae
% weight=1/15;
% r=1/2;
% s=(sqrt(5)+1)/4;
% t=(sqrt(5)-1)/4;
%
% vector_cos_theta=[t t t t s s s s r r r r 0 0 1];
% vector_sin_theta_sin_phi=[+s -s +s -s +r -r +r -r +t -t +t -t 0 1 0];
% vector_sin_theta_cos_phi=[+r +r -r -r +t +t -t -t +s +s -s -s 1 0 0];

for r=1:15
    coor1=vector_sin_theta_cos_phi(r);
    coor2=vector_sin_theta_sin_phi(r);
    coor3=vector_cos_theta(r);

 % evaluate P-tensor for oriented cylinders in anisotropic matrix
 Pcyl_CaP=P_iso_cyl(coor1,coor2,coor3,C0,J);

 % Calculation in global base: [I+P:(cHA-C0)]^-1 for solid phase (HA)
 A1=inv(I+Pcyl_CaP*(c_CaP-C0));
 help_IPcCaP = help_IPcCaP + weight*A1;

end

% CONTRIBUTION OF PORES
% evaluate P-tensor for spherical inclusions in anisotropic matrix
Psph_pore=P_iso_sph(C0,J,K);

% evaluate [I+P:(c-C0)]^-1 for pores (without integration)
help_pore=inv(I+Psph_pore*(c_pore-C0));

c_hom= ((1-phi)*c_CaP*help_IPcCaP+phi*c_pore*help_pore)*inv((1-phi)*help_IPcCaP+phi*help_pore);
C0_old=C0;
C0=c_hom;
D_hom=inv(c_hom);
end

C_homogenized(counter)=C0(3,3);
E1(i) =1/D_hom(1,1);
E3(i) =1/D_hom(3,3);
nu12(i) =-D_hom(1,2)*E1(i);
nu31(i) =-D_hom(1,3)*E3(i);
G12(i) =E1(i)/2*(1+nu12(i));
end

% save('workspace_after_hom_sc10.mat');
```

```
% % function []=make_histograms(hist_all, images_count, voxels, folder, scaffold )
%
% GRAY-VALUES
hist_gsc=figure
axes_gsc=axes('Parent',hist_gsc,'FontWeight','bold','FontSize',14);
bar(1:236,hist_all/(images_count*voxels),'k');
box(axes_gsc,'on');
grid(axes_gsc,'on');
hold(axes_gsc,'all');
axis([0 255 0 0.08]);
xlabel('X-ray attenuation [gray-scale values]','FontSize', 16, 'FontName', 'Times','FontWeight', 'bold');
ylabel('Probability density [-]','FontSize', 16, 'FontName', 'Times','FontWeight', 'bold');
title([folder,' ',scaffold])

saveas(hist_gsc,['hist_gsc_E21/',folder,'_',scaffold,'_E21','.eps']);
saveas(hist_gsc,['hist_gsc_E21/',folder,'_',scaffold,'_E21','.fig']);



% HISTOGRAM OG ALL SCAFFOLDS AND BTCP THEORETICAL
bins=0:235
x=(bins-b)/a;
y=hist_all/(images_count*voxels);

mu_max_8=(235-b)/a;  %breyta!!
data_8=[x;y];

save('data_temp_max/data_8.mat','mu_max_8','data_8');  % breyta!!

figure
plot(data_1(1,:),data_1(2,:),data_2(1,:),data_2(2,:),data_4(1,:),...
    data_4(2,:),data_5(1,:),data_5(2,:),data_7(1,:),data_7(2,:),...
    data_8(1,:),data_8(2,:),data_11(1,:),data_11(2,:),data_12(1,:),...
    data_12(2,:),data_14(1,:),data_14(2,:),data_15(1,:),data_15(2,:),...
    data_17(1,:),data_17(2,:),data_18(1,:),data_18(2,:));
axis([0 100 0 1.5]);
xlabel('X-ray attenuation [cm^{-1}]','FontSize', 16, 'FontName', 'Times','FontWeight', 'bold');
ylabel('Probability density [-]','FontSize', 16, 'FontName', 'Times','FontWeight', 'bold');

line([mu_max_1 mu_max_1], [0 0.07])
line([mu_max_2 mu_max_2], [0 0.07])
line([mu_max_4 mu_max_4], [0 0.07])
line([mu_max_5 mu_max_5], [0 0.07])
line([mu_max_7 mu_max_7], [0 0.07])
line([mu_max_8 mu_max_8], [0 0.07])
line([mu_max_11 mu_max_11], [0 0.07])
line([mu_max_12 mu_max_12], [0 0.07])
line([mu_max_14 mu_max_14], [0 0.07])
line([mu_max_15 mu_max_15], [0 0.07])
line([mu_max_17 mu_max_17], [0 0.07])
line([mu_max_18 mu_max_18], [0 0.07])

% line([mu_E21_1 mu_E21_1], [0 0.07])
% line([mu_E21_2 mu_E21_2], [0 0.07])
% line([mu_E21_4 mu_E21_4], [0 0.07])
% line([mu_E21_5 mu_E21_5], [0 0.07])
% line([mu_E21_7 mu_E21_7], [0 0.07])
% line([mu_E21_8 mu_E21_8], [0 0.07])
% line([mu_E21_11 mu_E21_11], [0 0.07])
% line([mu_E21_12 mu_E21_12], [0 0.07])
% line([mu_E21_14 mu_E21_14], [0 0.07])
% line([mu_E21_15 mu_E21_15], [0 0.07])
% line([mu_E21_17 mu_E21_17], [0 0.07])
% line([mu_E21_18 mu_E21_18], [0 0.07])
```

```
% ATTENUATION-COEFFICIENTS
% bins=0:255;
% hist_ac=figure
% axes_ac=axes('Parent',hist_ac,'FontWeight','bold','FontSize',14);
% bar((bins-b)/a,hist_all/(images_count*voxels),'k');
% box(axes_ac,'on');
% grid(axes_ac,'on');
% hold(axes_ac,'all');
% axis([0 50 0 0.05]);
% xlabel('X-ray attenuation [cm^-1]','FontSize', 16, 'FontName', 'Times','FontWeight', 'bold');
% ylabel('Probability density [-]','FontSize', 16, 'FontName', 'Times','FontWeight', 'bold');
% title([folder,' ',scaffold])
%
% saveas(hist_ac,['hist_ac_E21/',folder,'_',scaffold,'.eps']);
% saveas(hist_ac,['hist_ac_E21/',folder,'_',scaffold,'.fig']);


% NANOPOROSITY
%nano_fit=fit(bins(:),nanp(:),'cubicspline')

% nanop_threshold=nanop(threshold);
% belowth = find(nanop>nanop_threshold);
%
% temp=sum(hist_all(belowth))+hist_all(threshold);
% hist_all(belowth) = 0;

% nanop=1 at GV_Air !
% GV_AIR [0:255] !
% nanop1=GV_AIR(scaffold_number)+1;
% hist_all(nanop1)=temp;
%
% hist_nanop=figure
% axes_nanop = axes('Parent',hist_nanop,'FontWeight','bold','FontSize',14);
% % bar((bins-mu_bTCP)/(mu_AIR-mu_bTCP),hist_all/(images_count*voxels),'k');
% bar(nanop,hist_all/(images_count*voxels),'k');
% % bar((bins-b(9))/a(9),hist_all/(images_count*voxels),'k');
% % bar(bins,hist_all/(images_count*voxels),'k');
% %xlim(axes_nanop,[0 1.6]);
% box(axes_nanop,'on');
% grid(axes_nanop,'on');
% hold(axes_nanop,'all');
% axis([0 1.6 0 0.05]);
% xlabel('Voxel-specific nanoporosities [-]','FontSize', 16, 'FontName', 'Times','FontWeight', 'bold');
% ylabel('Probability density [-]','FontSize', 16, 'FontName', 'Times','FontWeight', 'bold');
% title([folder,' ',scaffold])
%
% saveas(hist_nanop,['hist_nanop/',folder,'_',scaffold,'.eps']);
% saveas(hist_nanop,['hist_nanop/',folder,'_',scaffold,'.fig']);

% NANOPOROSITY, CLEANED IMAGES
hist_nanop_clean=figure
axes_nanop_clean=axes('Parent',hist_nanop_clean,'FontWeight','bold','FontSize',14);
bar(nanop_clean,hist_all(GV_matrix)/(images_count*voxels),'k');
box(axes_nanop_clean,'on');
grid(axes_nanop_clean,'on');
hold(axes_nanop_clean,'all');
axis([0 1.6 0 0.05]);
xlabel('Voxel-specific nanoporosities [-]','FontSize', 16, 'FontName', 'Times','FontWeight', 'bold');
ylabel('Probability density [-]','FontSize', 16, 'FontName', 'Times','FontWeight', 'bold');
title([folder,' ',scaffold])


%
```

```
% saveas(hist_nanop_clean,['hist_nanop_clean/',folder,'_',scaffold,'.eps']);
% saveas(hist_nanop_clean,['hist_nanop_clean/',folder,'_',scaffold,'.fig']);
%
% % HOMOGENIZATION OF NANOP
% hist_hom_nanop=figure
% plot(nanop)
% % axis([0 1.6 0 0.0001]);
% title([folder,' ',scaffold])
%  xlabel('X-ray attenuation [gray-scale values]');
%  ylabel('nanoporosity [-]');
%
%
% %
% %

% HOMOGENIZATION OF NANOP_CLEAN
hist_hom_nanop_clean=figure
subplot(2,1,1); plot(nanop_clean,E3,'r',nanop_clean,G12,'b')
axis([0 1 0 100]);
title(['Young''s modulus,',' ',folder,' ',scaffold,' ','nanop clean'])
legend('E3','G12');
 xlabel('nanoporosity [-]');
 ylabel('Young''s and shear moduli [GPa]');
subplot(2,1,2); plot(nanop_clean,nu31,'r')
axis([0 1 0.25 0.38]);
title(['Poissons ratio,',' ',folder,' ',scaffold,' ','nanop clean',' ',photon_energy])
legend('nu31');
 xlabel('nanoporosity [-]');
 ylabel('Poissons ratios [-]');
%
%  saveas(hist_hom_nanop_clean,['hist_hom_nanop_clean/',folder,'_',scaffold,'.eps']);
% saveas(hist_hom_nanop_clean,['hist_hom_nanop_clean/',folder,'_',scaffold,'.fig']);
```

```
%                                                                       %
% mf_generate_FE_new.m                                                  %
%                                                                       %
% Created by:           Agnes Czenek                                    %
% E-Mail:               agnesc08@ru.is                                  %
% Based on code by:     Romane Blanchard and Alexander Dejaco           %
% E-Mail:               romane.blanchard@tuwien.ac.at                   %
%                                                                       %
% Dependencies:         none                                            %
% Note:                 generates a list of the elements with           %
%                       their corresponding grey values                 %
%                                                                       %
%%%%%%%%%%%%%%%%%%%%%%%%%%%%%%%%%%%%%%%%%%%%%%%%%%%%%%%%%%%%%%%%%%%%%%


grouping_factor=4;
load(['cleaned_volume/',folder,'_',scaffold,'_cleaned_volume','.mat'])
dimx=size(volumes,1);
dimy=size(volumes,2);
dimz=size(volumes,3);
dimx=floor(dimx/grouping_factor);
dimy=floor(dimy/grouping_factor);
dimz=floor(dimz/grouping_factor);



disp(['Going to reduce voxel count ...']);

all_voxels=volumes;


if (grouping_factor == 1)
    reduced_voxels=zeros(dimx,dimy,dimz,'uint8');
    reduced_voxels=all_voxels;
else

for a=1:(size(all_voxels,1)/grouping_factor)
    tic
    for b=1:(size(all_voxels,2)/grouping_factor)
        for c=1:(size(all_voxels,3)/grouping_factor)
            a1=(a-1)*grouping_factor+1;a2=(a-1)*...
                grouping_factor+grouping_factor;
            b1=(b-1)*grouping_factor+1;b2=(b-1)*...
                grouping_factor+grouping_factor;
            c1=(c-1)*grouping_factor+1;c2=(c-1)*...
                grouping_factor+grouping_factor;
            reduced_voxels(a,b,c)=...
                uint8(round((sum(sum(sum(all_voxels(...
                a1:a2,b1:b2,c1:c2)))))/grouping_factor^3));
        end
    end
    duration = toc;
    disp(['Reduction of ', num2str(a),'/',...
        num2str(size(all_voxels,1)/grouping_factor), ...
        ' completed(', num2str(duration), ')']);
end

save(['reduced_volume/',folder,'_',scaffold,'reduced_volume.mat'],...
    'reduced_voxels', 'grouping_factor', 'folder', 'scaffold');
end

disp(['voxel reduction done ...'])
%%
%%%%%%%%%%%%%%%%%%%%%%%%%%%% ELEMENT DEFINITIONS %%%%%%%%%%%%%%%%%%%%%%%%%
```

```
disp(['generating elements...']);

size_1=1:dimx;
size_2=1:dimy;
size_3=1:dimz;
num=0;


%element_structure holds element number for coordinate xyz
for k=1:dimz
    k
    if k==1
        for j=dimy:-1:1
            my_element_structure(:,max(size_2)-(j-1),max(size_3))=...
                (j-1)*max(size_1)+size_1;
        end
    else
        my_element_structure(:,:,max(size_3)-(k-1))=...
            my_element_structure(:,:,max(size_3))+(k-1)*max(size_1)*...
                max(size_2);
    end
end

fp_el_grey = fopen(['el_grey/','el_grey_',folder,'_',scaffold,'.txt'],'w')
curr_el=0;

%elements_sorted(a,b) gives coordinate b (123 xyz) for element id
for x=1:dimx
    x
    for y=1:dimy
        for z=1:dimz
            if (reduced_voxels(x,y,z) > threshold)
                curr_el=curr_el+1;

                fprintf(fp_el_grey, '%i %i\n', my_element_structure(x,y,z), reduced_voxels(x,y,z));

            else
                continue
            end



        end
    end
end
fclose(fp_el_grey);


%% Generates file associating element number to porosity

e_table=importdata(['engineering_table/engineering_table_',folder,scaffold,'.txt']);

el_grey=importdata(['el_grey/el_grey_',folder,'_',scaffold,'.txt']);
% 1st: elnum
% 2nd: gsc

elnum_total=length(el_grey);
elnum=0;
GVnum=0;

fp_E3 = fopen(['el_grey/E3', folder, scaffold,'.txt'],'w');
fp_nu31 = fopen(['el_grey/nu31', folder, scaffold,'.txt'],'w');
fp_porosity = fopen(['el_grey/porosity', folder, scaffold,'.txt'],'w');
% vnu
% 1st: gsc
```

```
% 2nd: v

for jj=1:length(el_grey)
   curr_element=el_grey(jj,1);
   curr_el_gsc=el_grey(jj,2);
   idx=find(e_table(:,1)==curr_el_gsc);

   fprintf(fp_nu31, '%i %i\n', curr_element, e_table(idx, 4));
   fprintf(fp_E3, '%i %i\n', curr_element, e_table(idx, 3));
   fprintf(fp_porosity, '%i %i\n', curr_element, e_table(idx, 2));
end
    fclose(fp_E3);
    fclose(fp_nu31);
  fclose(fp_porosity);
```

```
%                                                   %
% generate_color_e.m                                %
%                                                   %
% Created by:           Agnes Czenek                %
% E-Mail:               agnesc08@ru.is              %
%                                                   %
% Based on code by:     Alexander Dejaco            %
% Dependencies:         getSlice_cryst              %
% Note:                 generate color images       %
%                                                   %
%%%%%%%%%%%%%%%%%%%%%%%%%%%%%%%%%%%%%%%%%%%%%%%%%%%


close all;
disp('importing data...')

load(['reduced_volume/',folder,'_',scaffold,'reduced_volume.mat']);

dimx=size(reduced_voxels,1);
dimy=size(reduced_voxels,2);
dimz=size(reduced_voxels,3);
vDimx=1:dimx;
vDimy=1:dimy;
vDimz=1:dimz;
num=0;


disp('generating element structures...')


vvvElStruc=zeros(dimx,dimy,dimz);

% element number for coordinate xyz
for k=1:dimz
    if k==1
        for j=dimy:-1:1
            vvvElStruc(:,dimy-(j-1),dimz)=(j-1)*dimx+vDimx;
        end
    else
        vvvElStruc(:,:,dimz-(k-1))=vvvElStruc(:,:,dimz)+(k-1)*dimx*dimy;
    end
end

%elements_sorted(a,b) gives coordinate b (123 xyz) for element id
vvElCoord=zeros(dimx*dimy*dimz,3);
for x=1:dimx
    for y=1:dimy
        for z=1:dimz
            vvElCoord(vvvElStruc(x,y,z),1)=x;
            vvElCoord(vvvElStruc(x,y,z),2)=y;
            vvElCoord(vvvElStruc(x,y,z),3)=z;
        end
    end
end

disp('importing data...')

% need a column with element number and others with data
data=importdata(['el_grey/E3', folder, scaffold, '.txt']);

disp('calculating data...')

vModelEl = data(:,1); %.. elNum
vEV = data(:,2); %..
```

```
disp('generating x crossection...')
for curr_cs=1:dimx
    disp(['generating x crossection ', num2str(curr_cs)])
    clear vCsIndices
    clear vCsEl
    clear v2CsX

    SLICENUMX=curr_cs;
    % populate element numbers in the crossection
    vCsEl=vvvElStruc(SLICENUMX,vDimy,vDimz);
    vCsEl=vCsEl(:);

    [c,ia,vCsIndices] = intersect(vCsEl, vModelEl);
    vCsXEl   = vModelEl(vCsIndices);
    v2CsX(:,1) = vEV(vCsIndices);

    for nn=1:1
        clear imgX;
        imgX=zeros(dimy,dimz);
        for yy=1:dimy
            for zz=1:dimz
                imgX(yy,zz)=-20;
            end
        end

        for i=1:length(v2CsX(:,nn))
            value = v2CsX(i,nn);
            yCoord=vvElCoord(vCsXEl(i),2);
            zCoord=vvElCoord(vCsXEl(i),3);
            assert(vvElCoord(vCsXEl(i),1)==curr_cs);
            imgX((dimy+1)-yCoord, (dimz+1)-zCoord) = value;
        end

        switch nn
            case 1
                path=sprintf(['x_sequence_',folder,'_',scaffold,'/','E3_', '_%i.png'], curr_cs);
                generate_color_image_cryst_rhoec(imgX,'x',dimx,dimy,dimz,path);
            otherwise
                assert(false);
        end
    end
end

%%%%%%%%%%%%%%%%%%%%%%%%%%%% Y - CS

% for curr_cs=1:dimy
%     disp(['generating y crossection ', num2str(curr_cs)])
%
%     clear vCsIndices
%     clear vCsEl
%     clear v2CsY
%
%     SLICENUMY=curr_cs;
%     % populate element numbers in the crossection
%     vCsEl=vvvElStruc(vDimx,SLICENUMY,vDimz);
%     vCsEl=vCsEl(:);
%
%     [c,ia,vCsIndices] = intersect(vCsEl, vModelEl);
%     vCsYEl   = vModelEl(vCsIndices);
%     v2CsY(:,1) = vEV(vCsIndices);
%
%     for nn=1:1
%         clear imgY;
%         imgY=zeros(dimz,dimx);
%         for zz=1:dimz
```

```
%             for xx=1:dimx
%                 imgY(zz,xx)=-20;
%             end
%         end
%
%         for i=1:length(v2CsY(:,nn))
%             value = v2CsY(i,nn);
%             assert(vvElCoord(vCsYEl(i),2)==curr_cs);
%             zCoord=vvElCoord(vCsYEl(i),3);
%             xCoord=vvElCoord(vCsYEl(i),1);
%
%             imgY(zCoord, (dimx+1)-xCoord) = value;
%         end
%
%         switch nn
%             case 1
%                 path=sprintf('GF7/y_sequence_rhoec/rhoec_%i.png', curr_cs);
%                 generate_color_image_cryst_rhoec(imgY,'y',dimx,dimy,dimz,path);
%
%             otherwise
%                 assert(false);
%         end
%     end
% end
%
% for curr_cs=1:dimz
%     clear vCsIndices
%     clear vCsEl
%     clear v2CsZ
%
%     SLICENUMZ=curr_cs; % cs is set by the calling script !
%
%     % populate element numbers in the crossection
%     vCsEl=vvvElStruc(vDimx,vDimy,SLICENUMZ);
%     vCsEl=vCsEl(:);
%
%     [c,ia,vCsIndices] = intersect(vCsEl, vModelEl);
%
%     vCsZEl   = vModelEl(vCsIndices);
%
%     v2CsZ(:,1) = vEV(vCsIndices);
%
%
%     %%%%%%%%%%%%%%%%%%%%%%%%%%%% Z - CS
%     disp(['generating z crossection ', num2str(curr_cs)])
%
%     for nn=1:1
%         clear imgZ;
%         imgZ=zeros(dimy,dimx);
%         for yy=1:dimy
%             for xx=1:dimx
%                 imgZ(yy,xx)=-20;
%             end
%         end
%
%         for i=1:length(v2CsZ(:,nn))
%             value = v2CsZ(i,nn);
%
%             assert(vvElCoord(vCsZEl(i),3)==curr_cs);
%             yCoord=vvElCoord(vCsZEl(i),2);
%             xCoord=vvElCoord(vCsZEl(i),1);
%
%             imgZ((dimy+1)-yCoord, (dimx+1)-xCoord) = value;
%         end
%
```

```
%         switch nn
%             case 1
%                 path=sprintf('GF5/z_sequence_rhoec/rhoec_%i.png', curr_cs);
%                 generate_color_image_cryst_rhoec(imgZ ,'z',dimx,dimy,dimz,path);
%
%             otherwise
%                 assert(false);
%         end
%     end
% end


disp('done')
```

```
function [ ] = generate_color_image_cryst_rhoec(img, crossection, dimx, dimy, dimz, path)
%
% generate_color_image_e.m
%
% Created by:           Alexander Dejaco
% E-Mail:               alexander.dejaco@tuwien.ac.at
%
% FUNCTION
%
% Parameters:           image data, selected crossection, dimensions,
%                       output path
% Note:                 print strain color images
%
%%%%%%%%%%%%%%%%
% %COLOUR SCALE FOR YOUNG'S MODULUS E3
COLORBANDS(1,1) =  70;
COLORBANDS(1,2) =  65;
COLORBANDS(2,1) =  65;
COLORBANDS(2,2) =  60;
COLORBANDS(3,1) =  60;%; % red-red-orange
COLORBANDS(3,2) =  55;
COLORBANDS(4,1) =  55; % red-orange
COLORBANDS(4,2) =  50;
COLORBANDS(5,1) =  50; % orange
COLORBANDS(5,2) =  45;
COLORBANDS(6,1) =  45; % yellow
COLORBANDS(6,2) =  40;
%zero %
COLORBANDS(7,1) = 40;%median(A); % lime-green
COLORBANDS(7,2) = 35 ;
COLORBANDS(8,1) = 35; % blue-green
COLORBANDS(8,2) = 30;
COLORBANDS(9,1) = 30; % bright-blue
COLORBANDS(9,2) = 25;
COLORBANDS(10,1)= 25; % sky-blue
COLORBANDS(10,2)= 20;
COLORBANDS(11,1)= 20; % darker blue
COLORBANDS(11,2)= 15;
COLORBANDS(12,1)= 15; % dark blue
COLORBANDS(12,2)= 10;

% %COLOUR SCALE FOR POISSON'S RATIO NU31
% THIS SCALE IS USED FOR THE POISSONS RATIO !!!
%
% COLORBANDS(1,1) =  0.262;
% COLORBANDS(1,2) =  0.2585;
% COLORBANDS(2,1) =  0.2585;
% COLORBANDS(2,2) =  0.255;
% COLORBANDS(3,1) =  0.255;%; % red-red-orange
% COLORBANDS(3,2) =  0.2515;
% COLORBANDS(4,1) =  0.2515; % red-orange
% COLORBANDS(4,2) =  0.2480;
% COLORBANDS(5,1) =  0.2480; % orange
% COLORBANDS(5,2) =  0.2445;
% COLORBANDS(6,1) =  0.2445; % yellow
% COLORBANDS(6,2) =  0.241;
% % zero %
% COLORBANDS(7,1) = 0.241;%median(A); % lime-green
% COLORBANDS(7,2) = 0.2375 ;
% COLORBANDS(8,1) = 0.2375; % blue-green
% COLORBANDS(8,2) = 0.2340;
% COLORBANDS(9,1) = 0.2340; % bright-blue
% COLORBANDS(9,2) = 0.2305;
% COLORBANDS(10,1)= 0.2305; % sky-blue
% COLORBANDS(10,2)= 0.2270;
```

```
% COLORBANDS(11,1)= 0.2270; % darker blue
% COLORBANDS(11,2)= 0.2235;
% COLORBANDS(12,1)= 0.2235; % dark blue
% COLORBANDS(12,2)= 0.22;

%COLOUR SCALE FOR POROSITY
% COLORBANDS(1,1) =  0.7;
% COLORBANDS(1,2) =  0.65;
% COLORBANDS(2,1) =  0.65;
% COLORBANDS(2,2) =  0.6;
% COLORBANDS(3,1) =  0.6;%; % red-red-orange
% COLORBANDS(3,2) =  0.55;
% COLORBANDS(4,1) =  0.55; % red-orange
% COLORBANDS(4,2) =  0.50;
% COLORBANDS(5,1) =  0.50; % orange
% COLORBANDS(5,2) =  0.45;
% COLORBANDS(6,1) =  0.45; % yellow
% COLORBANDS(6,2) =  0.40;
% % zero %
% COLORBANDS(7,1) = 0.40;%median(A); % lime-green
% COLORBANDS(7,2) = 0.35 ;
% COLORBANDS(8,1) = 0.35; % blue-green
% COLORBANDS(8,2) = 0.30;
% COLORBANDS(9,1) = 0.30; % bright-blue
% COLORBANDS(9,2) = 0.25;
% COLORBANDS(10,1)= 0.25; % sky-blue
% COLORBANDS(10,2)= 0.2;
% COLORBANDS(11,1)= 0.2; % darker blue
% COLORBANDS(11,2)= 0.15;
% COLORBANDS(12,1)= 0.15; % dark blue
% COLORBANDS(12,2)= 0.1;

switch(crossection)
    case 'x'
        dimn=dimy;
        dimm=dimz;
        disp(['x dimn:',num2str(dimn),' dimm:',num2str(dimm)])
    case 'y'
        dimn=dimz;
        dimm=dimx;
        disp(['y dimn:',num2str(dimn),' dimm:',num2str(dimm)])
    case 'z'
        dimn=dimy;
        dimm=dimx;
        disp(['z dimn:',num2str(dimn),' dimm:',num2str(dimm)])
    otherwise
        assert(false)
end

imgXcolor=uint8(zeros(dimn,dimm,3));

for n=1:dimn
    for m=1:dimm
        value=double(img((dimn+1)-n,(dimm+1)-m));

        if value >= COLORBANDS(1,2)
            %   r=191;
            %   g=0;
            %   b=200;
            r=255;
            g=0;
            b=0;
        else
            if (( value < COLORBANDS(2,1) ) && ( value >= COLORBANDS(2,2) ))
                %   r=255;
```

```
    %   g=0;
    %   b=127;
    r=0;
    g=255; % LIME—GREEN
    b=0;
else
    if (( value < COLORBANDS(3,1) ) && ( value >= COLORBANDS(3,2) ))
        r=255;
        g=0;
        b=0;
    else
        if (( value < COLORBANDS(4,1) ) && ( value >= COLORBANDS(4,2) ))
            r=255;
            g=141;
            b=0;
        else
            if (( value < COLORBANDS(5,1) ) && ( value >= COLORBANDS(5,2) ))
                r=255;
                g=204;
                b=0;
            else
                if (( value < COLORBANDS(6,1) ) && ( value >= COLORBANDS(6,2) ))
                    %             if (value == 0)
                    %                 r=80;
                    %                 g=80;
                    %                 b=130;
                    %             else
                    r=255;
                    g=255; % YELLOW
                    b=0;
                    %             end
                else %%%%%% ZERO %%%%%%%
                    if (( value < COLORBANDS(7,1) ) && ( value >= COLORBANDS(7,2) ))
                        r=0;
                        g=255; % LIME—GREEN
                        b=0;
                    else
                        if (( value < COLORBANDS(8,1) ) && ( value >= COLORBANDS(8,2) ))
                            r=0;
                            g=255;
                            b=178;
                        else
                            if (( value < COLORBANDS(9,1) ) && ( value >= COLORBANDS(9,2) ))
                                r=0;
                                g=255;
                                b=255;
                            else
                                if (( value < COLORBANDS(10,1) ) && ( value >= COLORBANDS(10,2) ))
                                    r=0;
                                    g=157;
                                    b=255;
                                else
                                    if (( value < COLORBANDS(11,1) ) && ( value >= COLORBANDS(11,2) )
                                        r=0;
                                        g=59;
                                        b=255;
                                    else
                                        if value < COLORBANDS(12,1)
                                            if value == —20
                                                r=80;
                                                g=80;
                                                b=130;
                                            else
                                                r=0;
                                                g=0;
```

```
                                                    b=180;
                                                end
                                            else
                                                disp('outside, stopping!');
                                                disp(num2str(value))
                                                disp(num2str(n))
                                                disp(num2str(m))
                                                assert(false)
                                            end
                                        end
                                    end
                                end
                            end
                        end
                    end
                end
            end
        end

        imgXcolor((dimn+1)-n,(dimm+1)-m,1)=r;
        imgXcolor((dimn+1)-n,(dimm+1)-m,2)=g;
        imgXcolor((dimn+1)-n,(dimm+1)-m,3)=b;
    end
end

%imwrite(imgXcolor, path,'tiff','ColorSpace','icclab','Compression','none','Description','created by alexander.de
 imwrite(imgXcolor, path, 'png', 'Description','created by alexander.dejaco@tuwien.ac.at', 'bitdepth', 8);

end
```

The script for the back calculation of the photon energy of the microCT equipment which is done based on the formula referring to the linear relationship between grey values and attenuation coefficients. The function and the principles of the back calculation are the following:
The energy is recalculated for each scaffold data. First the data's are imported, the peak of air, aluminium is given and the max grey value of each data also like in main script and the mass density of β-TCP and ethanol is given.
Energy is selected from 1 to 100 for the materials in NIST database in order to find the exact energy which the microCT is using for image acquisition.
In the for loop, the energy is changing and a function is created bringing the attenuation coefficients (μ) from NIST data base for each material which is used (bTCP, ETH, AIR, and AL). The attenuation coefficients are saved as vectors in next step. The most frequent grey values (peaks) are named again example: GVair is GVleft, GVphantom is GVal and GVright is GVmax. The attenuation coefficients (μ) are also renamed and these values are put into the formula containing the proportionality constants a and b. the maximum attenuation coefficient (mu_max_vec) is calculated with the next formula, in this formula the maximum GV is used which is varying between data sets and it is needed to be changed manually !!
The final procedure is to calculate the ratio for the energy plot: if the ratio between β-TCP from NIST database and β-TCP from the CT scan data sets are equal to one that means that the attenuation coefficient of the pure β-TCP at NIST data base is equal to the attenuation coefficient of the scaffolds material. The ratio in our case was never one thus the voxels presented with grey values does not contain fully dense scaffold's material. The results which were gained from the energy plots was that the minimum and also the unique value, 21 keV for each and every data set from the CT images which is assumed to be the average energy which the microCT equipment used for the image acquisition.

```
%%%%%%%%%%%%%%%%%%%%%%%%%%%%%%%%%%%%%%%%%%%%%%%%%%%%%%%%%%%%%%%%%%%%%%%%%%%%%%%%
%                                                                                 %
% mainScript_Efunction.m: main script to backcompute energy                       %
%                                                                                 %
% dependencies:fun_NIST_A, import_images                                          %
% IMWS——TU WIEN                                                                   %
%                                                                                 %
%%%%%%%%%%%%%%%%%%%%%%%%%%%%%%%%%%%%%%%%%%%%%%%%%%%%%%%%%%%%%%%%%%%%%%%%%%%%%%%%


close all; clear all; clc;
disp(['starts script'])


% Loop over the scaffolds:
% (to study only one scaffold, erase/comment "for scaffold_iteration=1:12"
% and assign scaffold_iteration=number of the scaffold (from 1 to 12))
for scaffold_iteration=1:12
    switch scaffold_iteration
        % cases 1—6: empty
        case 1 %I
            folder='empty_8bit'
            scaffold_number=1 %used for calculation a and b; 1—20
            scaffold='scaffold1'
            images_count=1170
        case 2 %II
            folder='empty_8bit'
            scaffold_number=2 %used for calculation a and b; 1—20
            scaffold='scaffold2'
            images_count=994
        case 3 %III
            folder='empty_8bit'
            scaffold_number=4 %used for calculation a and b; 1—20
            scaffold='scaffold4'
            images_count=854
```

```
    case 4 %IV
        folder='empty_8bit'
        scaffold_number=5 %used for calculation a and b; 1-20
        scaffold='scaffold5'
        images_count=804
    case 5 %V
        folder='empty_8bit'
        scaffold_number=7 %used for calculation a and b; 1-20
        scaffold='scaffold7'
        images_count=880
    case 6 %VI
        folder='empty_8bit'
        scaffold_number=8 %used for calculation a and b; 1-20
        scaffold='scaffold8'
        images_count=802

        % cases 7 and 8: 3 weeks
    case 7 %I
        folder='3weeks_8bit'
        scaffold_number=11 %used for calculation a and b; 1-20
        scaffold='scaffold1_3w'
        images_count=770
    case 8 %II
        folder='3weeks_8bit'
        scaffold_number=12 %used for calculation a and b; 1-20
        scaffold='scaffold2_3w'
        images_count=1000
        % cases 9 and 10: 6 weeks
    case 9 %II
        folder='6weeks_8bit'
        scaffold_number=14 %used for calculation a and b; 1-20
        scaffold='scaffold4_6w'
        images_count=906
    case 10 %IV
        folder='6weeks_8bit'
        scaffold_number=15 %used for calculation a and b; 1-20
        scaffold='scaffold5_6w'
        images_count=918

        % cases 11 and 12: 8 weeks
    case 11 %V
        folder='8weeks_8bit'
        scaffold_number=17 %used for calculation a and b; 1-20
        scaffold='scaffold7_8w'
        images_count=1015
    case 12 %VI
        folder='8weeks_8bit'
        scaffold_number=18 %used for calculation a and b; 1-20
        scaffold='scaffold8_8w'
        images_count=826
end


% Directory name to read the images -- Agnes
dir=['/ct_images/',folder,'/',scaffold];
% Directory name -- Romane
%dir=['~/Documents/Agnes/BACKUP/ct_images/',folder,'/',scaffold];


% If the .mat file exists, loads the file, else run the script
% import_images to save the .mat_file
if exist(['raw_volume/',folder,'_',scaffold,'_','raw_volume.mat'])==0;
    import_images;
else
    load(['raw_volume/',folder,'_',scaffold,'_','raw_volume.mat']);
```

```
end

% Table 1
GV_AIR = [77; 55; 70; 44; 42; 59; 64; 65; 39; 36; 37; 57; 80; 56; 71; 44; 71; 39; 55; 62; 82];
GV_AL =  [165;157;159;168;165;167;163;144;180;184;184;133;185;155;171;179;177;122;169; 105; 130];
GV_max = [245;240;0;239;246;  0; 240;235; 0;   0;240; 167;   0;  198;212;   0; 227;157;0;0];
GV_SC_vec =[204;193;188;190;203;195;196;191;185;189;194;138; 194; 163; 178; 188; 191;128;180; 198]; %peak of


% Mass densities
rho_bTCP = 3.07;    % g/cm3 mass density of CaP scaffold
rho_ETH = 0.789;    % g/cm3 mass density of ethanol

% Loop over the energies [kev]
disp(['loop over energy...']);

for ii=1:100
    photon_energy=ii;

    % Computes the X-ray attenuation coefficient depending on energies (Fig. 3)
    fun_NIST_A;

    % Saves the attenuation coefficients as vectors
    mu_bTCP_vec(ii)=mu_bTCP_theoretical; mu_ETH_vec(ii)=mu_ETH_theoretical;
    mu_AL_vec(ii)=mu_AL_theoretical; mu_AIR_vec(ii)=mu_AIR_theoretical;
end
disp(['done']);


%% Assignements
% Peaks from histogram, to be modified
GV_left=GV_AIR(scaffold_number); % left peak (air)
GV_phantom= GV_AL(scaffold_number); % GV of the phantom that you recorded after cropping
GV_right= GV_SC_vec(scaffold_number); % maximum grey value of the histogram


% assigns attenuation coefficients
mu_left_vec=mu_AIR_vec;
mu_phantom_vec=mu_AL_vec;
mu_right_vec=mu_bTCP_vec;

% Computes coefficients a and b, still depending on the energy [Eq.(2)]
b_vec= (mu_left_vec*GV_phantom-mu_phantom_vec*GV_left)./(GV_phantom-GV_left)
a_vec=(mu_left_vec-mu_phantom_vec)./(GV_left-GV_phantom)

% Computes the attenuation coefficient at the top of the scaffold peak
mu_peak_vec=a_vec*GV_right+b_vec;

% ratio to find energy as minimum of the curve Eq.(7)
ratio=mu_peak_vec./mu_bTCP_vec;
ratio4plot(scaffold_iteration,:)=ratio;

% nanoporosity at the peak of scaffold Eq.(4) and (5)
if scaffold_number<=10
    phi_peak_vec=(mu_peak_vec-mu_bTCP_vec)./(mu_AIR_vec-mu_bTCP_vec);
else
    phi_peak_vec=(mu_peak_vec-mu_bTCP_vec)./(mu_ETH_vec-mu_bTCP_vec);
end
% saves the nanoporosity for each scaffold in an vector
phi4plot(scaffold_iteration, :)=phi_peak_vec;

% Finds the maximum of the curve, or unique value
[maxR, maxIndex]=max(phi_peak_vec(5:100));
% Saves in a vector the scaffold number (1 to 12), the value at the
% maximum of the curve and the index of the maximum
```

```
    uniquePoint(scaffold_iteration,:)=[scaffold_iteration, maxR, maxIndex];


end

disp(['Plotting...']);
%% Plots
% energy values
xaxis=1:100;
% time (in weeks)
xaxis2=[0 0 0 0 0 0 3 3 6 6 8 8];

% Nanoporosity as function of the energy for all 12 scaffolds
figure0=figure;
axes0 = axes('Parent',figure0,'FontWeight','bold','FontSize',14);
hold(axes0,'all');
grid (axes0,'on');
plot(xaxis, phi4plot(1,:),'LineWidth',3,'Color',[0 0 0]);
plot(xaxis, phi4plot(2,:),'LineWidth',2,'LineStyle','--','Color',[0 0 0]);
plot(xaxis, phi4plot(3,:), 'Marker','o','LineWidth',1,'LineStyle','none','Color',[0 0 0]);
plot(xaxis, phi4plot(4,:),'LineWidth',3,'LineStyle',':','Color',[0 0 0]);
plot(xaxis, phi4plot(5,:),'LineWidth',2,'LineStyle','-.','Color',[0 0 0]);
plot(xaxis, phi4plot(6,:), 'LineWidth',1,...
    'Color',[0.0392156876623631 0.141176477074623 0.415686279535294]);
plot(xaxis, phi4plot(7,:),'LineWidth',3,'Color',[1 0.694117665290833 0.39215686917305]);
plot(xaxis, phi4plot(8,:), 'LineWidth',2,'LineStyle','--',...
    'Color',[1 0.694117665290833 0.39215686917305]);
plot(xaxis, phi4plot(9,:),'Marker','o','LineWidth',1,'LineStyle','none','Color',[0 0 1]);
plot(xaxis, phi4plot(10,:),'LineWidth',3,'LineStyle',':','Color',[0 0 1]);
plot(xaxis, phi4plot(11,:), 'LineWidth',2,'LineStyle','-.',...
    'Color',[0.847058832645416 0.160784319043159 0]);
plot(xaxis, phi4plot(12,:), 'Color',[0.847058832645416 0.160784319043159 0]);
xlim([5 50]);
ylim([0 0.6]);
% Create xlabel
xlabel({'Energy [keV]'},'FontWeight','bold','FontSize',16,...
    'FontName','Times');
% Create ylabel
ylabel({'Nanoporosity [cm^{-1}]'},'FontWeight','bold','FontSize',16,...
    'FontName','Times');
% Create legend
legend0 = legend({'scaffold I', 'scaffold II', 'scaffold III', 'scaffold IV',...
    'scaffold V', 'scaffold VI', 'scaffold I, 3 weeks after culture',...
    'scaffold II, 3 weeks after culture', 'scaffold III, 6 weeks after culture',...
    'scaffold IV, 6 weeks after culture', 'scaffold V, 8 weeks after culture', ...
    'scaffold VI, 8 weeks after culture'}, 'Fontname', 'Times',...
    'Location','EastOutside', 'Fontsize', 14);
hold off;

% Nanoporosity=f(time) for all scaffolds
figure01=figure
axes01 = axes('Parent',figure01,'FontWeight','bold','FontSize',14);
hold(axes01,'all');
grid (axes01,'on');
plot(xaxis2(1),uniquePoint(1,2),'k','Marker','square', 'Markersize', 10,'Linestyle', 'none');
plot(xaxis2(2),uniquePoint(2,2),'k','Marker','x', 'Markersize', 10,'Linestyle', 'none');
plot(xaxis2(3),uniquePoint(3,2),'k','Marker','diamond', 'Markersize', 10,'Linestyle', 'none');
plot(xaxis2(4),uniquePoint(4,2),'k','Marker','pentagram', 'Markersize', 10,'Linestyle', 'none');
plot(xaxis2(5),uniquePoint(5,2),'k','Marker','o', 'Markersize', 10,'Linestyle', 'none');
plot(xaxis2(6),uniquePoint(6,2),'k','Marker','o', 'MarkerFaceColor',[0 0 0], 'Markersize', 10,'Linestyle', 'none'
plot(xaxis2(7),uniquePoint(7,2),'k','Marker','square', 'Markersize', 10,'Linestyle', 'none');
plot(xaxis2(8),uniquePoint(8,2),'k','Marker','x', 'Markersize', 10,'Linestyle', 'none');
plot(xaxis2(9),uniquePoint(9,2),'k','Marker','diamond', 'Markersize', 10,'Linestyle', 'none');
plot(xaxis2(10),uniquePoint(10,2),'k','Marker','pentagram', 'Markersize', 10,'Linestyle', 'none');
plot(xaxis2(11),uniquePoint(11,2),'k','Marker','o', 'Markersize', 10,'Linestyle', 'none');
```

```
plot(xaxis2(12),uniquePoint(12,2),'k','Marker','o','MarkerFaceColor',[0 0 0], 'Markersize', 10,'Linestyle', 'none
xlim([-1 10]);
% Create xlabel
xlabel({'Time [Week]'},'FontWeight','bold','FontSize',16,...
    'FontName','Times');
% Create ylabel
ylabel({'Nanoporosity'},'FontWeight','bold','FontSize',16,...
    'FontName','Times');
legend01 = legend({'scaffold I', 'scaffold II', 'scaffold III', 'scaffold IV',...
    'scaffold V', 'scaffold VI'}, 'Fontname', 'Times','Fontsize', 14,...
    'Location','SouthEast');
hold off;

%Attenuation of betaTCP=f(E) for the last scaffold
figure1=figure
hold on;grid on;
plot(xaxis, mu_peak_vec , xaxis, mu_bTCP_vec);
legend('computed \beta-TCP', 'theoretical \beta-TCP');
xlabel('Energy [keV]','FontSize', 12, 'FontName', 'Times','FontWeight', 'bold');
ylabel('attenuation coefficient [cm^{-1}]','FontSize', 13, 'FontName', 'Times','FontWeight', 'bold');
axis([0 80 0 200]);
title([folder,' ',scaffold])
hold off;
%saveas(figure1,['hist_photon_energy/',folder,'_',scaffold,'.fig']);

% Ratio=f(E) for the last scaffold
hist_energy=figure
plot(xaxis,ratio,'.-')
xlabel('Energy [keV]','FontSize', 16, 'FontName', 'Times','FontWeight', 'bold');
ylabel('Ratio of attenuation coefficients','FontSize', 16, 'FontName', 'Times','FontWeight', 'bold');
axis([0.2 100 0 1]);
xlim([0 100])
ylim([0.2 0.9])
grid on;
title([folder,' ',scaffold])
% saveas(hist_energy,['photon_energy/',folder,'_',scaffold,'_zoomed','.eps']);
% saveas(hist_energy,['photon_energy/',folder,'_',scaffold,'_zoomed','.fig']);

% Ratio=f(E) for all scaffolds
figure02=figure
axes02 = axes('Parent',figure02,'FontWeight','bold','FontSize',14);
hold(axes02,'all');
grid (axes02,'on');
plot(xaxis, ratio4plot(1,:),'LineWidth',3,'Color',[0 0 0]);
plot(xaxis, ratio4plot(2,:),'LineWidth',2,'LineStyle','--','Color',[0 0 0]);
plot(xaxis, ratio4plot(3,:), 'Marker','o','LineWidth',1,'LineStyle','none','Color',[0 0 0]);
plot(xaxis, ratio4plot(4,:),'LineWidth',3,'LineStyle',':','Color',[0 0 0]);
plot(xaxis, ratio4plot(5,:),'LineWidth',2,'LineStyle','-.','Color',[0 0 0]);
plot(xaxis, ratio4plot(6,:), 'LineWidth',1,...
    'Color',[0.0392156876623631 0.141176477074623 0.415686279535294]);
plot(xaxis, ratio4plot(7,:),'LineWidth',3,'Color',[1 0.694117665290833 0.39215686917305]);
plot(xaxis, ratio4plot(8,:), 'LineWidth',2,'LineStyle','--',...
    'Color',[1 0.694117665290833 0.39215686917305]);
plot(xaxis, ratio4plot(9,:),'Marker','o','LineWidth',1,'LineStyle','none','Color',[0 0 1]);
plot(xaxis, ratio4plot(10,:),'LineWidth',3,'LineStyle',':','Color',[0 0 1]);
plot(xaxis, ratio4plot(11,:), 'LineWidth',2,'LineStyle','-.',...
    'Color',[0.847058832645416 0.160784319043159 0]);
plot(xaxis, ratio4plot(12,:), 'Color',[0.847058832645416 0.160784319043159 0]);
xlabel('Photon energy [keV]','FontSize', 18, 'FontName', 'Times','FontWeight', 'bold');
ylabel('Ratio of attenuation coefficients','FontSize', 18, 'FontName', 'Times','FontWeight', 'bold');
xlim([0 100]);
ylim([0.4 1.2]);
%set(gca, 'XTick', (0 : 5 : 100) ); %tick on x axis how frequent are the numbers from min to max
legend('Before','3 weeks','6 weeks','8 weeks','Location','SouthEast');
```